1990

Ultrasonic characterization of elastic constants and defects in composite materials

Hyunjo Jeong
Iowa State University

INFORMATION TO USERS

The most advanced technology has been used to photograph and reproduce this manuscript from the microfilm master. UMI films the text directly from the original or copy submitted. Thus, some thesis and dissertation copies are in typewriter face, while others may be from any type of computer printer.

The quality of this reproduction is dependent upon the quality of the copy submitted. Broken or indistinct print, colored or poor quality illustrations and photographs, print bleedthrough, substandard margins, and improper alignment can adversely affect reproduction.

In the unlikely event that the author did not send UMI a complete manuscript and there are missing pages, these will be noted. Also, if unauthorized copyright material had to be removed, a note will indicate the deletion.

Oversize materials (e.g., maps, drawings, charts) are reproduced by sectioning the original, beginning at the upper left-hand corner and continuing from left to right in equal sections with small overlaps. Each original is also photographed in one exposure and is included in reduced form at the back of the book.

Photographs included in the original manuscript have been reproduced xerographically in this copy. Higher quality 6" x 9" black and white photographic prints are available for any photographs or illustrations appearing in this copy for an additional charge. Contact UMI directly to order.

U·M·I

University Microfilms International
A Bell & Howell Information Company
300 North Zeeb Road, Ann Arbor, MI 48106-1346 USA
313/761-4700 800/521-0600

Order Number 9110512

Ultrasonic characterization of elastic constants and defects in composite materials

Jeong, Hyunjo, Ph.D.

Iowa State University, 1990

U·M·I
300 N. Zeeb Rd.
Ann Arbor, MI 48106

Ultrasonic characterization of elastic constants and defects in composite materials

by

Hyunjo Jeong

A Dissertation Submitted to the
Graduate Faculty in Partial Fulfillment of the
Requirements for the Degree of
DOCTOR OF PHILOSOPHY

Department: Aerospace Engineering and Engineering Mechanics
Major: Engineering Mechanics

Approved:

Signature was redacted for privacy.

In Charge of Major Work

Signature was redacted for privacy.

For the Major Department

Signature was redacted for privacy.

For the Graduate College

Iowa State University
Ames, Iowa
1990

TABLE OF CONTENTS

LIST OF TABLES

LIST OF FIGURES

GENERAL INTRODUCTION

A composite material can be defined as a macroscopic combination of two or more chemically distinct phases, having a distinct interface separating them. The phase which is harder and stronger is called the reinforcement, whereas the other is referred to as the matrix. Composite materials were developed because no single, homogeneous structural material could be found that had all of the desired properties for a given application. Fiber reinforced polymer composites were developed in response to demands of the aerospace community for enhanced performance. Metal matrix composites (MMCs) have been developed for more than 20 years. However, the initial emphases were on continuous fiber MMCs such as boron/aluminum composite system. In recent years, discontinuous MMCs have been investigated due to the economic production of silicon carbides [1]. Among the discontinuously reinforced MMCs, silicon carbide whiskers (SiC_w) and particulates (SiC_p) in an aluminum matrix have attracted a good deal of attraction [2,3]. Aluminum matrix composites are of interest because they can be subjected to conventional metal forming processes such as extrusion, rolling, forging and casting. MMCs offer high specific strength and specific modulus plus a service temperature capability much higher than that of polymer matrix composites.

The properties of composites are strongly influenced by the properties of their

constituent materials as well as the shape and orientation of the reinforcement. The composite properties may be the volume fraction sum of properties of the constituent (rule of mixtures) or the constituents may interact in a more complex way so as to provide properties in the composite that are not accounted for by simple rule of mixtures. The geometry of the reinforcement may be described by the shape, size, and size distribution. Since the shape determines the interfacial area, it plays an important role in determining the extent of the interaction between the reinforcement and the matrix. The orientation of the reinforcement affects the isotropy of the composite system. When the reinforcement is in the form of particulate, with all their dimensions approximately equal, the composite behaves essentially as isotropic material. In fiber reinforced composites, such as unidirectional composites, anisotropy may be desirable since the primary advantage of the composites is the ability to control anisotropy by design and fabrication. In other cases, the manufacturing process (e.g., extrusion of short fiber MMCs) may induce orientation of the reinforcement and hence induce some anisotropy. A number of analytical model were developed to predict the elastic behavior of a particular composite system. Analytical models range from simple (rule of mixtures) to rigorous. When a composite design engineer wants to develop a new composite system, modelling is important to tailor the unique properties from the properties of constituent phases and other microstructural variables.

Many of the composites—in particular, the fiber reinforced polymer and metal matrix composites—are inherently imperfect by virtue of the processing and manufacturing techniques with which they are fabricated. A cured polymer composite part may contain a multitude of internal defects, such as voids, delaminations, fiber

misorientations and nonuniform fiber distributions. Discontinuous MMCs can also contain defects such as voids and intermetallic compounds. Some of these internal defects may become critical flaws during the service life of a part and cause catastrophic failure. Even when the defects are individually less than critical, they may collectively have a large effect on the material property and hence the performance of a component. Consequently, composite materials introduce more requirement for inspection and quality assurance. Different nondestructive inspection (NDI) or nondestructive evaluation (NDE) techniques have been employed for fiber reinforced polymer composites [4-13] as well as metal matrix composites [14-18].

Ultrasonic techniques are most frequently used for NDE of composites. Recent review of their concepts and principles are given in [19,20]. Various material properties, including the stiffness, the volume fraction of voids, and the attenuation are monitored by different ultrasonic methods. Velocity measurement, attenuation measurement, C-scan and acousto-ultrasonics are examples of ultrasonic NDE techniques. Velocity measurement provides a better absolute value and has proved to be a viable method of directly determining dynamic elastic constants. If the material density is known, elastic moduli can be immediately calculated from relationships giving the wave speed in terms of the moduli and density. As a material parameter, stiffness can be affected by many variables. For a polymeric composite laminate of a given fiber orientation and resin type, a number of variables can affect the elastic constants. These include the fiber and resin volume fraction, the state of cure, the fiber to matrix bond strength, and the void content. For particulate reinforced MMCs, the volume fraction of reinforcement, the particle shape and orientation, and the content of voids and intermetallics can all affect the elastic stiffness. Thus, a knowledge of the

elastic stiffness of composite materials is necessary for design verification and quality control.

Review of Previous Work

The topic of this thesis covers a rather extensive area so that the review of literature is not intended to be exhaustive. Here, some relevant works are reviewed in the following areas: dynamic elastic constant measurements, composite models, NDE of voids, ultrasonic spectroscopy, and Kramers-Kronig relations.

Dynamic elastic constant measurement. Recently a number of techniques were used to measure the dynamic Young's modulus of isotropic materials [21]. Since ultrasonic velocities of longitudinal and shear waves are given respectively by $V_L = \sqrt{(\lambda + 2\mu)/\rho}$ and $V_S = \sqrt{\mu/\rho}$ (λ and μ are Lame's constants and ρ is density of the material), measurement of these velocities will produce a complete description of the isotropic properties. Ultrasonic velocities can be measured using the time-of-flight of a pulse or using the phase spectroscopy. For anisotropic materials, it can be shown that, if the density of the material is known, the dynamic elastic moduli can be deduced from velocity measurements of longitudinal and shear waves propagating in various directions of the specimen [22]. Several methods have been used to measure the velocity of sound in composites, including the contact through transmission [23-28], the immersion through transmission [29-33] and the critical angle method [34]. Of these, immersion technique has been proved to be most viable for quality control. In some studies, velocity was measured using multiple angles of incidence and a numerical procedure was used to determine the elastic constants [34-36]. For composite materials in the form of thin, laminated plates, ultrasonic

wave speeds were usually measured through the thickness. Recently, Stiffler [37] has suggested using in-plane Lamb waves to determine the in-plane laminate stiffnesses.

Composite models. A number of composite models have been developed to predict the effective elastic constants of composites based on the elastic properties of constituent phases. These composite models include the shear lag model, the laminated plate model, the variational principle model, and the Eshelby and Mori-Tanaka's model. The mathematical treatment of these models has been given by Mura [38] and Christensen [39].

The shear lag model is best suited for an aligned short fiber composite where short fibers of constant aspect ratio are all aligned in the loading direction [40,41]. The shear lag model can also be applied to prediction of the flow stress during plastic deformation of MMCs [42]. It is known that the shear lag model tends to give a poor approximation than the other rigorous models such as Eshelby's model [43].

The laminated plate model [44] provides an analytical tool to predict overall properties of the laminate which usually consists of laminae with different fiber orientations.

The composite model based on variational principles is aimed at providing the upper and lower bounds on the elastic properties. Hashin and Shtrikman considered new composite model based on the variational principle which is valid for anisotropic phases [45,46].

Eshelby's model [47] is suited for a short fiber composite system because it takes into account the shape effect of an ellipsoidal fiber. Eshelby's model is also applicable to particulate and continuous fiber composites as special cases of short fiber. Application of Eshelby's model to determination of elastic constants are given in

[39]. Eshelby's model is limited to dilute concentration of the reinforcement. In actual composites, however, the volume fraction of fibers are finite so that the interaction between fibers becomes important. In this case, Eshelby's model can still be used to provide an approximate solution of the stress field if a term accounting for such interaction is included. For this purpose, the concept of the average perturbed stress in the matrix of a composite is introduced by Mori and Tanaka [48]. Combination of Eshelby's model and Mori-Tanaka's theory solved important elasticity problems including the effective elastic constants [49-56]. Within the framework of this model, three-phase composite models were also considered [52,57,58]. More recently, Benveniste [59,60] reformulated the Eshelby and Mori-Tanaka's problem to obtain a direct tensor expression for effective stiffness. Using Benveniste's approach, Norris [61] examined the validity of Mori-Tanaka's approximation for multi-phase composites.

NDE of voids. Voids are one of the most common flaws encountered during the fabrication of fiber reinforced polymer composites. Voids arise from two main causes [62]: entrapment of air due to incomplete wetting of the fibers by the resin, and the release of volatile gas during the curing cycle in thermosetting resins and during the melt processing operations in thermoplastic polymers. The void content and distribution depends on the fiber volume fraction and the processing parameters such as temperature, pressure and time. Voids occurring at the interface between the unidirectional laminae are usually elongated into ellipsoidal cavities along the adjacent fiber directions [63]. On the other hand, voids in woven laminates tend to be more spherical [64]. The presence of voids in a composite laminate may affect some of its matrix dominated mechanical properties [65]. Large reductions in interlaminar

shear strengths were observed even when the void content was only a few percent by volume [66,67]. The presence of voids generally decreases the fatigue resistance and increases the rate and amount of water absorption [68]. Thus, a knowledge of the void content is important for estimating the quality of the composite.

Since voids are strong scatterers for elastic waves, the presence of voids in composite laminates has noticeable effects on ultrasonic attenuation. The correlation between attenuation and void content in carbon fiber reinforced composites are well known: greater void content causes increased attenuation and the increase is greater at higher frequencies [8,69]. By manufacturing standards with known void content, the void content of a particular system of composite can be quantitatively evaluated. Martin [70] and Hale and Ashton [71] developed a model for calculating the attenuation of ultrasonic waves propagating through a fiber reinforced composite containing voids. Recently, measurement procedures were developed to obtain the ultrasonic attenuation as a function of frequency using broadband pulses, and a correlation between the attenuation slope, or $d\alpha/df$, and the volume fraction of porosity has been established [64,72]. Interlaminar shear strength was found to correlate with the void content and hence the attenuation coefficient [8,65,69]. The effects of porosity on other ultrasonic quantities such as the backscatter have also been of interest [73-76]. Changes in ultrasonic longitudinal and shear velocities with porosity have also been studied [77-79].

Ultrasonic spectroscopy. Ultrasonic spectroscopy is the frequency domain study of ultrasonic wave interactions with a material. Ultrasonic spectroscopy technique proves valuable because many material properties are manifested as amplitude or phase changes in the ultrasonic waves interrogating the specimen. The technique

is based on the Fourier analysis of digitized ultrasonic signals. Phase velocity, group velocity and attenuation can be obtained as a function of frequency [80-84]. Phase slope method was also used for accurate measurement of phase delay in nondispersive media [85,86]. More recently, amplitude spectrum technique was used to measure the phase velocity of thin samples, where different reflected or transmitted waveforms from the sample boundary can not be separated in the time domain [87,88].

Kramers-Kronig relations. The Kramers-Kronig relations relate the real and imaginary parts of the frequency response function for any linear, causal, passive system. For acoustical systems, these relations lead to a pair of integral relations between the attenuation and the phase velocity. The exact relations require the evaluation of the integrals over all frequencies. O'Donnel et al. [89] proposed a local approximation to the exact Kramers-Kronig relations which allowed the change in phase velocity to be estimated from the attenuation coefficient measured over a finite frequency range. Rose et al. [90] and Rose [91] have applied the exact Kramers-Kronig relations to the calculation of porosity. Hughes et al. [84] tested the local approximation in porous epoxy. Beltzer and Brauner [92,93] used the Kramers-Kronig relations to obtain the dynamic response of fibrous composites for the full frequency range.

Objectives, Approaches and Findings

In this thesis, ultrasonic velocities were used to characterize the elastic constants of particulate reinforced MMCs and the void (porosity) content of fiber reinforced polymer composites. The contents of the thesis are divided into two parts. The first part deals with the determination of anisotropic elastic constants of SiC_p reinforced

Al/SiC$_p$ MMCs were predicted using the properties of the constituent phases and some of microstructural data. The transversely isotropic properties predicted by the model were compared with the ultrasonically measured results.

The second part of the thesis is concerned with the theoretical and experimental studies of ultrasonic velocity for the NDE of porosity in carbon fiber reinforced plastics (CFRP). A fiber reinforced composite containing voids in the matrix phase was considered in the study of the effect of void characteristics and fiber properties on the ultrasonic velocity. The model was composed of isotropic matrix, unidirectional fibers and ellipsoidal voids. In the model, the matrix and voids were assumed to form an "effective matrix". The characteristics of this effective matrix was calculated using Mori-Tanaka's theory and the composite cylinders assemblage model by Hashin was employed to obtain the overall transversely isotropic properties. Special attention was given to the effect of microstructure features—void and fiber contents, fiber anisotropy and void shape—on the velocity of longitudinal waves propagating normal to the fibers. The analysis results indicated that ultrasonic velocity could be used as a tool for the NDE of porosity in CFRP. Following the model analysis, phase velocity and attenuation were measured using ultrasonic spectroscopy in the through transmission, immersion testing mode. Broadband ultrasonic pulses were used and frequency dependent phase velocity was obtained for a series of carbon (graphite) fiber reinforced epoxy and polyimide laminate specimens containing different level of porosity. The measured phase velocity was found to correlate with the void content. A quantitative correlation between velocity change and void content was sought by calculating the fractional velocity decrease (expressed in percent) at a given frequency. Finally, the relationship between attenuation and velocity change

was tested using the local approximation of the Kramers-Kronig relations.

In summary, there are three major accomplishments of this thesis: (1) The determination of the complete orthotropic elastic constants of Al/SiC$_p$ MMC's by ultrasonic velocity measurements. MMCs are of growing importance for structural applications and the elastic constant data for the Al/SiC$_p$ system should prove useful for design purposes. (2) Development of a matrix formulation for predicting the effective stiffness of two-phase composites containing arbitrarily oriented ellipsoidal fibers. When a new composite system is needed in an application, the ability to model allows one to tailor its unique properties from the constituent properties and microstructural characteristics. (3) Application of the ultrasonic phase velocity to the NDE of porosity in CFRP. Although further research is needed in this area, analytical and experimental studies of ultrasonic velocity as a tool for void content evaluation have been made.

PART I. CHARACTERIZATION OF ELASTIC CONSTANTS

1. INTRODUCTION

Metal matrix composites are promising new materials for structural applications because of their high specific stiffness and strength, and high temperature stability. Of particular interest are the SiC whisker (SiC_w) and particulate (SiC_p) reinforced aluminum matrix composites. The improved mechanical properties, such as the elastic moduli and strength, are governed by the properties of constituent phases, the interface between the matrix and reinforcing particles, as well as the shape, orientation and volume fraction of the reinforcing phase. The shape and orientation of SiC particles have a major effect on the anisotropic properties of Al/SiC composites. The overall properties also depend on the manufacturing process of these composites since it determines the orientation of the particles and may produce internal defects such as porosity or intermetallic compounds [14]. Thus it is important to experimentally characterize the effective elastic properties of these composites and to theoretically predict them from the knowledge of the constituents properties and the microstructures.

Recently ultrasonic methods have been widely used as a nondestructive evaluation tool for detecting inhomogeneous distribution of SiC particles [16], for quality control of Al/SiC composites during manufacturing processes [15,18], and for measuring anisotropic elastic properties [26,28] of these composites. The elastic stiffnesses

may be determined by a series of mechanical tests or by ultrasonic wave propagation techniques. Ultrasonic techniques offer some advantage because they can be used nondestructively with small samples. The magnitude of the velocity of an ultrasonic wave propagating in a material is related to the density and one or more stiffness components C_{ij} of the material. Measurements of wave velocity along a sufficient number of directions will enable all the stiffness components to be determined. The elastic constants determined ultrasonically can be compared to those determined by mechanical tests, provided the ultrasonic wavelengths used are much larger than the dimensions of constituent material phases.

In this thesis, both experimental and theoretical results on the effective elastic moduli of α-SiC_p reinforced aluminum metal matrix composites fabricated by powder metallurgy and extrusion process are reported. We utilized ultrasonic wave propagation to measure elastic stiffnesses in the long wavelength limit in these materials. Assuming the composites to be orthotropic, all nine stiffness components were measured using an water immersion, oblique incidence technique [29-33,35]. Other engineering constants including Young's moduli, shear moduli and Poisson's ratios were also reported. Young's moduli deduced from the ultrasonic results were compared with the tensile test data. Microstructures of these composites were also examined using scanning electron microscopy [14] and digital image analysis. Special attention was given to the SiC particle characteristics such as the shape, aspect ratio and orientation distribution.

Prediction of elastic constants were made by a two-phase composite model based on the Eshelby's equivalent inclusion principle [47] and the Mori-Tanaka's theory [48]. This model is known to be valid for finite concentration of fibers. A simple

matrix form of effective stiffness expression was developed and application of this model system to prediction of Al/SiC$_p$ MMCs were discussed. The elastic constants predicted by the model were compared with the ultrasonically measured data.

2. MATERIALS

Three aluminum base alloys of 2124, 6061 and 7091 were employed. Each of these alloys were reinforced by 10-30% volume fraction of SiC_p. The SiC_p free Al alloys of each system were also fabricated at the same time, and a total of fourteen samples were studied. These metal matrix composites were fabricated by DWA Composites Specialties, Inc. using a powder metallurgy technique. The SiC particulates were obtained from a α-SiC of abrasive grade that have been crushed into fine powders and separated by the desired particle size. The composite materials were received in an extruded-plate form with final extrusion ratios ranging from 11:1 to 39:1. Following extrusion, the 2124 Al/SiC_p were T4 heat treated, while the 6061 Al/SiC_p and the 7091 Al/SiC_p were T6 heat treated. The plates were surface ground and prepared into laboratory specimens of dimensions 1.2 cm in thickness, 6 cm in width, and 10 cm in length.

Detailed information of these composites is summarized in Table 2.1, including base alloy, billet number, SiC_p loading, extrusion ratio and density. Mass density was determined by the displacement method using distilled water.

Table 2.1: SiC_p reinforced metal matrix composites

Base alloy	Billet number	SiC_p loading(%)	Extrusion ratio	Density (g/cm^3)
2124 Al	PE-2600	0	20:1	2.77
2124 Al	PE-3025-1	20	NA	2.85
2124 Al	PE-2404	25	11:1	2.89
2124 Al	PE-2229	25	11:1	2.88
2124 Al	PE-2488	30	20:1	2.90
6061 Al	PE-2045	0	11:1	2.71
6061 Al	PE-2047	20	10:1	2.90
6061 Al	PE-2099	25	39:1	2.84
6061 Al	PE-2731	30	20:1	2.84
7091 Al	PE-2730	0	20:1	2.84
7091 Al	PE-2711	10	25:1	2.88
7091 Al	PE-2712	20	25:1	2.91
7091 Al	PE-2713	30	20:1	2.92
7091 Al	PE-2665	30	11:1	2.94

3. ULTRASONIC MEASUREMENTS

3.1 Wave Propagation in Anisotropic Solids

Consider a plane displacement wave propagating with phase velocity V in a direction defined by the unit propagation vector $\boldsymbol{n}$

$$u_i = Ad_i exp[ik(\boldsymbol{x} \cdot \boldsymbol{n} - Vt)] \tag{3.1}$$

where A is the amplitude, d_i are the components of a unit vector defining the direction of the particle displacements, $\boldsymbol{k} = k\boldsymbol{n} = \frac{\omega}{V}\boldsymbol{n}$ is the wave number, $\boldsymbol{x}$ is the position vector, ω is the circular frequency, and t is time.

On substitution of Equation (3.1) into the equation of motion

$$\rho \ddot{u}_i = C_{ijkl} u_{l,jk} \tag{3.2}$$

we obtain

$$(C_{ijkl} n_j n_l - \rho V^2 \delta_{ik}) u_k = 0 \tag{3.3}$$

Here C_{ijkl} are the elastic constants, ρ is the density, and δ_{ik} is the Kronecker delta. Equation (3.3), known as Christoffel's equation, represents a set of homogeneous equations for three unknown displacements u_1, u_2 and u_3. For a nontrivial solution the determinant of the coefficients must vanish, that is

$$\left| \Gamma_{ik} - \rho V^2 \delta_{ik} \right| = 0 \tag{3.4}$$

where

$$\Gamma_{ik} = C_{ijkl} n_j n_l. \tag{3.5}$$

The three roots of Equation (3.4) are in general different, giving rise to three different velocities of propagation. Therefore, for a given direction of propagation, defined by n_j, there will be three waves with mutually perpendicular displacement vectors propagating with different phase velocities. In general these waves will not be pure longitudinal or pure transverse, but one will be quasilongitudinal (QL) and the other two will be quasitransverse (QT). However, for certain special directions of propagation (usually directions of symmetry) one wave is pure longitudinal (L) and the other two are pure transverse (T).

Another aspect of wave propagation which is of great importance in anisotropic materials is the propagation of energy. Because the energy flux vector usually does not coincide with the wave normal $\boldsymbol{n}$, the values and directions of the phase velocity and energy (or group) velocity are in general different. The energy velocity (V_g) is greater than or equal to the phase velocity (V) and they are related by the following simple equation

$$V_g \cos\psi = V \tag{3.6}$$

where ψ is the angle between the energy velocity and the wave vector $\boldsymbol{k}$ [94].

This phenomenon of the deviation of energy from the direction of wave propagation in anisotropic solids has many important consequences that must be taken into consideration in experimental studies of ultrasonic wave speed for material characterization purposes. As a simple example, the predicted refracted direction of an obliquely incident beam using Snell's law (based on phase velocity) is not the actual path traversed by the ultrasonic energy.

3.2 Elastic Constants for Orthotropic Symmetry

The elastic stiffness of a material with orthotropic symmetry are characterized by nine independent constants. These are conveniently shown as the stiffness matrix using contracted notation:

$$[C] = \begin{bmatrix} C_{11} & C_{12} & C_{13} & 0 & 0 & 0 \\ C_{12} & C_{22} & C_{23} & 0 & 0 & 0 \\ C_{13} & C_{23} & C_{33} & 0 & 0 & 0 \\ 0 & 0 & 0 & C_{44} & 0 & 0 \\ 0 & 0 & 0 & 0 & C_{55} & 0 \\ 0 & 0 & 0 & 0 & 0 & C_{66} \end{bmatrix} \tag{3.7}$$

Orthotropic materials have three mutually perpendicular symmetry directions. The three symmetry axes are chosen as follows: x_1 is the extrusion direction, x_2 is the in-plane transverse direction, and x_3 is the out-of-plane direction as shown in Figure 3.1.

In order to determine the effective elastic stiffnesses of an orthotropic material from the ultrasonic velocities, we need at least nine independent velocity (especially phase velocity) measurements. Consider, for example, a plane wave travelling in the x_1 direction (n_1=1, $n_2 = n_3$=0). From Equation (3.4), the characteristic equation reduces to

$$(C_{11} - \rho V^2)(C_{66} - \rho V^2)(C_{55} - \rho V^2) = 0. \tag{3.8}$$

Hence there exists the possibility of three different waves having velocities $\sqrt{C_{11}/\rho}$, $\sqrt{C_{66}/\rho}$, and $\sqrt{C_{55}/\rho}$. By substituting each of these velocities into Christoffel's

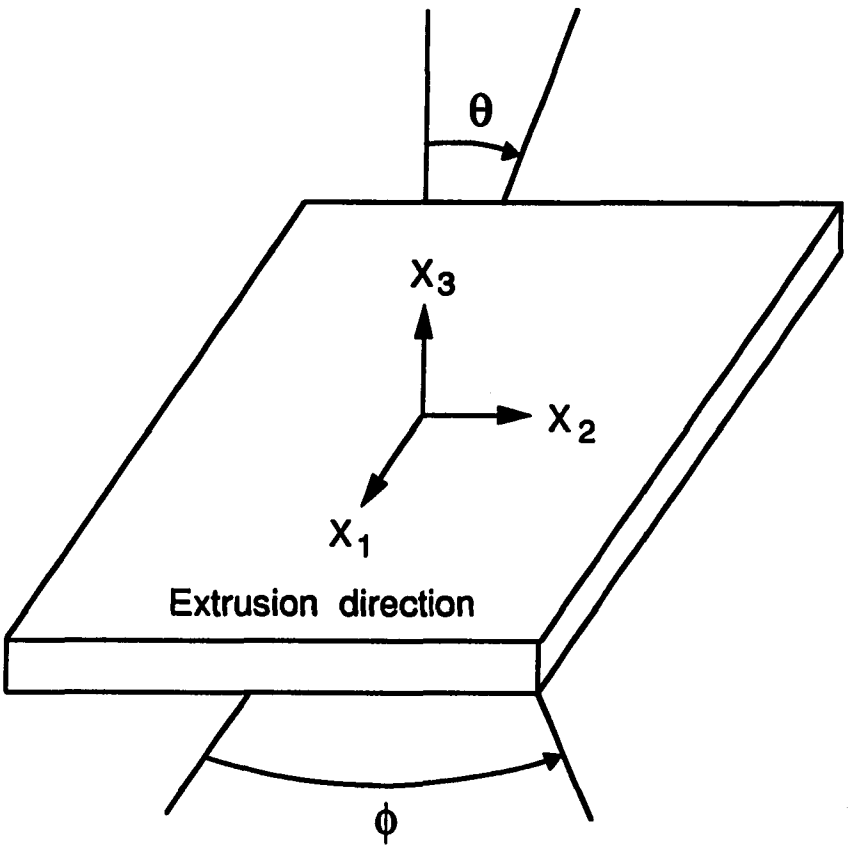

Figure 3.1: Material symmetry axes for orthotropic plate

equation, Equation (3.3), it is found that the first wave is purely longitudinal, while the other two are purely transverse, with displacement vectors in the x_2 and x_3 directions, respectively. Similar results are obtained for waves propagating in the directions of the other symmetry axes. Thus it is clear that all the diagonal stiffness components can be determined by measuring the velocities of appropriate waves propagating along symmetry directions.

Consider, now, a wave propagating along a direction at an angle θ_r from the x_2 axis in the x_1-x_2 plane ($n_1=\sin\theta_r$, $n_2=\cos\theta_r$, $n_3=0$). In this case, one solution to Equation (3.4) represents a purely transverse wave having a displacement vector in the x_3 direction and a phase velocity given by

$$V = \sqrt{(n_1^2 C_{55} + n_2^2 C_{44})/\rho} \tag{3.9}$$

The other two solutions to Equation (3.4) with displacement vectors in the x_1-x_2 plane are neither purely longitudinal nor purely transverse; they propagate with velocities given by the roots of the equation

$$(n_1^2 C_{66} + n_2^2 C_{22} - \rho V_{QT}^2)(n_1^2 C_{11} + n_2^2 C_{66} - \rho V_{QT}^2) - n_1^2 n_2^2 (C_{12} + C_{66})^2 = 0. \tag{3.10}$$

The faster wave is QL and the slower one is QT. Similar equations are obtained when one considers propagation along nonsymmetry directions on the other two symmetry planes. For the determination of C_{12}, a set of velocity measurements are made at different angles of propagation in an oblique incidence, immersion experiment, and a best solution is obtained for C_{12} using a nonlinear least squares method [34,35,95]. C_{12} can be also obtained by cutting a specimen with faces at intermediate angle to the symmetry directions, usually 45 degrees [23-27]. In this work, we have used the oblique incidence, through transmission testing mode to determine all off-diagonal

stiffness components together with the shear components C_{44}, C_{55} and C_{66}. The shear stiffness components were also determined using direct contact mode.

3.3 Experimental

Anticipating angle of refraction and energy beam deviation from the phase front normal for oblique incidence, we cut two parallelopipeds of about $4.0 \times 1.5 \times 1.2$ *cm* from each sample with their faces parallel to the symmetry planes. Surfaces were prepared by grinding so that opposite faces are flat and parallel to within 5 μm. The sample was mounted on a turntable, with an accuracy of 0.1°, in a water tank; the transmitting and receiving transducers were located on opposite sides of the sample for through transmission ultrasonic velocity measurement. The angle of incidence was varied by rotating the turntable. Throughout the experiment, two 5 MHz broadband transducers of 0.635 *cm* (0.25 *in*) diameter were used. The transmitting transducer was driven by a spike voltage pulse. Since measurement of phase velocities over the frequency range from 0.5 MHz to 30 MHz resulted in less than 0.5% difference between the measured velocities, dispersion was neglected and velocity was measured using the time of flight of transmitted pulses. The time of flight was measured with a 1 ns relative accuracy on a LeCroy 9400 digital oscilloscope.

3.3.1 Measurements of diagonal stiffness components

In order to measure C_{11}, a pulse of L wave is propagated along the x_1 axis in an immersion setup. By measuring the time delay difference, Δt, of the L wave pulse with and without the sample in the ultrasonic path, the L wave velocity V_L of sample is calculated from $V_L = (1/V_W - \Delta t/d)^{-1}$, where d is the sample thickness and V_W

is the sound velocity in water. The temperature of the water bath was measured with 0.1°C accuracy and the temperature dependent sound velocity in water was computed using the equation given in [96]. C_{11} is then calculated from $C_{11} = \rho V_L^2$, where ρ is the density of the material. C_{22} and C_{33} can be measured in a similar manner.

Shear stiffness components were first measured by direct contact method. In order to obtain C_{44}, for example, T wave is propagated in the x_2 direction with polarization in x_3 direction or propagated in the x_3 direction with polarization in the x_2 direction. By measuring the time of flight, Δt, from two consecutive pulses, the T wave velocity is calculated by $V_T = 2d/\Delta t$. Then the shear stiffness components is obtained by $C_{44} = \rho V_T^2$. The shear stiffness components were also measured using the oblique incidence, immersion method together with the off-diagonal stiffness components.

3.3.2 Measurements at oblique incidence

When a L wave launched from an immersed transducer impinges on the surface of an anisotropic solid inclined at an angle to the ultrasonic path, mode conversion will occur at the liquid-solid interface. In general, two QT modes and one QL mode will be produced; however, if the propagation is constrained to a symmetry plane of an orthotropic medium and along a nonsymmetry direction, then only one QT wave and one QL wave will be generated, as shown in Figure 3.2.

In an oblique incidence, through-transmission immersion test, the difference in delay time for the L-QT-L wave with and without the sample in place at an incident

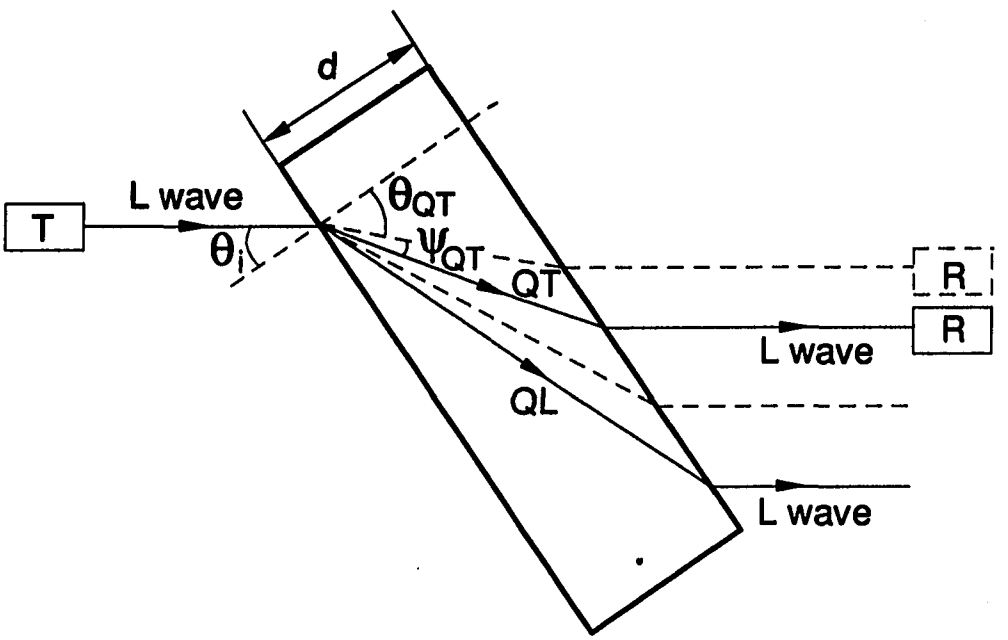

Figure 3.2: Oblique incidence of sound wave in an orthotropic plate submerged in water

angle θ_i is given by

$$\Delta t = \frac{d}{\cos\theta_{QT}}\left(\frac{\cos(\theta_{QT} - \theta_i)}{V_W} - \frac{1}{V_{QT}}\right) \tag{3.11}$$

in which the refraction angle θ_{QT} is given by

$$\theta_{QT} = \tan^{-1}\left(\frac{\sin\theta_i}{\cos\theta_i - \Delta t V_W/d}\right). \tag{3.12}$$

The phase velocity for QT wave in the direction of θ_{QT} is then calculated from Snell's law by

$$V_{QT} = \left(\frac{1}{V_W^2} - \frac{2\Delta t\cos\theta_i}{dV_W} + \frac{\Delta t^2}{d^2}\right)^{-1/2}. \tag{3.13}$$

Similar expressions can be written down for the L-QL-L wave in which V_{QT} and θ_{QT} are replaced by V_{QL} and θ_{QL}. Hence, by measuring θ_i and Δt for the QT and QL waves, one can calculate θ_{QT} and θ_{QL} and then V_{QT} and V_{QL}.

Since the refracted QT and QL waves will travel in nonsymmetry directions when the incident beam is oblique, the acoustic wave energy propagates at a deviation angle, ψ, with respect to the phase front normal as shown in Figure 3.2. Depending on the degree of anisotropy, the emergent beam can be displaced significantly from its refraction angle calculated from Snell's law. It is therefore important to shift the receiving transducer to the position where the energy emerges from the sample (Figure 3.2). This seems to create the dilemma that the measured delay time is that of the group velocity while the Christoffel equation for calculating the stiffnesses uses the phase velocity. However, combining Snell's law and Equation (3.6) that relates the phase velocity to the group velocity, it can be shown that the time delay experienced by the group velocity (Δt_g) is equal to the time delay experienced by the phase velocity (Δt_p). Mignogna [97] proved that Δt_g is equivalent to Δt_p for

waves propagating in arbitrary symmetry class of materials. Thus the phase velocity can be correctly calculated from Equation (3.13) using the time delay measured for the group velocity.

Measurements of C_{66}, C_{12}. In order to measure C_{66} and C_{12} using oblique incidence technique the sample is oriented with the x_3-axis vertical and the pulse is then propagated in the x_1-x_2 plane. Two refracted waves (QT and QL) will be generated as θ_i is increased from zero. Δt for QT and QL waves, and hence θ_{QT}, V_{QT} and θ_{QL}, V_{QL}, respectively can be obtained for different incident angles.

With the sample mounted as shown in Figure 3.3, the refracted QT waves will propagate along the phase normal vector $(n_1, n_2, 0)$, where $n_1 = \sin\theta_{QT}$, $n_2 = \cos\theta_{QT}$, and satisfy the characteristic equation (3.10). Similar expressions can be written for QL waves.

Introducing two unknowns, $X = C_{12}$ and $Y = C_{66}$, Equation (3.10) can be written as

$$AX^2 + 2AXY + BY + D = 0 \tag{3.14}$$

where

$$A = n_1^2 n_2^2 \tag{3.15}$$

$$B = -n_1^4 C_{11} - n_2^4 C_{22} + \rho V_{QT}^2 \tag{3.16}$$

$$D = -n_1^2 n_2^2 C_{11} C_{22} + (n_1^2 C_{11} + n_2^2 C_{22})\rho V_{QT}^2 - (\rho V_{QT}^2)^2 \tag{3.17}$$

Equation (3.14) then becomes a coupled quadratic Equation, so that if two different sets of (θ_{QT}, V_{QT}) are known, it can be simply solved for C_{12} and C_{66}; however, because of experimental errors and material variability, this does not lead to reliable

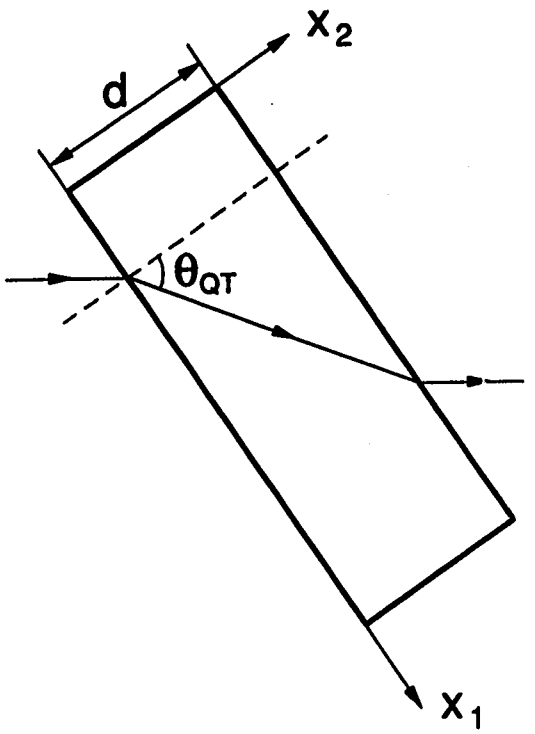

Figure 3.3: Sample orientation for measuring C_{66} and C_{12}

values of C_{12} and C_{66}. Instead a set of measurements exceeding the number of unknown elastic constants are made at different incidence angles, and from this set of data a best solution is obtained to the Equation (3.14) with minimum least squares error. Furthermore, measurements were made on the QT waves only since a huge amount of numerical error was found to be involved in the computation of these elastic constants when QL waves were used.

We first measured three sets of Δt for QT waves at $\theta_i = \pm 6^\circ, \pm 8^\circ$ and $\pm 10^\circ$ and found the mean Δt for each angle in order to calculate refraction angles and velocities from Equations (3.12) and (3.13), respectively. C_{12} and C_{66} were then determined from Equation (3.14) using a nonlinear least squares method.

An equivalent set of measurements could be made by propagating the pulse along an angle θ_{QT} from the x_1 axis with $n_1 = \cos\theta_{QT}$, $n_2 = \sin\theta_{QT}$, $n_3 = 0$.

Measurements of C_{55}, C_{13}. To measure C_{55} and C_{13} the sample is oriented with the x_2-axis vertical (Figure 3.4). A pulse is then propagated in the x_1-x_3 plane. Refracted QT waves will propagate along the vector (n_1,0, n_3), where $n_1 = \sin\theta_{QT}$, $n_3 = \cos\theta_{QT}$. An equation analogous to Equation (3.10) is satisfied for propagation in the x_1-x_3 plane. This equation can be easily written down by changing the subscripts for the stiffness components and the direction cosines in Equation (3.10) so that 2→3 and 6→5.

An equivalent set of measurements could be made by propagating the pulse along an angle θ_{QT} from the x_1 axis with $n_1 = \cos\theta_{QT}$, n_2=0, $n_3 = \sin\theta_{QT}$.

Measurements of C_{44}, C_{23}. To measure C_{44} and C_{23} the sample is oriented with the x_1-axis vertical (Figure 3.5). The pulse is then propagated in the x_2-x_3 plane. Refracted waves will propagate along the vector (0, n_2, n_3), where

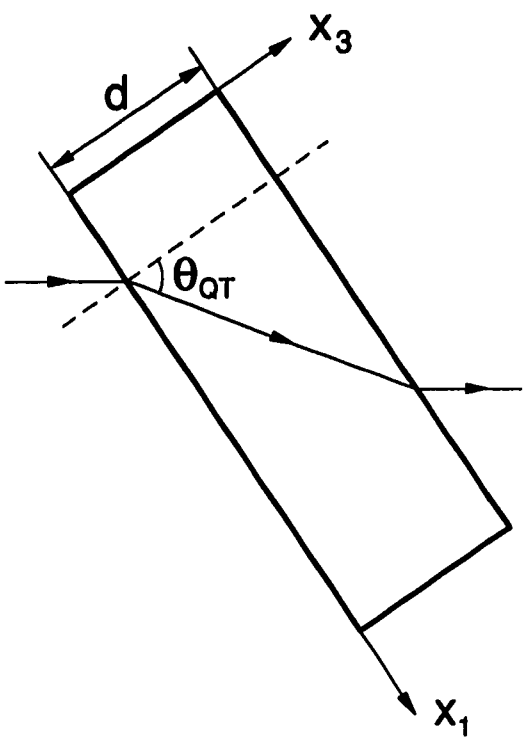

Figure 3.4: Sample orientation for measuring C_{55} and C_{13}

$n_2 = \sin\theta_{QT}$, $n_3 = \cos\theta_{QT}$. Velocities of QL and QT waves will satisfy similar relationship to Equation (3.10) if the subscripts are changed so that 1—2, 2—3 and 6—4.

An equivalent set of measurements could be made by propagating the pulse along an angle θ_{QT} from the x_2 axis with n_1=0, $n_2 = \cos\theta_{QT}$, $n_3 = \sin\theta_{QT}$.

3.4 Results and Discussion

The experimental results for the three different Al/SiC$_p$ composite systems are listed in Tables 3.1-3.3. The nine stiffness components and other engineering constants such as the Young's modulus and Poisson's ratio are listed. Young's moduli in x_1, x_2 and x_3 directions were computed from the relations: $E_{11} = 1/S_{11}$, $E_{22} = 1/S_{22}$, $E_{33} = 1/S_{33}$, where S_{ij} denote components of the elastic compliance which are related to the elastic stiffness according to $[S_{ij}] = [C_{ij}]^{-1}$. Shear moduli in the 2-3, 1-3 and 1-2 planes were obtained from the relations: $G_{23} = C_{44}$, $G_{13} = C_{55}$, $G_{12} = C_{66}$. Poisson's ratios were obtained from $\nu_{12} = -S_{12}/S_{11}$, $\nu_{21} = -S_{12}/S_{22}$, $\nu_{13} = -S_{13}/S_{11}$, $\nu_{31} = -S_{13}/S_{33}$, $\nu_{23} = -S_{23}/S_{22}$, $\nu_{32} = -S_{23}/S_{33}$.

The experimental results for 25% 6061 Al/SiC$_p$ (PE-2099) and 30% 7091 Al/SiC$_p$ (PE-2713) were not included because the sample dimension of the former was not thick enough for ultrasonic measurements due to its high extrusion ratio and the latter sample contained larger amount of porosity compared to other samples (see Tables 2.1 and 5.1).

The accuracy of the stiffness measurement is determined by the accuracy of the velocity values. Since C_{11}, C_{22} and C_{33} are determined by the measurement of pure longitudinal modes along the symmetry axes, the accuracy is very high. Considering

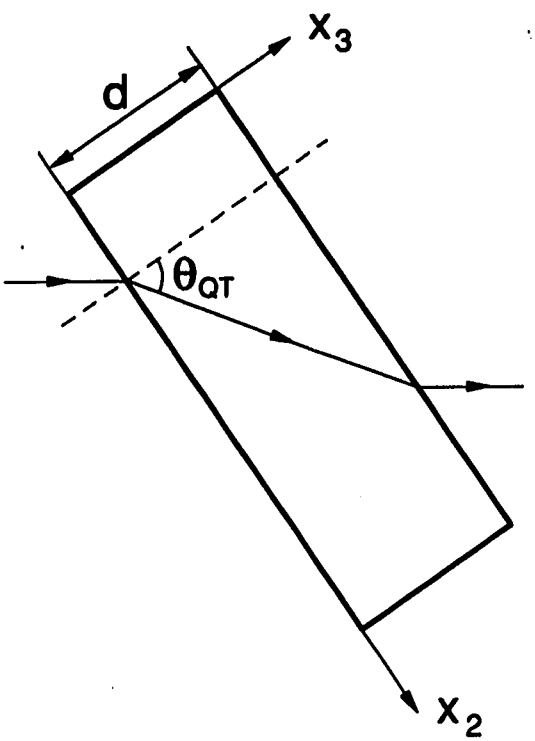

Figure 3.5: Sample orientation for measuring C_{44} and C_{23}

Table 3.1: Ultrasonic measurement results for the 2124 Al/SiC$_p$ composites (unit=GPa except ν_{ij})

	PE-2600 0 %	PE-3025-1 20 %	PE-2404 25 %	PE-2229 25 %	PE-2488 30 %
C_{11}	113.5	150.2	162.7	161.2	169.4
C_{22}	113.8	145.9	159.7	157.4	166.6
C_{33}	113.2	139.6	147.8	147.2	156.0
C_{12}	57.6	64.4	66.9	66.0	68.6
C_{13}	58.7	64.7	66.9	65.3	68.7
C_{23}	57.9	65.6	67.6	66.2	69.7
C_{44}	27.1	37.6	41.5	41.6	45.1
C_{55}	27.8	38.7	41.8	42.3	45.6
C_{66}	27.0	40.6	46.2	45.9	49.1
E_{11}	74.0	110.2	122.2	121.7	128.5
E_{22}	75.0	105.5	118.8	117.5	125.1
E_{33}	73.5	99.6	108.1	108.8	115.5
ν_{12}	0.328	0.295	0.282	0.287	0.280
ν_{13}	0.351	0.325	0.324	0.314	0.315
ν_{23}	0.339	0.339	0.333	0.327	0.327
ν_{21}	0.332	0.283	0.274	0.277	0.272
ν_{31}	0.348	0.293	0.286	0.281	0.283
ν_{32}	0.332	0.320	0.303	0.303	0.302

Table 3.2: Ultrasonic measurement results for the 6061 Al/SiC$_p$ composites (unit=GPa except ν_{ij})

	PE-2045 0 %	PE-2047 20 %	PE-2731 30 %
C_{11}	112.5	162.9	166.1
C_{22}	113.1	157.8	163.2
C_{33}	111.6	147.9	153.0
C_{12}	57.5	66.4	67.5
C_{13}	58.3	67.3	67.9
C_{23}	58.5	66.6	68.2
C_{44}	26.4	41.6	44.1
C_{55}	26.7	42.5	44.7
C_{66}	25.8	45.7	47.7
E_{11}	73.2	122.1	125.5
E_{22}	73.6	118.0	122.6
E_{33}	71.5	108.4	113.1
ν_{12}	0.327	0.282	0.280
ν_{13}	0.351	0.328	0.319
ν_{23}	0.353	0.326	0.324
ν_{21}	0.328	0.273	0.274
ν_{31}	0.343	0.291	0.287
ν_{32}	0.343	0.300	0.299

Table 3.3: Ultrasonic measurement results for the 7091 Al/SiC$_p$ composites (unit=GPa except ν_{ij})

	PE-2730 0 %	PE-2711 10 %	PE-2712 20 %	PE-2665 30 %
C_{11}	112.9	129.5	152.0	167.4
C_{22}	113.4	126.6	146.7	166.5
C_{33}	112.2	123.2	138.8	156.3
C_{12}	56.9	60.0	64.7	68.0
C_{13}	58.0	60.4	65.2	67.6
C_{23}	57.7	60.6	65.1	68.8
C_{44}	26.7	31.0	37.7	45.3
C_{55}	27.2	31.6	38.3	45.9
C_{66}	26.4	32.2	41.1	49.0
E_{11}	74.2	90.4	111.4	127.4
E_{22}	74.9	87.6	106.6	125.6
E_{33}	72.8	84.3	99.1	116.7
ν_{12}	0.323	0.313	0.294	0.281
ν_{13}	0.351	0.336	0.332	0.309
ν_{23}	0.345	0.343	0.337	0.320
ν_{21}	0.326	0.303	0.281	0.277
ν_{31}	0.344	0.313	0.295	0.283
ν_{32}	0.336	0.330	0.313	0.298

such variables as material density, specimen dimension, sound velocity in water and transit times, accuracies of better than 1% are expected in these components for both contact and immersion measurements. When contact transducers are used to determine the shear stiffness components C'_{44}, C_{55} and C'_{66}, the same accuracy can be achieved. The accuracy of the off-diagonal components C'_{12}, C'_{13} and C'_{23}, however, seem to be less because these components are measured indirectly. Since these components are determined from the diagonal stiffness components and certain velocities, as shown in Equation (3.10), good accuracy in these quantities can only be achieved if high accuracy exists in the other parameters. Accuracy of the off-diagonal stiffness components has an effect on the Young's moduli and the Poisson's ratios.

In addition to being measured by the contact method, the shear moduli G_{12}, G_{13} and G_{23} were also measured by the oblique incidence immersion method, together with the off-diagonal stiffness components. Shear moduli measured by the immersion method were found to agree well with those of direct contact method. The results are compared in Figure 3.6. The excellent agreement between the two methods has lent confidence to the off-diagonal stiffness results obtained by oblique incidence immersion.

All the reinforced composite samples show orthotropic behavior. For each sample the elastic stiffness is highest along the extrusion direction x_1, next highest along the in-plane transverse direction x_2, and lowest along the out-of-plane transverse direction x_3. The differences between C_{11} and C_{33} for the 30% SiC_p samples in the composite systems of 2124, 6061 and 7091 aluminum are about 9%, 9% and 7%, respectively. Young's moduli show similar anisotropic behaviors and their differences between E_{11} and E_{33} for the 30% samples in the three alloy systems are about 11%,

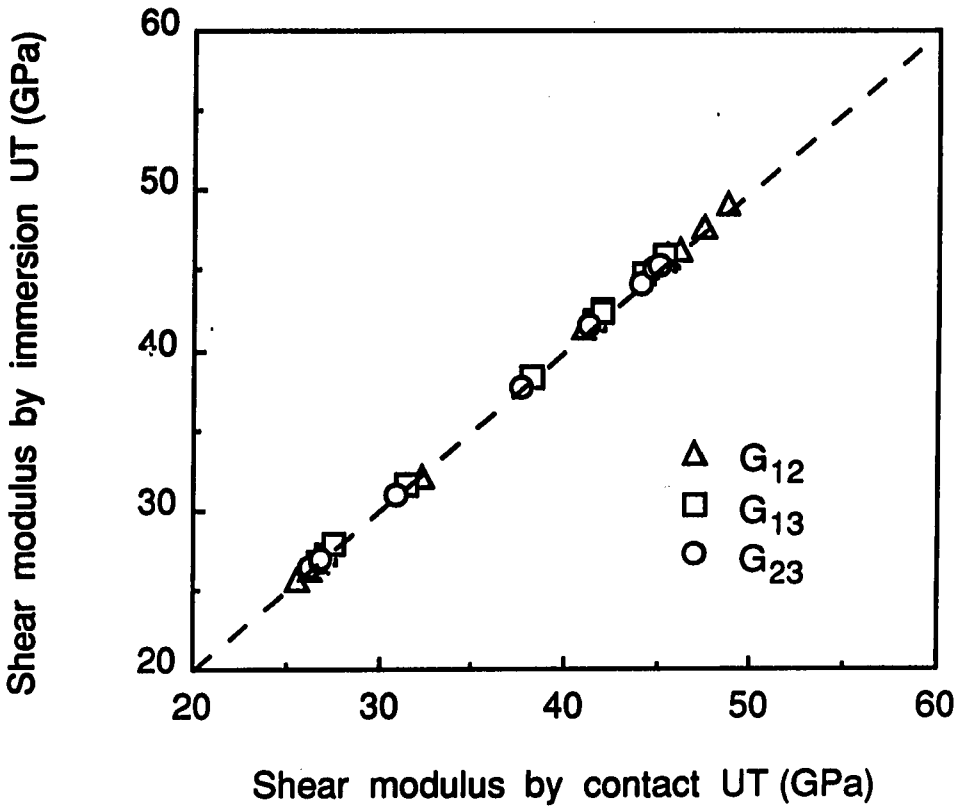

Figure 3.6: Comparison of shear moduli measured by ultrasonic immersion method with those obtained by direct contact method

11% and 9%, respectively. Within the extrusion plane, however, the elastic constants are different only by a few percent. Consequently the shear stiffness $C'_{66}(= G_{12})$ has the highest value, and $C'_{55}(= G_{13})$ and $C'_{44}(= G_{23})$ are almost the same. The differences between G_{12} and G_{23} for the 30% SiC_p samples in the 2124, 6061 and 7091 alloy systems are about 9%, 8% and 8%, respectively.

All elastic constants, except for the Poisson's ratios, increase with increasing volume fraction of SiC_p in the three alloy systems. The rate of increase is not linear, especially for Young's moduli and the diagonal stiffness components. These observations are consistent with previous work [98,99]. Compared with unreinforced samples, C'_{11}, G_{12} and E_{11} of the 30% samples in each system show an increase of more than 45%, 80% and 70%, respectively. Experimental data for elastic moduli of Al/SiC_p composites are sparse in the literature. Although it is hard to compare the present results with published data without detailed information on the microstructure, the ultrasonically measured data compared well with other experimental data obtained by different ultrasonic techniques [28] and tensile tests [98-100].

The off-diagonal stiffness components also show increase with increasing volume content of SiC_p. The difference between these components in each sample is less than 2%. With 30% reinforcement of SiC_p, these off-diagonal stiffness components increase by about 17-20%. The highest anisotropy of Poisson's ratios occurs between ν_{23} and ν_{21} in each series of composites. The difference between these two components in the 30% SiC_p samples of the 2124, 6061 and 7091 Al alloy systems are about 20%, 18% and 16%, respectively. Poisson's ratios decrease with increasing volume fraction of SiC_p and the maximum decrease occurs in ν_{31} in each alloy system; the decrease is about 20-23% at a SiC_p loading level of 30%.

The ultrasonic velocity measurements seem to be sensitive to the presence of internal defects like intermetallic compounds or porosity. The intermetallic compounds are known to be very stiff; a high content of intermetallic compounds is therefore expected to increase the elastic constants. Porosity, on the other hand, should decrease the elastic stiffness. According to the microstructural analysis (Table 5.1), the 20% SiC_p sample in the 6061 Al series (PE-2047) exhibited about 15% volume fraction of intermetallic compounds. The elastic constants of this sample are almost the same as those for 25% SiC_p samples in the 2124 Al series. The 30% SiC_p sample in the 7091 Al series (PE-2713) contains higher porosity compared with the same volume fraction samples of the same base alloy (PE-2665). The elastic stiffnesses of the sample PE-2713 was shown to be very inhomogeneous and they were generally lower than those of PE-2665 by about 4-5%.

The SiC_p free (unreinforced) samples in each alloy system show also an orthotropic behavior. The elastic stiffnesses C_{11}, C_{22} and C_{33} of in each series of base alloys are isotropic to within 1%. On the other hand, differences between the components of the off-diagonal stiffness, shear stiffness and Young's modulus in each alloy system are less than 3%. Poisson's ratios show most dominant anisotropic behavior. The highest anisotropy occurs between ν_{13} and ν_{12} and their difference is about 7-9% in each alloy system. The anisotropy in the unreinforced Al alloys may be caused by the texture as a result of the extrusion or by the anisotropic distribution of intermetallic compounds. The anisotropic properties in these samples are considerably small compared to the maximum anisotropy observed in the SiC_p reinforced samples.

4. TENSILE TESTS

Tensile specimens fabricated from each composite plate included both LT (longitudinal loading-transverse crack) and TL (transverse loading-longitudinal crack) types. Each specimen had a gage section 2.54 mm thick, 12.7 mm wide and 25.4 mm long. The LT specimens provided the longitudinal tensile properties parallel to the extrusion direction, while the TL specimens gave the transverse properties which were 90 degree to the extrusion direction. Tensile tests were conducted at room temperature using a screw-driven machine. The loading rate was 0.25 mm/min. A strain gage was mounted at the center of the gage section to measure the strain during tensile tests. The measured Young's moduli are given in Table 4.1.

Table 4.1 shows that Young's modulus E_{11} is in general higher than E_{22} and that the difference between the Young's moduli from mechanical tests is larger than the difference between the Young's moduli deduced from the ultrasonic test results. It is also noticed that E_{11} of the 20% SiC_p sample in the 6061 Al series (PE-2047) and E_{22} of the 30% SiC_p sample in the 2124 Al series (PE-2488) are considerably lower than those of ultrasonic results. The discrepancy between the ultasonic data and the tensile test data for these two samples is not known; it may be caused by variations in the tensile tests and material properties. When measuring Young's modulus of short fiber MMCs by tensile test, difficulties can be encountered as a

Table 4.1: Tensile test results (unit=GPa)

Base alloy	Billet number	E_{11}	E_{22}
2124 Al	PE-2600	68.5	70.4
2124 Al	PE-3025-1	NA	NA
2124 Al	PE-2404	121	111
2124 Al	PE-2229	119	109
2124 Al	PE-2488	124	110
6061 Al	PE-2045	71.7	70.2
6061 Al	PE-2047	105	113
6061 Al	PE-2099	114	104
6061 Al	PE-2731	123	116
7091 Al	PE-2730	73.9	71.3
7091 Al	PE-2711	87.3	82.8
7091 Al	PE-2712	109	98.9
7091 Al	PE-2713	115	119
7091 Al	PE-2665	121	117

result of the reduced linear elastic range [101]. The ultrasonically measured Young's moduli are compared with the tensile test results in Figure 4.1. They generally agree within several percent except for PE-2047 and PE-2488.

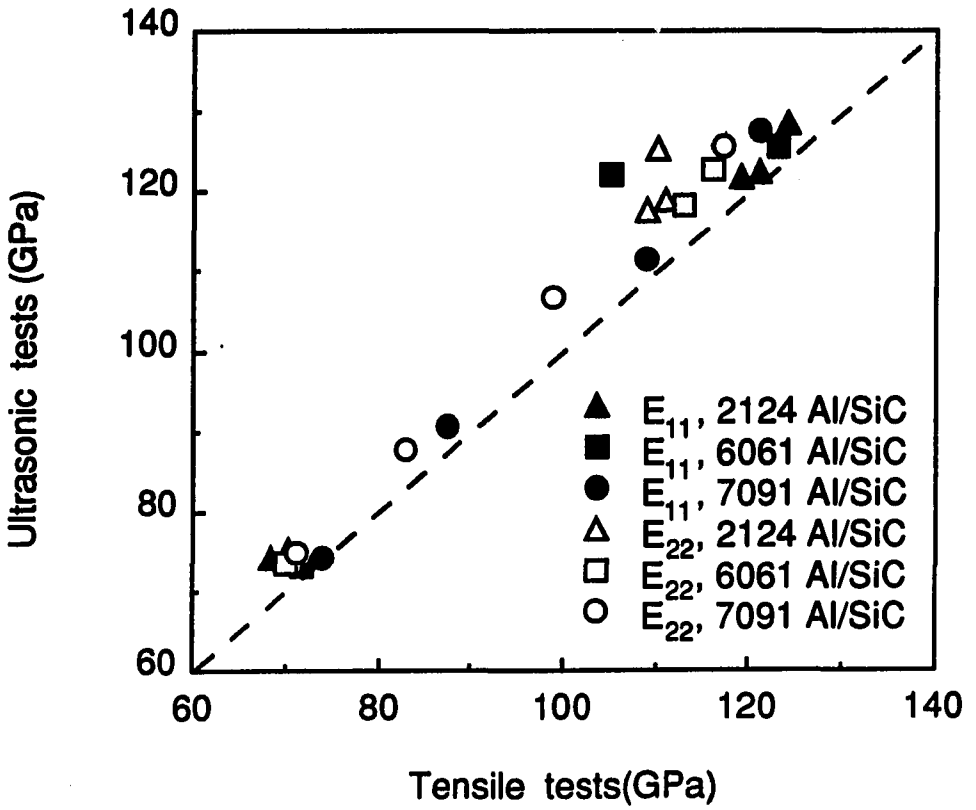

Figure 4.1: Comparison of Young's moduli measured by ultrasonic method and those obtained by tensile tests

5. MICROSTRUCTURAL ANALYSIS

Metallographic specimens were prepared for microstructural characterization using scanning electron microscopy (SEM). The initial polishing was performed using 240 to 600 grit emery paper. Fine diamond paste was subsequently employed to further polish the specimen to 1 μm finish. The final polishing was accomplished using cerium oxides with a particle size of approximately 0.05 μm. The SEM photographs of metallographic specimens were taken using both secondary electron and backscattered electron imaging techniques. The SEM micrographs were used to obtain the average size of SiC_p and the amounts of intermetallics and porosity.

To examine the particle characteristics such as shape, aspect ratio and orientation distribution of SiC_p, additional specimens were prepared. Three pieces of specimens were cut from one % (PE-2712) and two 30 % (PE-2713 and PE-2665) 7091 Al composites with their faces parallel to the material symmetry planes. Optical micrographs were taken at several representative locations on each face and these micrographs were then analyzed using an image analysis system. Attention was given to the shape, aspect ratio and orientation distribution of SiC_p on these cut sections. The aspect ratio (l/d) of SiC particles was determined by the maximum length (major axis) of each particle divided by its perpendicular width. The aspect ratio distribution was then found in terms of the percentage of particle number. The

orientation of SiC particles on the three symmetry planes were obtained by measuring the angle of the major axis of each particle with respect to particular directions. The angle ϕ measured the orientation of the major axis of each particle on the extrusion plane from the x_1 axis while the angle θ measured the orientation of particles on the x_1-x_3 and x_2-x_3 planes from the x_3 axis as shown in Figure 3.1. The orientation distribution was also found by the percentage of particle number.

5.1 SEM Metallographic Examinations

Metallographic examination revealed SiC_p, intermetallic compounds and porosity [14]. The quantitative measurement results of these features are presented in Table 5.1.

The average size of SiC_p varied approximately from 2 to 4 μm for the three alloy series of composites. It appeared that in each alloy series the average particle size was slightly larger for the samples with the greater volume percentages of SiC_p. The volume percentages of SiC_p measured from the micrographs were found to be in good agreement with the nominal percentages.

All of the composites, including the 0% SiC_p (unloaded) samples, showed some presence of intermetallic compounds; the amount ranged from about 2 to 15% by volume. In each series of the three alloy systems, considerable variation in the volume fraction of intermetallic compounds was observed. In particular the 20 v/o SiC_p composite (PE-2047) in the 6061 alloy series exhibited an unusually large volume percentage of intermetallic compounds as compared to other composites.

Porosity was often observed in the composites with 30 % SiC_p loading. The volume percentage of porosity varied from 1.6 to 4.2 %. The porosity was generally

Table 5.1: Microstructural characteristics of Al/SiC_p composites

Base alloy	Billet number	Intermetallic compounds(v/o)	Porosity (v/o)	SiC_p size(μm)
2124 Al	PE-2600	7.4±1.7	0	0
2124 Al	PE-2404	4.4±2.8	0	2.5±1.8
2124 Al	PE-2229	10.0±3.9	0	2.4±1.5
2124 Al	PE-2488	6.7±3.7	1.4±1.8	3.9±2.9
6061 Al	PE-2045	5.2±2.2	0	0
6061 Al	PE-2047	15.5±4.8	0	2.3±1.8
6061 Al	PE-2099	2.9±2.2	0	2.6±1.7
6061 Al	PE-2731	1.2±2.1	2.6±2.3	2.8±1.7
7091 Al	PE-2730	6.9±2.6	0	0
7091 Al	PE-2711	6.9±2.8	0.5±0.9	2.4±1.2
7091 Al	PE-2712	4.4±2.6	0	2.3±1.5
7091 Al	PE-2713	3.2±1.1	4.2±2.8	3.5±2.8
7091 Al	PE-2665	6.9±2.8	1.6±1.4	3.7±2.1

found to be present at the interface between SiC_p and base alloy.

5.2 Image Analysis Results

The optical micrographs taken on the three symmetry planes of the 30% SiC_p sample (7091 Al, PE-2665) are shown in Figures 5.1-5.3, where symmetry axes are indicated. At a glance, the SiC particles are shaped somewhat irregularly. On the x_1-x_2 plane (extrusion plane), they tend to be relatively round, while on the other two planes the particles tend to be long and narrow.

The aspect ratio distributions are shown in Figures 5.4-5.6 for the 30% SiC_p sample (PE-2665). They seem to have similar distribution histograms on the three symmetry planes and the aspect ratio range from 1 to 6. The mean value of the aspect ratio on the three symmetry planes of 7091 Al/SiC_p samples are listed in

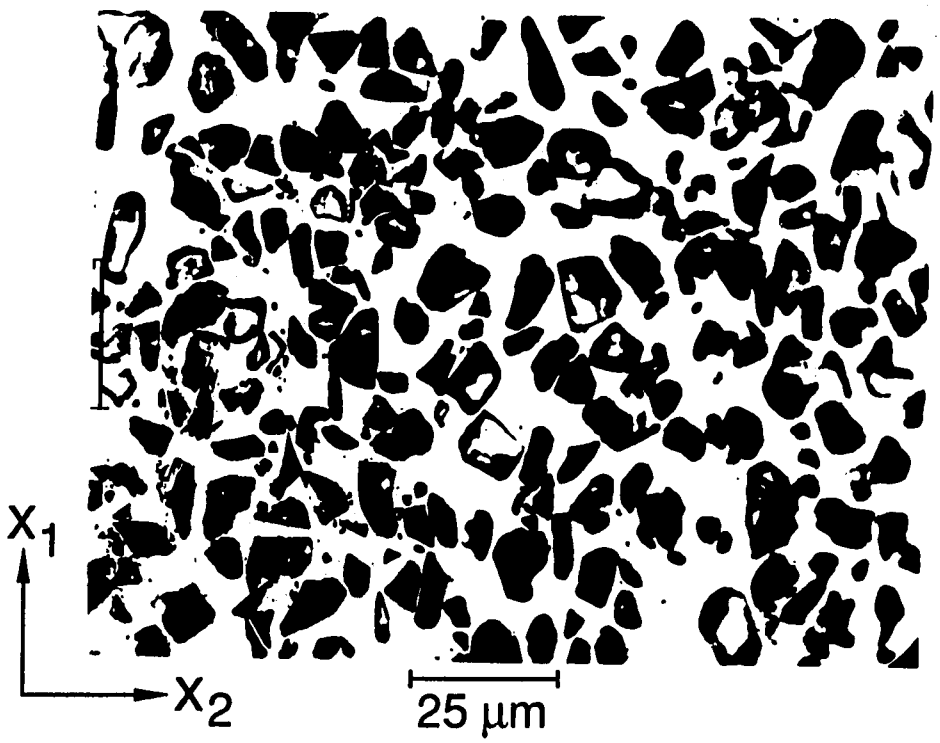

Figure 5.1: Photomicrograph taken on the x_1-x_2 plane of 30% SiC_p/7091 Al (PE-2665)

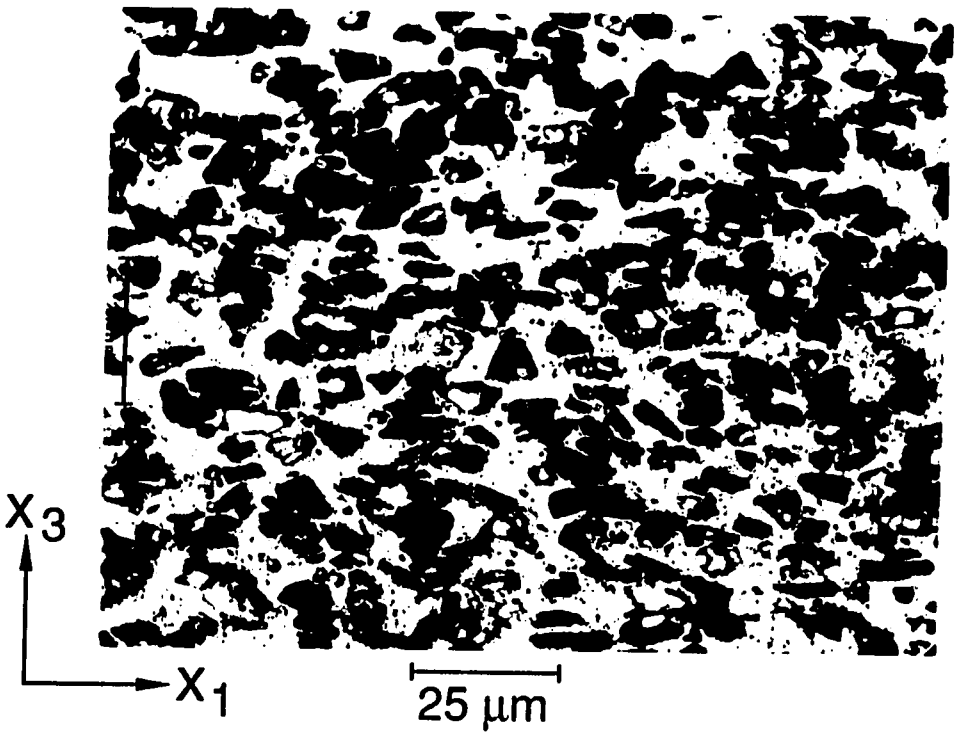

Figure 5.2: Photomicrograph taken on the x_1-x_3 plane of 30% SiC$_p$/7091 Al (PE-2665)

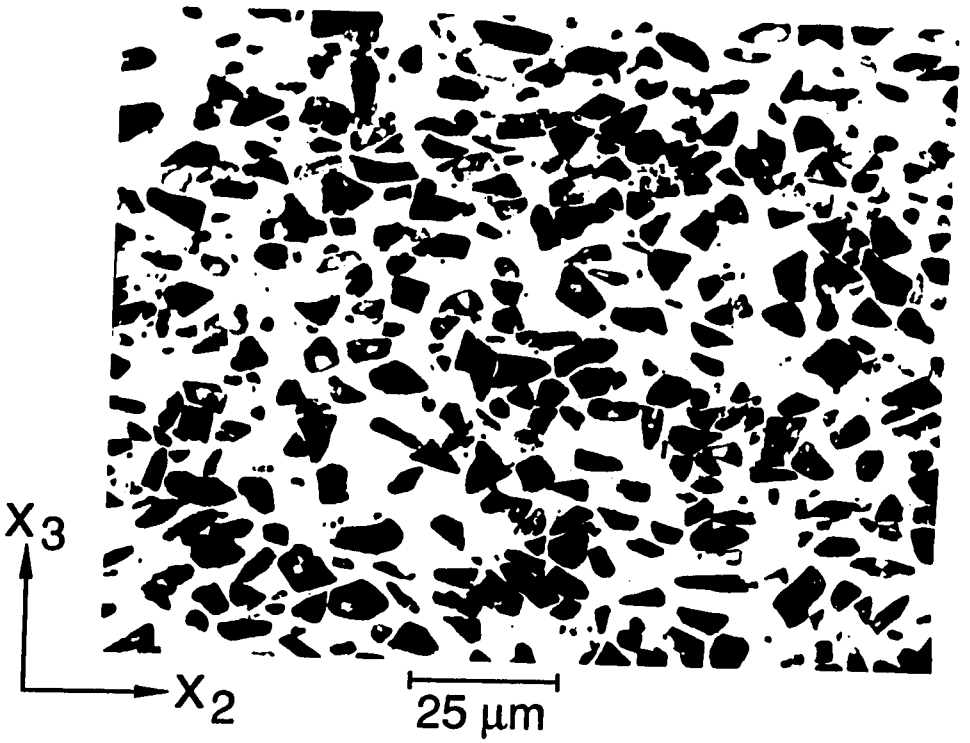

Figure 5.3: Photomicrograph taken on the x_2-x_3 plane of 30% SiC$_p$/7091 Al (PE-2665)

Table 5.2: Average aspect ratio of SiC_p on three symmetry planes

Base alloy	Billet number	SiC_p aspect ratio x_1-x_2 plane	x_1-x_3 plane	x_2-x_3 plane
7091 Al	PE-2712	NA	3.2±1.2	3.4±1.4
7091 Al	PE-2713	2.7±0.8	3.0±1.2	3.1±1.0
7091 Al	PE-2665	2.6±0.8	3.0±1.0	3.2±1.0

Table 5.2.

Table 5.2 shows that the average aspect ratio on the x_1-x_3 and x_2-x_3 planes are in general slightly higher than that on the x_1-x_2 plane.

Quantitative information on the particulate orientation distribution was also obtained from the image analysis of the micrographs of the three symmetry planes. The orientation of a particle in a plane was specified by the angle between its major axis and a selected symmetry axis in that plane. Figures 5.7-5.9 show the orientation of the particulates in the 30% SiC_p/7091 Al sample (PE-2665). The orientation distribution in the extrusion plane (x_1-x_2 plane) is shown in Figure 5.7. The orientation in the extrusion plane is usually random, while a very slight tendency to align along the extrusion direction in some sample. In the other two symmetry planes, however, the distribution showed a pronounced preference for the particles to lie down in the extrusion plane. Figures 5.8 and 5.9 show, respectively, the orientation distribution in the x_1-x_3 and the x_2-x_3 planes. Similar orientation behavior was also found in the image analysis of micrographs on two other samples; these are PE-2712 (20% SiC_p, 7091 Al) and PE-2713 (30% SiC_p, 7091 Al). The preferred orientation distribution of the particulates, evidently the result of the extrusion process, has an important effect on the anisotropic elastic properties of the material as already mentioned in the general introduction of the thesis. An examination of the elastic constants mea-

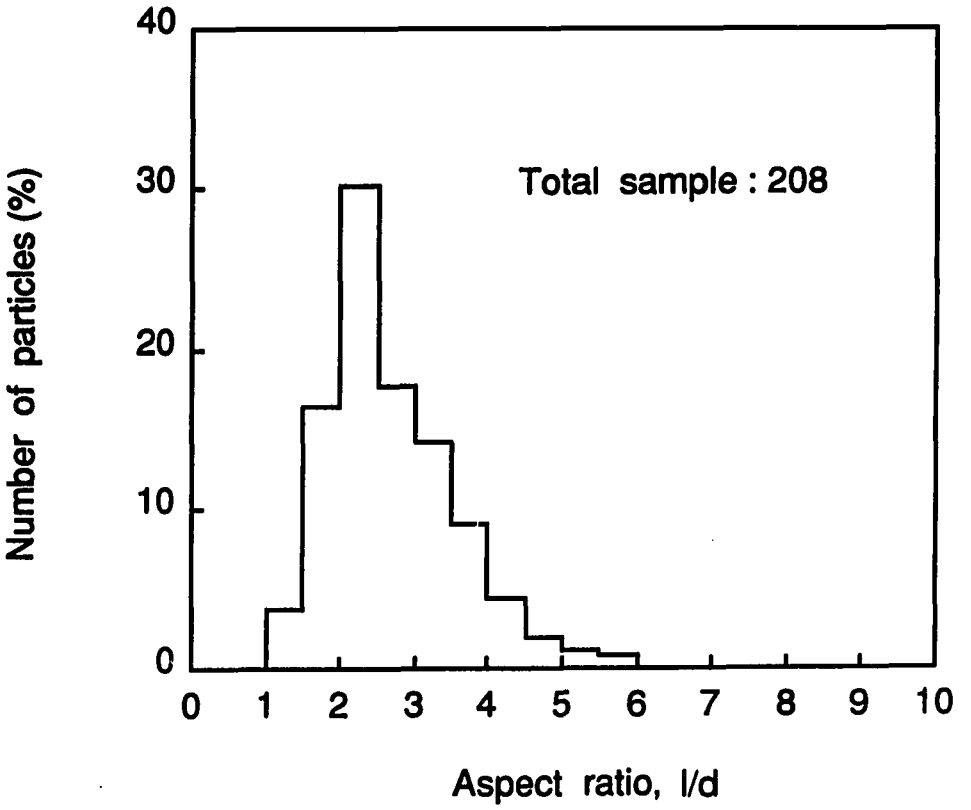

Figure 5.4: SiC_p aspect ratio distribution on the x_1-x_2 plane of 30% SiC_p/7091 Al sample (PE-2665)

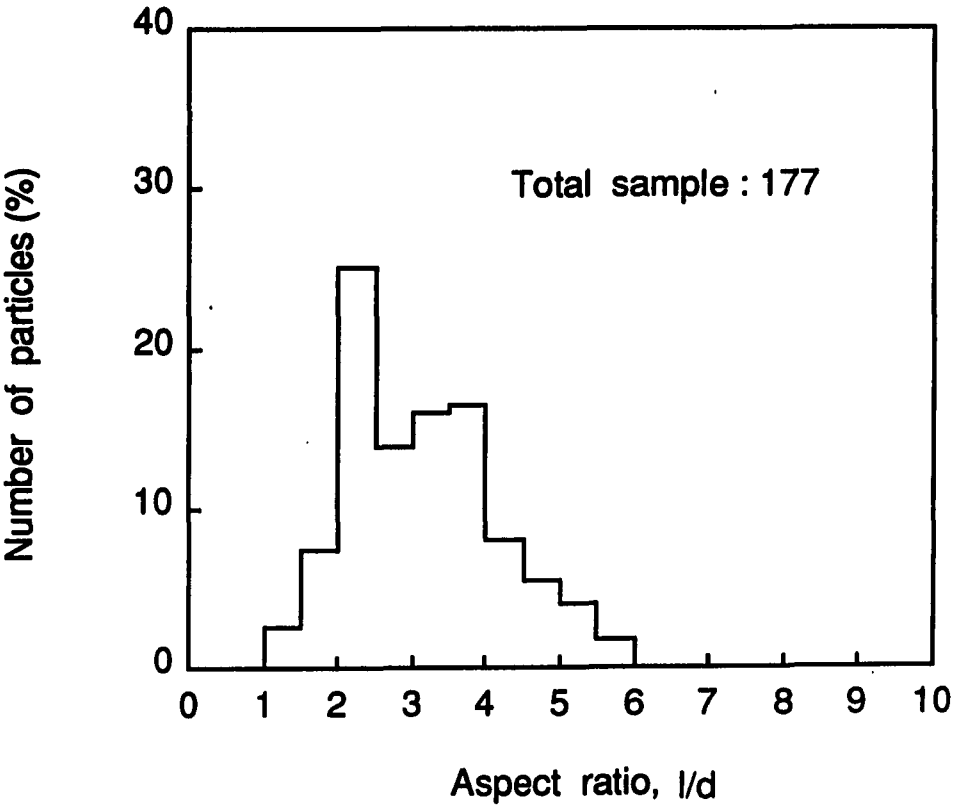

Figure 5.5: SiC_p aspect ratio distribution on the x_1-x_3 plane of 30% SiC_p/7091 Al sample (PE-2665)

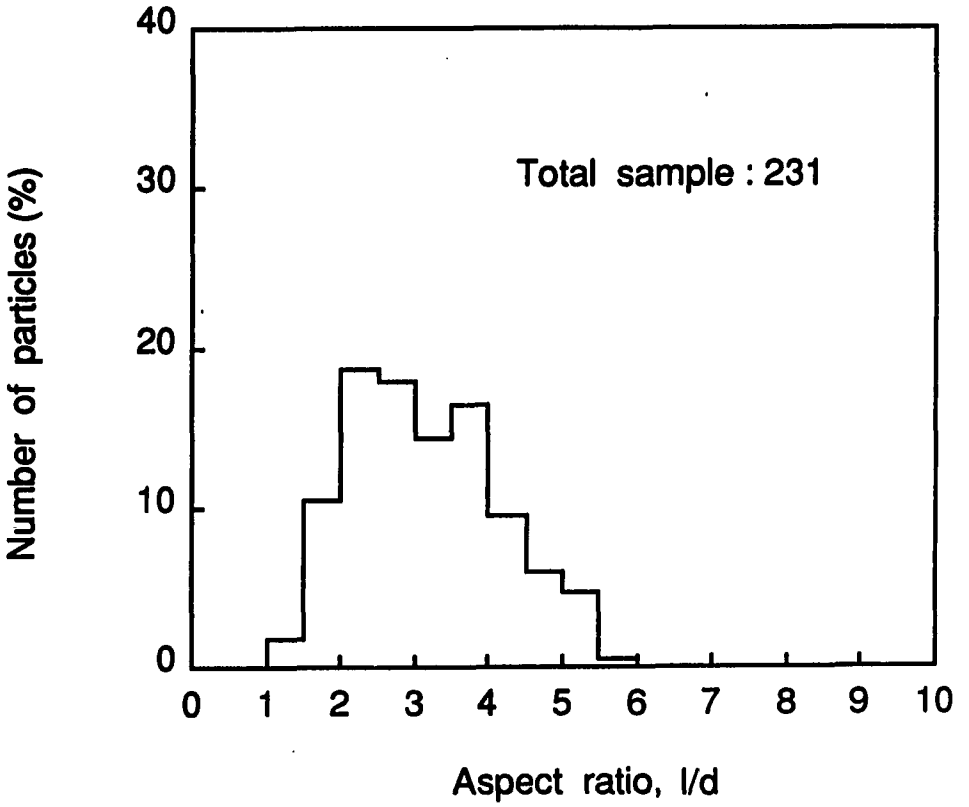

Figure 5.6: SiC_p aspect ratio distribution on the x_2-x_3 plane of 30% SiC_p/7091 Al sample (PE-2665)

sured ultrasonically shows that the elastic property anisotropy is consistent with the particle orientation behavior.

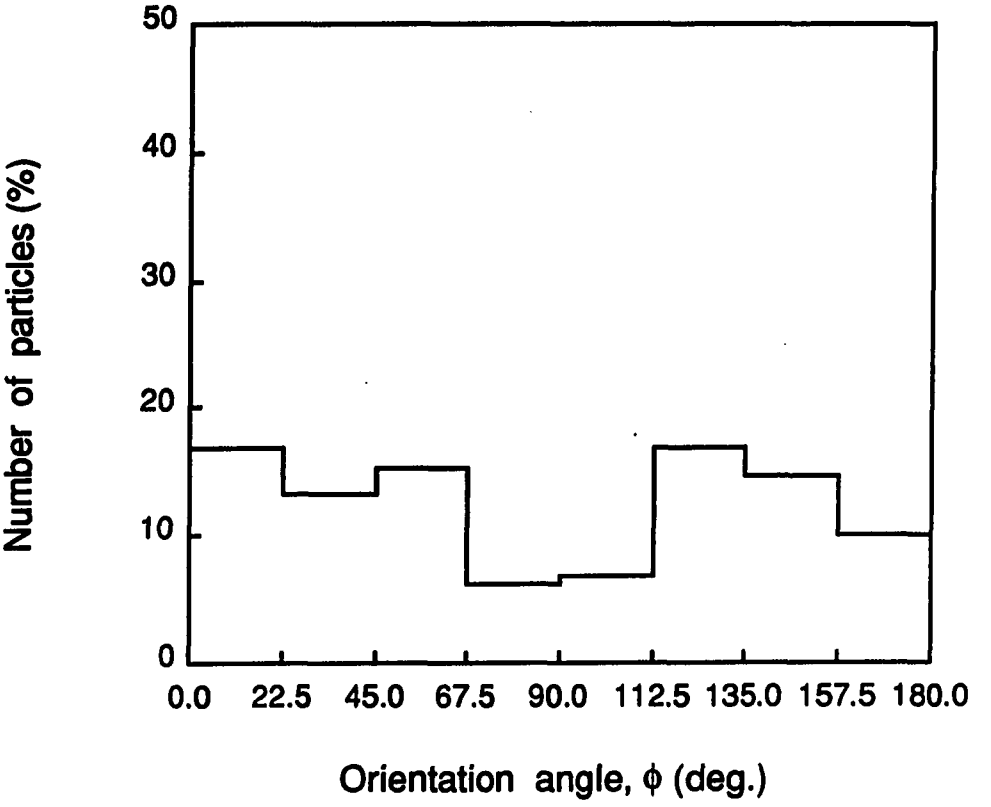

Figure 5.7: SiC_p orientation distribution on the x_1-x_2 plane of 30% SiC_p/7091 Al sample (PE-2665)

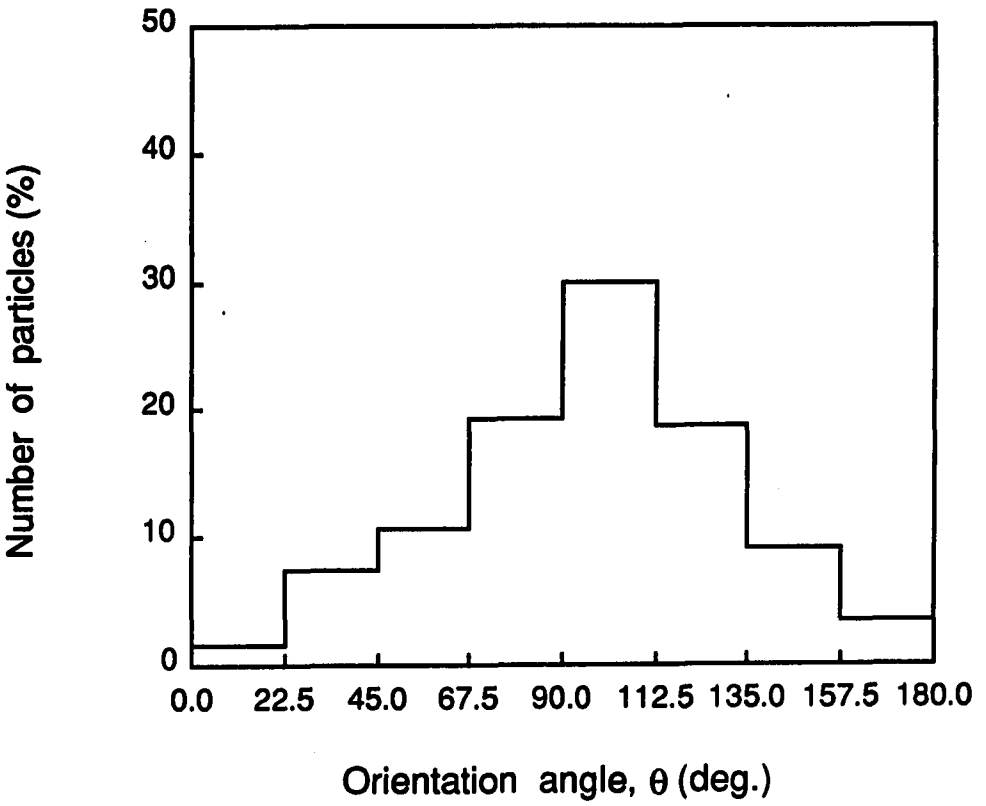

Figure 5.8: SiC_p orientation distribution on the x_1-x_3 plane of 30% SiC_p/7091 Al sample (PE-2665)

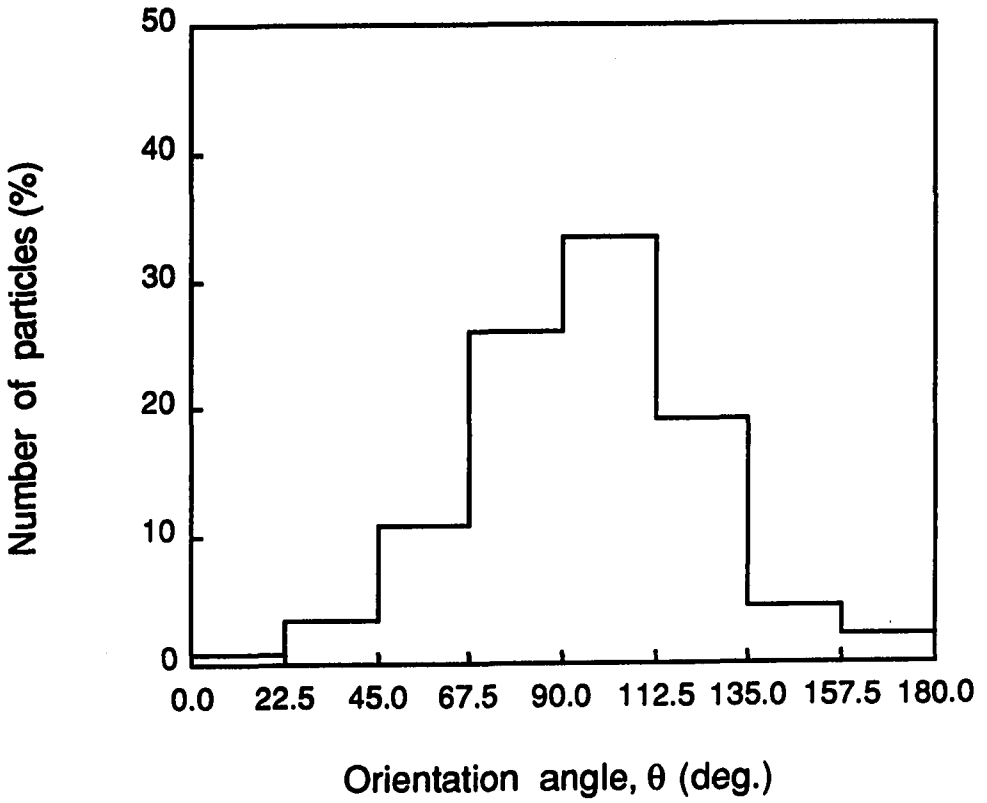

Figure 5.9: SiC_p orientation distribution on the x_2-x_3 plane of 30% SiC_p/7091 Al sample (PE-2665)

6. THEORETICAL PREDICTION

Among various theoretical models for predicting the overall elastic moduli of short fiber reinforced composites, the one based on the equivalent inclusion principle of Eshelby [47] and the concept of average stress or average strain in the matrix by Mori-Tanaka [48] have been employed widely for composites containing a finite volume fraction of ellipsoidal fibers. The model usually involved the explicit calculation of eigenstrain (transformation strain) or average strain of the matrix in specific loading directions to obtain the overall engineering constants [49-58]. By considering a relationship between the average strain of the fiber and the imposed uniform strain at the boundary, Benveniste [59] proposed a closed form expression of effective stiffness tensor for composites containing aligned or randomly oriented particles. Within the framework of Benveniste's approach Ferrari and Johnson [102] used a harmonic method to treat the probability density function of arbitrarily oriented short fibers.

The mathematical model we have used to predict the effective elastic stiffness of Al/SiC_p composites consists of an isotropic matrix containing a finite volume fraction of arbitrarily oriented ellipsoidal particles, which are isotropic and all of the same size, as shown in Figure 6.1.

The strategy we have used here for deriving the effective stiffness of the model can be summarized as follows:

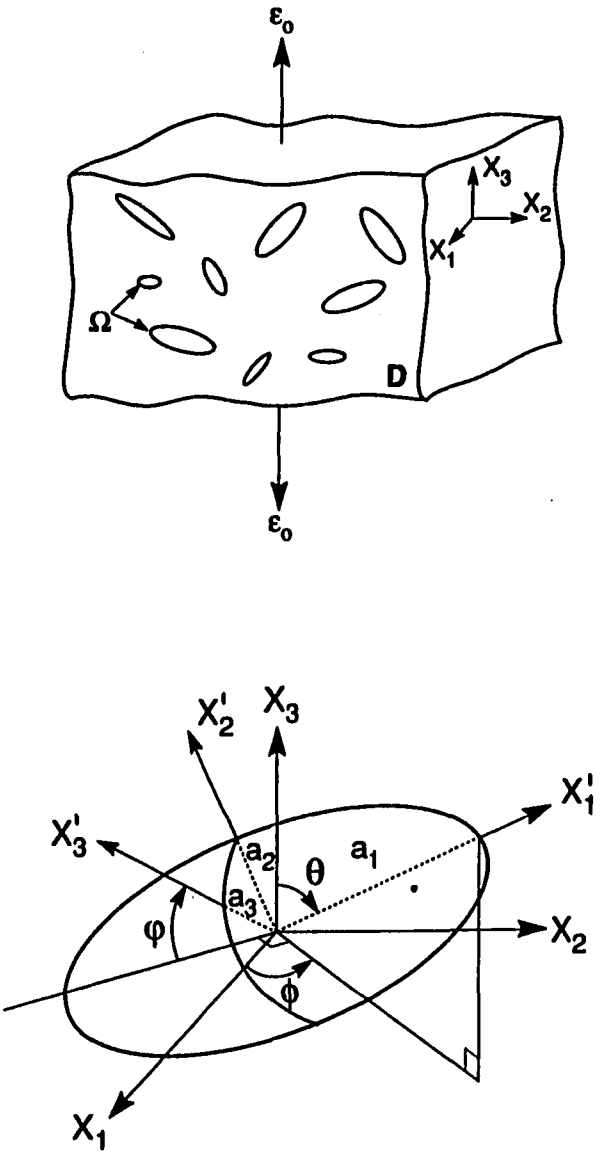

Figure 6.1: Mathematical model to predict effective stiffness of a composite containing ellipsoidal particles

1. Employ the Mori-Tanaka's average stress in the matrix and Eshelby's equivalence inclusion idea to obtain a solution for the average perturbed strain ($\tilde{\boldsymbol{\epsilon}}$) and the average perturbed stress ($\tilde{\boldsymbol{\sigma}}$) of the matrix as a result of a homogeneous displacement boundary condition corresponding to $\boldsymbol{\epsilon}_0$.

2. Therefore evaluate the volume average of the strain and the stress over matrix phase as well as the orientation dependent average strain and stress over fiber phase.

3. Compute the relation between the orientation dependent eigenstrain ($< \boldsymbol{\epsilon}^* >$) and the applied strain $\boldsymbol{\epsilon}_0$. The evaluation of $< \boldsymbol{\epsilon}^* >$ is central to the derivation of a closed form tensor expression for effective stiffness.

4. Find a corresponding closed form matrix expression of effective stiffness for easier numerical calculation.

Both symbolic and indicial notations will be used in the formulation. Bold-face lowercase letters denote second-rank tensors, and capital letters denote the fourth-rank tensors. The inner product of two tensors is written such that $\boldsymbol{\sigma\epsilon} = \sigma_{im}\epsilon_{mj}$, $\boldsymbol{C\epsilon} = C_{ijkl}\epsilon_{kl}$ and $\boldsymbol{CS} = C_{ijmn}S_{mnkl}$. Superscripts "f" and "m" refer to quantities pertaining to the fiber and the matrix, respectively. The fiber volume fraction and the matrix volume fraction are denoted respectively by ν_f and ν_m where $\nu_f + \nu_m = 1$. The isotropic stiffness tensors of the matrix and the fiber are denoted by $\boldsymbol{C}_m$ and $\boldsymbol{C}_f$, respectively and the corresponding compliance tensors are $\boldsymbol{C}_m^{-1}$ and $\boldsymbol{C}_f^{-1}$.

6.1 Derivation of the Effective Stiffness

Let the domains of the infinite elastic body and the fibers be denoted by D and Ω, respectively. The domain of the matrix thus becomes $D - \Omega$.

Consider a typical fiber depicted in Figure 6.1. The local axes of the fiber

are denoted by the primed coordinate system $x_1^{'},x_2^{'},x_3^{'}$ and the global axes by the unprimed one. The principal axes of the ellipsoidal fiber along the $x_1^{'}$, $x_2^{'}$ and $x_3^{'}$, respectively, are denoted by a_1, a_2 and a_3 and their magnitudes follow the order $a_1 > a_2 > a_3$. Denoting a_{ij} as the direction cosine between the ith primed and jth unprimed axes,

$$\boldsymbol{a} = \begin{bmatrix} sin\theta cos\phi & sin\theta sin\phi & cos\theta \\ -cos\theta cos\phi cos\varphi - sin\phi sin\varphi & -cos\theta sin\phi cos\varphi + cos\phi sin\varphi & sin\theta cos\varphi \\ -cos\theta cos\phi sin\varphi + sin\phi cos\varphi & -cos\theta sin\phi sin\varphi - cos\phi cos\varphi & sin\theta sin\varphi \end{bmatrix} \tag{6.1}$$

Now the composite is subjected to the boundary displacement at infinity to give rise to a homogeneous strain $\boldsymbol{\epsilon}_0$. Compared to the single inclusion problem, the average strain of the matrix in the composite at a finite concentration of fibers will be different from $\boldsymbol{\epsilon}_0$ by a perturbed strain. If the average perturbed strain in the matrix due to the presence of all fibers is denoted by $\tilde{\boldsymbol{\epsilon}}$, which corresponds to an averaged perturbed stress $\tilde{\boldsymbol{\sigma}}$, the average of the total strain and that of the total stress of the matrix in the composite are, respectively

$$\bar{\boldsymbol{\epsilon}}^m = \boldsymbol{\epsilon}_0 + \tilde{\boldsymbol{\epsilon}} \tag{6.2}$$

$$= \boldsymbol{C}_m^{-1}(\boldsymbol{\sigma}_0 + \tilde{\boldsymbol{\sigma}}), \tag{6.3}$$

$$\bar{\boldsymbol{\sigma}}^m = \boldsymbol{\sigma}_0 + \tilde{\boldsymbol{\sigma}} \tag{6.4}$$

$$= \boldsymbol{C}_m(\boldsymbol{\epsilon}_0 + \tilde{\boldsymbol{\epsilon}}). \tag{6.5}$$

Following Mori-Tanaka's theory [48], a single fiber is introduced into the composite D. The orientation of this fiber is defined by the Euler angles ϕ, θ and φ as

shown in Figure 6.1. Since the fiber is now embedded in the matrix, its strain and stress state, depending on the specific orientation, will differ from those of surrounding matrix by a further perturbation, say, ϵ^{pt} and σ^{pt}. The Eshelby's equivalent inclusion principle [47] can then be applied to this fiber. By means of this principle, the strain and stress within the fiber can be written as

$$\bar{\epsilon}^f = \epsilon_0 + \tilde{\epsilon} + \epsilon^{pt} \tag{6.6}$$

$$= C_f^{-1}(\sigma_0 + \tilde{\sigma} + \sigma^{pt}) = C_m^{-1}(\sigma_0 + \tilde{\sigma} + \sigma^{pt} - \sigma^*), \tag{6.7}$$

$$\bar{\sigma}^f = \sigma_0 + \tilde{\sigma} + \sigma^{pt} \tag{6.8}$$

$$= C_f(\epsilon_0 + \tilde{\epsilon} + \epsilon^{pt}) = C_m(\epsilon_0 + \tilde{\epsilon} + \epsilon^{pt} - \epsilon^*) \tag{6.9}$$

where σ^* and ϵ^* are eigenstress and eigenstrain, respectively, which have nonvanishing components in Ω, but become zero outside Ω. Since the added single fiber can be treated as any fiber in the composite, the above relations hold for any fiber. While ϵ_0, $\tilde{\epsilon}$, σ_0 and $\tilde{\sigma}$ are common for all fibers, ϵ^{pt}, ϵ^*, σ^{pt} and σ^* are orientation dependent.

It is convenient to write Equations (6.6)-(6.9) in the local coordinate system in order to use known relations. Instead of repeating these equations in the local primed coordinate system, we shall refer to them as $(\ )'$; for example, Equation $(6.6)'$ refer to Equation (6.6) in the local coordinate system, i.e. $\bar{\epsilon}^{f\prime} = \epsilon_0' + \tilde{\epsilon}' + \epsilon^{pt\prime}$. The perturbed stress $\sigma^{pt}{}'$ and strain $\epsilon^{pt}{}'$ in the local coordinates are further related to the eigenstress and eigenstrain by

$$\sigma^{pt}{}' = R\sigma^*{}', \tag{6.10}$$

$$\epsilon^{pt}{}' = S\epsilon^*{}' \tag{6.11}$$

where $\boldsymbol{R}$ is Hill's tensor [103] and $\boldsymbol{S}$ is Eshelby's tensor [47]. From the last terms of Equations $(6.7)'$ and $(6.9)'$, it can be shown that

$$\boldsymbol{\sigma}^{*'} = -\boldsymbol{C}_m \boldsymbol{\epsilon}^{*'}. \tag{6.12}$$

It is useful to find the relation between $\bar{\boldsymbol{\epsilon}}^{f'}$ and $\bar{\boldsymbol{\epsilon}}^{m'}$. One obtains from Equations $(6.2)'$ and $(6.6)'$ that

$$\bar{\boldsymbol{\epsilon}}^{f'} = \bar{\boldsymbol{\epsilon}}^{m'} + \boldsymbol{S}\boldsymbol{\epsilon}^{*'}. \tag{6.13}$$

Equation $(6.9)'$ can be written as

$$\boldsymbol{C}_f \bar{\boldsymbol{\epsilon}}^{f'} = \boldsymbol{C}_m(\bar{\boldsymbol{\epsilon}}^{f'} - \boldsymbol{\epsilon}^{*'}). \tag{6.14}$$

Solving Equation (6.14) for $\boldsymbol{\epsilon}^{*'}$ and substituting into Equation (6.13), one obtains

$$\bar{\boldsymbol{\epsilon}}^{f'} = \boldsymbol{T}' \bar{\boldsymbol{\epsilon}}^{m'} \tag{6.15}$$

where

$$\boldsymbol{T}' = [\boldsymbol{I} + \boldsymbol{S}\boldsymbol{C}_m^{-1}(\boldsymbol{C}_f - \boldsymbol{C}_m)]^{-1} \tag{6.16}$$

and $\boldsymbol{I}$ is the identity tensor. The tensor $\boldsymbol{T}'$ is known as Wu's tensor and its components can be found in [104]. $\boldsymbol{T}'$ holds symmetry properties of

$$T'_{ijkl} = T'_{jikl} = T'_{ijlk}. \tag{6.17}$$

Wu's tensor in the global coordinate system can be found through the usual tensor transformation

$$T_{ijkl} = a_{mi}a_{nj}a_{ok}a_{pl}T'_{mnop}. \tag{6.18}$$

The tensor $\boldsymbol{T}'$ can also be written in a different form. By rewriting Equation $(6.9)'$ as

$$\boldsymbol{C}_f(\bar{\boldsymbol{\epsilon}}^{m'} + \boldsymbol{\epsilon}^{pt'}) = \boldsymbol{C}_m(\bar{\boldsymbol{\epsilon}}^{m'} + \boldsymbol{\epsilon}^{pt'} - \boldsymbol{\epsilon}^{*'}), \tag{6.19}$$

one can then solve for $\epsilon^{*'}$ in terms of $\bar{\epsilon}^{m'}$ and substitute into Equation (6.13) to obtain the other form of $\boldsymbol{T}'$:

$$\boldsymbol{T}' = \boldsymbol{I} - \boldsymbol{S}[(\boldsymbol{C}_f - \boldsymbol{C}_m)\boldsymbol{S} + \boldsymbol{C}_m]^{-1}(\boldsymbol{C}_f - \boldsymbol{C}_m). \tag{6.20}$$

Consider now the volume average of the total strain in the composite,

$$\bar{\epsilon} = \frac{1}{V_D}\int_D \epsilon dV = \frac{1}{V_D}\int_{D-\Omega} \epsilon dV + \frac{1}{V_D}\int_{\Omega} \epsilon dV \tag{6.21}$$

where V_D denotes the volume of domain D and the overbar represents the volume average. Since the strain in the matrix does not depend on the orientation, the first integration simply becomes $\nu_m \bar{\epsilon}^m$ where ν_m is denoted by $(D - \Omega)/V_D$. However, the second integration in Equation (6.21) should be conducted over all possible orientations, since the ellipsoidal particles of the same size are arbitrarily oriented in the Ω. This can be accomplished by the orientation distribution function (ODF) weighted integration in the Euler space. Denoting V as the volume of the single fiber and $\rho(\phi, \theta, \varphi)$ as ODF, the volume integral in the Ω domain is

$$\frac{1}{V_D}\int_{\Omega} \bar{\epsilon}^f dV = \frac{1}{V_D}\int_0^{\phi=2\pi}\int_0^{\theta=\pi}\int_0^{\varphi=2\pi} \bar{\epsilon}^f \rho(\phi, \theta, \varphi) V dS \tag{6.22}$$

where the infinitesimal surface area is $dS = \sin\theta d\phi d\theta d\varphi$. The volume fraction of the fibers can be defined by

$$\nu_f = \frac{1}{V_D}\int_{\Omega} \rho(\phi, \theta, \varphi) V dS. \tag{6.23}$$

A substitution of Equation (6.23) into Equation (6.22) then leads to

$$\frac{1}{V_D}\int_{\Omega} \bar{\epsilon}^f dV = \nu_f < \bar{\epsilon}^f > \tag{6.24}$$

where the angle bracket $< \cdot >$ denotes the orientation average, defined as

$$< \bar{\epsilon}^f > = \frac{\int_0^{\phi=2\pi} \int_0^{\theta=\pi} \int_0^{\varphi=2\pi} \bar{\epsilon}^f \rho(\phi,\theta,\varphi) \sin\theta d\phi d\theta d\varphi}{\int_0^{\phi=2\pi} \int_0^{\theta=\pi} \int_0^{\varphi=2\pi} \rho(\phi,\theta,\varphi) \sin\theta d\phi d\theta d\varphi}, \tag{6.25}$$

and $\bar{\epsilon}^f$ can be obtained from $\bar{\epsilon}^{f'}$ through the tensor transformation

$$\bar{\epsilon}^f_{ij} = a_{ki} a_{lj} \bar{\epsilon}^{f'}_{kl}. \tag{6.26}$$

Equation (6.21) can then be written as

$$\bar{\epsilon} = \nu_m \bar{\epsilon}^m + \nu_f < \bar{\epsilon}^f >. \tag{6.27}$$

Takao et al. [50] also conducted a similar ODF weighted integration for spheroidal inclusions in their study of the effect of fiber misorientation on the longitudinal Young's modulus.

Similarly, by taking the volume average of total stress in the composite, one obtains

$$\bar{\sigma} = \nu_m \bar{\sigma}^m + \nu_f < \bar{\sigma}^f >. \tag{6.28}$$

As a first step toward the derivation of effective stiffness, we need to evaluate the average perturbed strain $\tilde{\epsilon}$ and the average perturbed stress $\tilde{\sigma}$. By inserting Equation (6.2) as $\bar{\epsilon}^m$ and Equation (6.6) as $\bar{\epsilon}^f$ into Equation (6.27) and noticing that the volume average of the total strain $\bar{\epsilon}$ must be in balance with the externally applied strain ϵ_0, we obtain

$$\tilde{\epsilon} = -\nu_f < \epsilon^{pt} >. \tag{6.29}$$

Similarly, substitution of Equation (6.3) as $\bar{\epsilon}^m$ and the last term of Equation (6.7) as $\bar{\epsilon}^f$ into Equation (6.27) yields

$$\tilde{\sigma} = -\nu_f < \sigma^{pt} - \sigma^* > \tag{6.30}$$

where $\bar{\epsilon} = \epsilon_0 = C_m^{-1}\sigma_0$ were used.

Since the effective stiffness C of the composite relates the average stress and average strain of the composite through

$$\bar{\sigma} = C\epsilon_0, \tag{6.31}$$

we need to calculate the average stress of the composite. Substitution of Equation (6.4) as $\bar{\sigma}^m$ and Equation (6.8) as $\bar{\sigma}^f$ into Equation (6.28), and together with Equation (6.30), yields

$$\bar{\sigma} = C_m(\epsilon_0 - \nu_f < \epsilon^* >) \tag{6.32}$$

where $\sigma_0 = C_m\epsilon_0$ was used.

As shown in Equation (6.32), it is necessary to evaluate $< \epsilon^* >$ in terms of ϵ_0 in order to evaluate the effective stiffness C. To accomplish this, the equivalence principle of Equations $(6.6)'$-$(6.9)'$ in the local coordinate system is used. Solving for $\epsilon^{*'}$ from Equation $(6.9)'$, together with Equations (6.10) and (6.11), one obtains

$$\epsilon^{*'} = -C_m^{-1}(C_f - C_m)T'(\epsilon_0' + \tilde{\epsilon}'). \tag{6.33}$$

The orientation average $< \epsilon^* >$ can be evaluated according to the definition of Equation (6.25). In Equation (6.33), $\epsilon^{*'}$ is given in terms of $(\epsilon_0' + \tilde{\epsilon}')$, which in turn are related to $(\epsilon_0 + \tilde{\epsilon})$ through the usual tensor transformation. Following this process, one arrives at

$$< \epsilon^* >= -C_m^{-1}(C_f - C_m) < T > (\epsilon_0 + \tilde{\epsilon}). \tag{6.34}$$

Now a substitution of ϵ given in Equation (6.29) into Equation (6.34) yields $< \epsilon^* >$ in terms of ϵ_0. Following similar manipulations as before and after some

rearrangements, one finds that

$$< \epsilon^* >= -\boldsymbol{C}_m^{-1}(\boldsymbol{C}_f - \boldsymbol{C}_m) < \boldsymbol{T} > [\nu_m \boldsymbol{I} + \nu_f < \boldsymbol{T} >]^{-1} \epsilon_0. \qquad (6.35)$$

Substitution of Equation (6.35) into Equation (6.32) yields the effective stiffness tensor $\boldsymbol{C}$ as

$$\boldsymbol{C} = \boldsymbol{C}_m + \nu_f(\boldsymbol{C}_f - \boldsymbol{C}_m) < \boldsymbol{T} > [\nu_m \boldsymbol{I} + \nu_f < \boldsymbol{T} >]^{-1}. \qquad (6.36)$$

The orientation average $< \boldsymbol{T} >$ in Equation (6.36) can be performed by transforming the local $\boldsymbol{T}'$ into the global $\boldsymbol{T}$ through the tensor transformation Equation (6.18) and then carrying out the ODF weighted integration as shown in Equation (6.25).

6.2 Matrix Formulation

In the above development the need arises for performing a number of operations on fourth-rank tensors; e.g., contraction, inversion, coordinate transformation and ODF-weighted integration. These operations will become much simpler to perform when a fourth order tensor is written as a 6×6 matrix by use of the contracted notation. The orientation average $< \boldsymbol{T} >$ holds the same symmetry properties as $\boldsymbol{T}'$. Hence $< \boldsymbol{T} >$ can be reduced to 6×6 matrix form using the usual contracted notation. Furthermore $< \boldsymbol{T} >$ must have the symmetry properties of effective stiffness tensor.

The matrix form corresponding to Equation (6.36) is then given by

$$\boldsymbol{c} = \boldsymbol{c}_m + \nu_f(\boldsymbol{c}_f - \boldsymbol{c}_m) < \boldsymbol{t} > [\nu_m \boldsymbol{i} + \nu_f < \boldsymbol{t} >]^{-1} \qquad (6.37)$$

where i is diagonal matrix composed of [1,1,1,1/2,1/2,1/2] and the local Wu's tensor t' in matrix form is given in [104].

The orientation average of $< t >$ can be performed as before by the following integration:

$$< t > = \frac{\int_0^{\phi=2\pi} \int_0^{\theta=\pi} \int_0^{\varphi=2\pi} t\rho(\phi,\theta,\varphi) \sin\theta d\phi d\theta d\varphi}{\int_0^{\phi=2\pi} \int_0^{\theta=\pi} \int_0^{\varphi=2\pi} \rho(\phi,\theta,\varphi) sin\theta d\phi d\theta d\varphi} \tag{6.38}$$

where t can be obtained from t' through the matrix transformation [94]

$$t = mt'm^T \tag{6.39}$$

The matrix m is given by

$$m = \begin{bmatrix} a_{11}^2 & a_{21}^2 & a_{31}^2 \\ a_{12}^2 & a_{22}^2 & a_{32}^2 \\ a_{13}^2 & a_{23}^2 & a_{33}^2 \\ a_{12}a_{13} & a_{22}a_{23} & a_{32}a_{33} \\ a_{11}a_{13} & a_{21}a_{23} & a_{31}a_{33} \\ a_{11}a_{12} & a_{21}a_{22} & a_{31}a_{32} \end{bmatrix}$$

$$\begin{bmatrix} 2a_{21}a_{31} & 2a_{11}a_{31} & 2a_{11}a_{21} \\ 2a_{22}a_{32} & 2a_{12}a_{32} & 2a_{12}a_{22} \\ 2a_{23}a_{33} & 2a_{13}a_{33} & 2a_{13}a_{23} \\ a_{22}a_{33}+a_{23}a_{32} & a_{12}a_{33}+a_{13}a_{32} & a_{13}a_{22}+a_{12}a_{23} \\ a_{21}a_{33}+a_{23}a_{31} & a_{11}a_{33}+a_{31}a_{13} & a_{13}a_{21}+a_{11}a_{23} \\ a_{31}a_{22}+a_{21}a_{32} & a_{31}a_{12}+a_{32}a_{11} & a_{11}a_{22}+a_{12}a_{21} \end{bmatrix} \tag{6.40}$$

6.3 Numerical Calculation

In the previous section, we derived a closed matrix form of effective stiffness for the model system based on the Eshelby and Mori-Tanaka's theory. When applying the present model for the prediction of the effective stiffness of Al/SiC$_p$ composites studied earlier, we need information on the particle characteristics such as shape, aspect ratio and orientation distribution. The material properties of constituent phases are also required. These variables in the commercial composites differ from the model in a number of ways. Below we consider how the model can be applied to the Al/SiC$_p$ composite system.

We will make further assumption as necessary and justification of the assumptions will be addressed based on the other related work on the present model in connection with the microstructural analysis data of the Al/SiC$_p$ composites.

Particle shape. In the model of Eshelby and Mori-Tanaka, the shape of a particle is represented by an ellipsoid. Eshelby's tensor $\boldsymbol{S}$ represents both the geometry and orientation of the particle. For isotropic matrix, $\boldsymbol{S}$ is given by the Poisson's ratio of the matrix material and by the aspect ratio or relative size of the three axes a_1, a_2 and a_3. Formula of $\boldsymbol{S}$ for various particle shapes can be found in [38]. Thus, for numerical calculation purposes, the shape of SiC particle should be approximated within the framework of ellipsoids. The micrographs in Figures 5.1-5.3 show that the SiC particles are irregularly shaped and are with corners. Clearly the local stress distribution around these irregularly shaped particles will be different from that expected around ellipsoids of similar aspect ratio. However, recent photoelastic modeling work by Withers et al. [105] has demonstrated that the stress around a cylindrical SiC$_w$ and that around ellipsoid of equivalent aspect ratio are indistin-

guishable at points more than approximately half a whisker radius away from the inclusion surface. Almost irrespective of particle shape, the local fluctuations of the stress field would be expected to fall off rapidly. Thus it does not seem unreasonable to expect the mean stresses, both within the particle and in the matrix, to be quite closely approximated by the values determined for ellipsoids of major to minor axis ratio equal to the particle aspect ratio.

Here we approximated the shape of the SiC_p with a general ellipsoid and investigated the shape effects on the different components of effective elastic constants. To begin with, we first considered particle shape of prolate spheroid ($a_1 > a_2 = a_3$) and oblate spheroid ($a_1 = a_2 > a_3$). Based on the comparison of numerical results obtained from these two shapes with the experimental data, we further considered ellipsoidal particle shapes of different aspect ratios. For a fixed orientation distribution and material properties, we tested different aspect ratios including (3,1,0.1), (3,1,0.2), $\cdots$, (3,1,0.9) and found that (3,1,0.5) fitted well with the ultrasonic test results.

Aspect ratio of the particle. In this model of the effective stiffness the particle aspect ratio has been assumed to be a constant in order to facilitate the computation. We make this assumption despite the particle shape nonuniformity as shown in Figures 5.4-5.6 and Table 5.2. Takao and Taya [51] have recently studied the effect of the nonuniformity of fiber aspect ratio and found that the use of the mean value of aspect ratio for the prediction of the stiffness can be justified provided the range of the fiber aspect ratio is not too great. The aspect ratio distribution of the present Al/SiC_p system does not cover a wide range, so that the use of the mean aspect ratio can be justified.

Based on the microstructural analysis we used particle aspect ratio of α=3 ($=a_1/a_2$) and α=1/3 ($=a_3/a_1$) for prolate spheroid and oblate spheroid, respectively. For ellipsoidal particle shape we employed (a_1, a_2, a_3)=(3,1,0.5)

Orientation distribution. The stiffness of short fiber MMCs is known to be strongly dependent on the fiber orientation. The proportion of fibers at each angle is specified by the ODF $\rho(\phi, \theta, \varphi)$. By averaging the tensor $\boldsymbol{T}$ of differently oriented particles using ODF, the effective $< \boldsymbol{T} >$ is obtained.

If the particle is composed of prolate spheroids, only two angles (ϕ, θ) are enough to describe the orientation status. Based on the fabrication process of the Al/SiC$_p$ composites, and the experimental orientation distribution as shown in Figures 5.7-5.9, we assumed that the major axis x_1' of the particle was lying in the extrusion plane (i.e., $\theta = \pi/2$). By taking $\varphi = \pi/2$, we can then let the x_2' axis lie in the the x_1-x_2 plane since a_2=a_3. Furthermore the distribution of the orientation angle ϕ, the angle between the local x_1' axis and the global x_1 axis, was assumed to be random (i.e., $\rho(\phi)$=constant). This type of orientation was considered by Tandon and Weng [53]. Since the matrix expression of effective stiffness derived in the previous section and Tandon and Weng's explicit expression for calculating composites engineering constants are based on the same principle, one should expect the same numerical results. For oblate spheroids we again let $\theta = \pi/2$ and let x_1' and x_2' lie on the x_1-x_2 plane by taking $\varphi = \pi/2$. This will readily make the orientation angle ϕ random on the x_1-x_2 plane because a_1 is equal to a_2. Consequently we do not have to take the orientation average. Both types of orientation distribution function above will result in the transversely isotropic composites with isotropic properties in x_1-x_2 plane.

For ellipsoidal particle, we need three angles (θ, ϕ, φ) to describe the orientation

status. We again let the x_1' axis lie in the x_1-x_2 plane (i.e., $\theta = \pi/2$). We then need to specify the orientation distribution for the angle ϕ and φ. The angle ϕ, as before, measures the orientation angle of the longest axis x_1' from the global $x_1$axis, while the angle φ measures the rotation of x_2'-x_3' plane from the global x_3 axis and will provide an axisymmetric type distribution function. The orientation distribution for ϕ is again chosen as random. When the orientation distribution of the angle φ is known, the distribution function can be reconstructed using the concept of orientation tensor by Advani and Trucker [106]. It was found that a great number of higher order terms are required to reconstruct a relatively simple experimental ODF with accuracy. Therefore the evaluation of ODF-weighted integral in the orientation average becomes very time consuming, although not impossible. For simplicity, we decided to use random distribution for the angle φ. For the above choice of ODF, $\rho(\phi, \varphi)$ becomes constant and the overall elastic properties of the composite will be transversely isotropic.

Properties of constituent materials. The composite model is composed of two different material systems, Al matrix and SiC_p fibers, with their properties assumed to be isotropic. However, there also exists intermetallic compounds and porosity in the Al/SiC_p composites. As discussed earlier, the properties of these materials are quite different from those of Al alloy or SiC. Intermetallics were found to be present in the Al matrix region of both unreinforced samples and SiC_p reinforced samples. Thus the Al matrix in these samples can be regarded as an effective medium. Furthermore the ultrasonic results show that the properties of all the unreinforced samples are weakly orthotropic with stiffness anisotropy of no more than 3%. In general for matrices of anisotropic stiffnesses, Eshelby's method becomes nonanalytic.

Provided the matrix is transversely isotropic, the modified Eshelby's method can still be used. The errors in neglecting the effect of texture for a transversely isotropic matrix have been considered and for aluminum these effects were found to be small [105].

Porosity are also present in the 30% SiC_p samples in each series of Al/SiC_p samples. Since the volume fraction of porosity is considerably small compared to the SiC_p content, porosity was just neglected.

Based on the above observations, it does not seem unreasonable to assume isotropic elastic constants for the Al matrix of these samples. We further assumed the properties of the Al matrices in unreinforced samples in each alloy series to be the same as the properties of the Al matrices in the reinforced samples in each series of composites.

For 2124-T4-Al, C_{11}=113.5 GPa and C_{44}=27.3 GPa were used. For 7091-T6-Al, C_{11}=112.8 GPa and C_{44}=26.8 GPa were used. These values were taken from the mean of ultrasonically measured data for the SiC-free samples of 2124 and 7091 alloys.

The SiC particulates used are α-SiC. Elastic constants of SiC are rare except for Young's modulus. Schreiber and Soga [107] measured complete isotropic properties of Polycrystalline α-SiC using ultrasonic technique. For α-SiC, we used C_{11} =491.5 GPa and C_{44} =196 GPa taken from [107].

The nominal volume fraction of SiC_p was used in the calculation.

6.4 Comparison with Experimental Results

To assess the effects of particle shape on the calculated elastic constants, elastic constants of the 30% SiC_p/2124 Al composite were computed assuming the particles are: (1) prolate spheroids with an aspect ratio of α=3, (2) oblate spheroids with an aspect ratio of α=1/3, and (3) ellipsoids with (a_1, a_2, a_3)=(3,1,0.5).

The calculated results, as compared to the experimental values, are given in table 6.1. As mentioned earlier, it is first noticed that the prolate spheroidal case above gave exactly the same results when compared with Tandon and Weng's results [53]. The prolate spheroid gave generally good agreement except for the components C'_{12}, E_{11} and ν_{21}. Oblate spheroids improved the agreement of the above three components but considerably degrades the agreement of the other components such as C'_{33}, , C'_{44}, E_{33} and ν_{13}. The ellipsoidal shape with (a_1, a_2, a_3)=(3,1,0.5) seemed to provide the best overall agreement of all the elastic constants. There are, of course, an infinite number of possible combinations for the particle shape, aspect ratio, and orientation. The combinations used in the modeling are consistent with the microstructural data of the composites.

Because the ellipsoidal model seemed to provide the best agreement with the measured results, elastic constants calculations for the other SiC_p percentages in the 2124 Al series and for the other two alloy systems were made using the ellipsoid model. Figures 6.2-6.8 show comparisons of the theoretical predictions and experimental data for the 7091 Al/SiC_p system.

All the predicted elastic constants are compared with experimental results in Figures 6.2-6.8. The overall agreements between the model predictions and the ultrasonic experiments are within 7% for the three different concentrations of 7091

Table 6.1: Effects of particle shape on the elastic constants of 30% SiC_p/2124 Al composite (unit=GPa except ν_{ij})

	Prolate spheroid ($\alpha = 3$)	Oblate spheroid ($\alpha = 1/3$)	Ellipsoid $(a_1, a_2, a_3) = (3, 1, 0.5)$	Experimental data
C_{11}	166.6	171.5	171.0	169.4
C_{22}	166.6	171.5	171.0	166.6
C_{33}	155.4	150.3	155.7	156.0
C_{12}	72.0	70.6	72.6	68.6
C_{13}	70.4	70.3	70.3	68.7
C_{23}	70.4	70.3	70.3	69.7
C_{44}	43.2	40.9	43.4	45.1
C_{55}	43.2	40.9	43.4	45.6
C_{66}	47.3	50.5	49.2	49.1
E_{11}	122.7	128.4	127.3	128.6
E_{22}	122.7	128.4	127.3	125.2
E_{33}	113.8	109.5	115.1	115.5
ν_{12}	0.298	0.272	0.293	0.280
ν_{13}	0.318	0.341	0.319	0.315
ν_{23}	0.318	0.341	0.319	0.327
ν_{21}	0.298	0.272	0.293	0.271
ν_{31}	0.295	0.290	0.289	0.284
ν_{32}	0.295	0.290	0.289	0.302

Al/SiC$_p$ samples.

Some general observations are made on the 30% SiC$_p$ sample (PE-2665). The predicted diagonal stiffness components $C'_{11}(= C'_{22})$ and C'_{33} agrees well with the experimental values (Figure 6.2). The predicted shear modulus G'_{12} are also in good agreement with the experimental value, while the predicted $G'_{13}(= G'_{23})$ are about 7% lower the experimental data (Figure 6.3). The predicted off-diagonal components $C'_{13}(= C'_{23})$ agrees with the experimental values within 4%, but the predicted C'_{12} is about 7% higher than the experimental value (Figure 6.4). All predicted Young's moduli are in good agreement with the experimental values (Figure 6.5). Predicted Poisson's ratios $\nu_{13}(= \nu_{23})$ and $\nu_{31}(= \nu_{32})$ agrees well with the experimental data, while $\nu_{12}(= \nu_{21})$ are about 6% higher than the experimental values. Similar observations can be also made on the 10% and 20% SiC$_p$ samples.

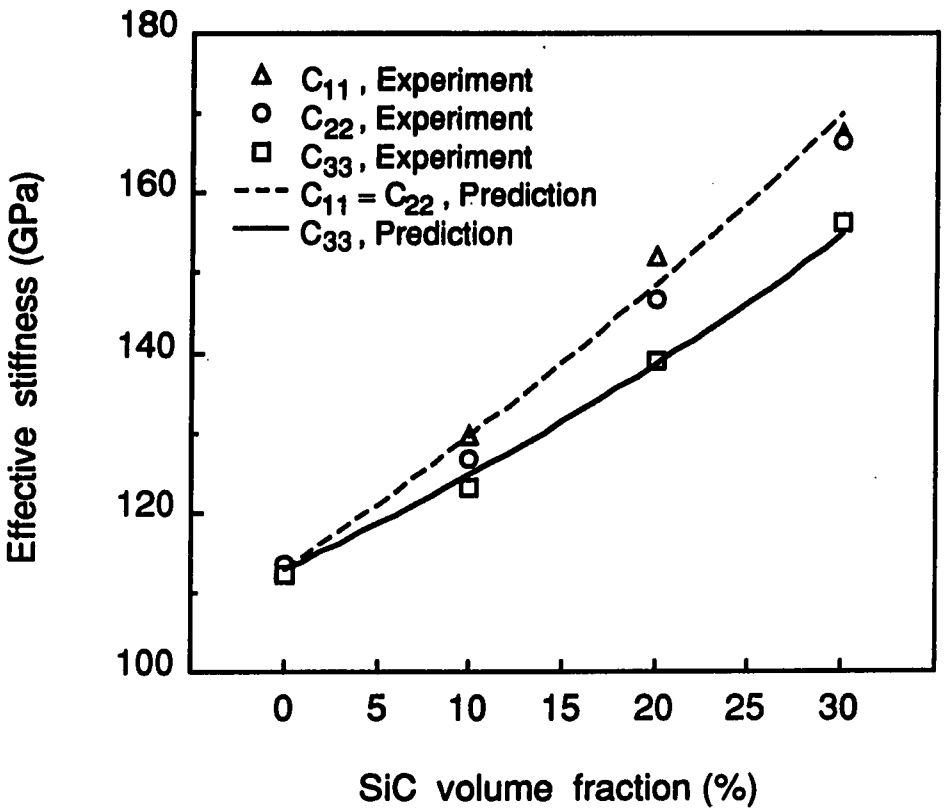

Figure 6.2: Comparison of predicted stiffnesses C_{11}, C_{22} and C_{33} with experimental results (7091 Al/SiC$_p$)

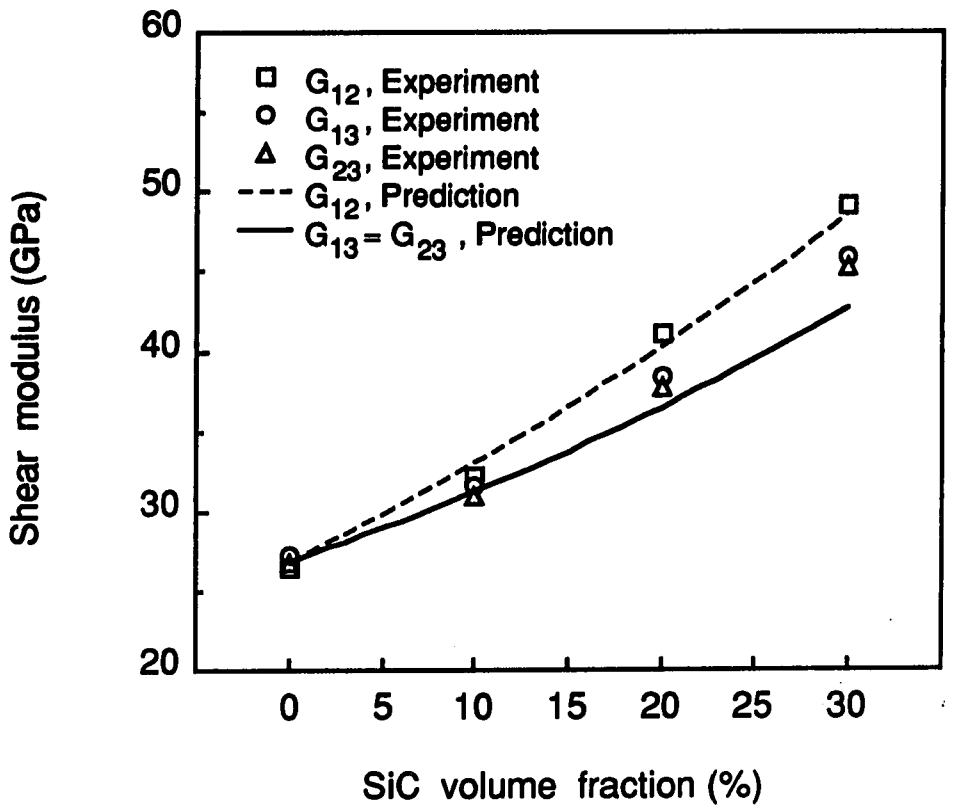

Figure 6.3: Comparison of predicted shear moduli G_{12} $(= C_{66}), G_{13}$ $(= C_{55})$ and G_{23} $(= C_{44})$ with experimental results (7091 Al/SiC$_p$)

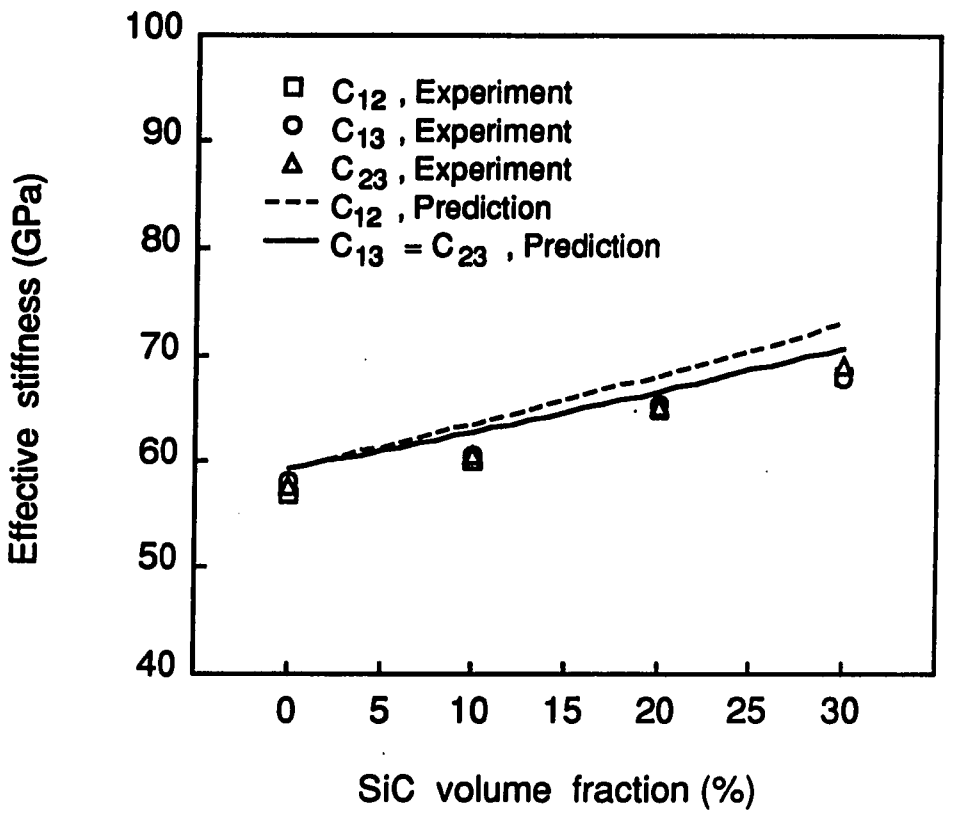

Figure 6.4: Comparison of predicted stiffnesses C_{12}, C_{13} and C_{23} with experimental results (7091 Al/SiC$_p$)

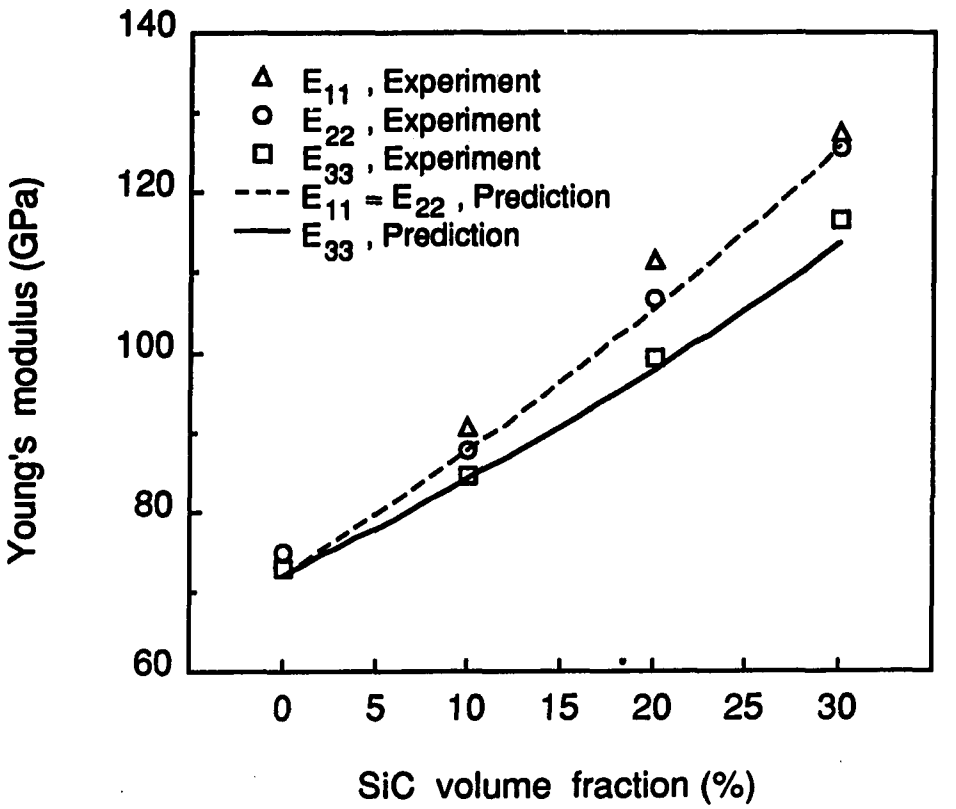

Figure 6.5: Comparison of predicted Young's moduli with experimental results (7091 Al/SiC$_p$)

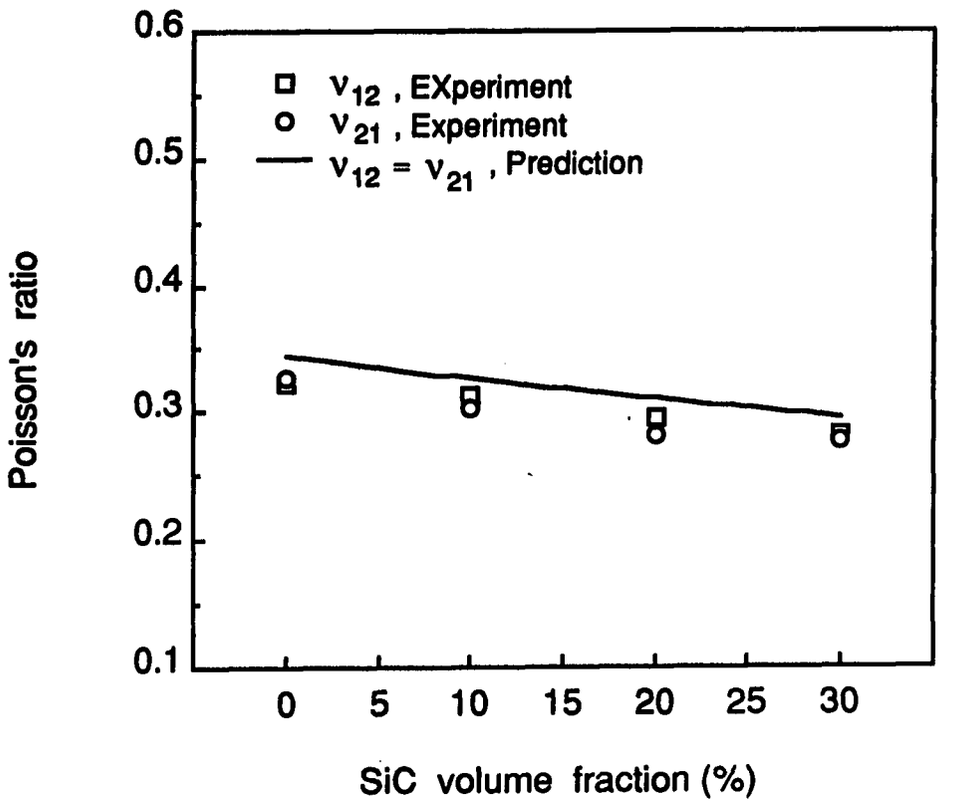

Figure 6.6: Comparison of predicted Poisson's ratios ν_{12} and ν_{21} with experimental results (7091 Al/SiC$_p$)

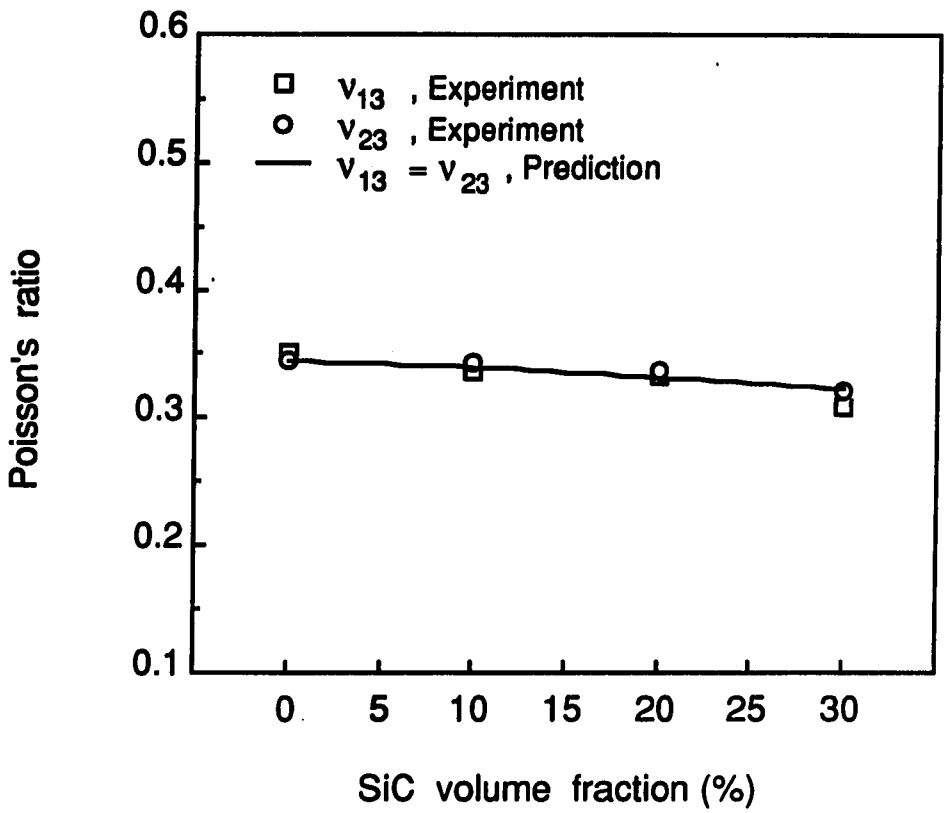

Figure 6.7: Comparison of predicted Poisson's ratios ν_{13} and ν_{23} with experimental results (7091 Al/SiC$_p$)

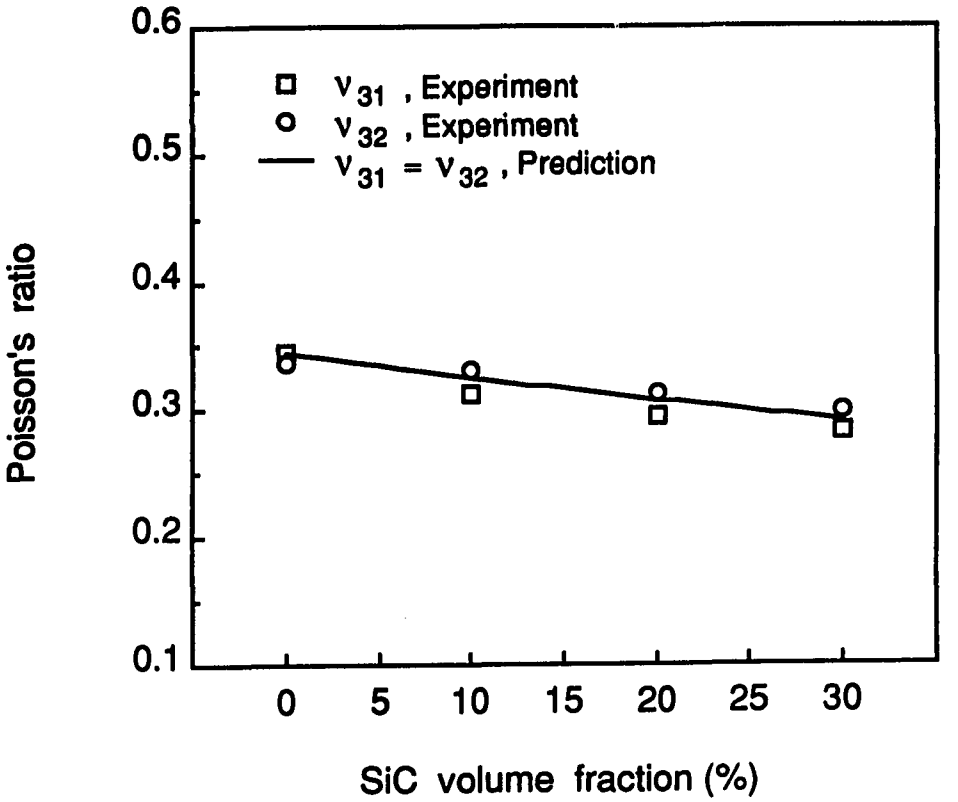

Figure 6.8: Comparison of predicted Poisson's ratios ν_{31} and ν_{32} with experimental results (7091 Al/SiC$_p$)

7. CONCLUSION

Ultrasonic velocity measurements using normal and oblique incidence in the immersion mode have determined the complete set of orthotropic elastic constants of extruded Al/SiC_p metal matrix composites.

All the reinforced samples in the 2124, 6061 and 7091 alloy systems exhibited orthotropic behavior. The maximum anisotropy occurred between the extrusion direction and out-of-plane direction for stiffness components C_{ii}, i=1,2,3 and deduced Young's moduli. However, the in-plane stiffness components, C_{11} and C_{22}, and the in-plane Young's moduli, E_{11} and E_{22}, showed only a few percent differences. Consequently the in-plane shear modulus G_{12} was highest and G_{13} and G_{23} were almost the same.

The ultrasonic measurement results agreed qualitatively with the microstructural examinations using SEM and image analysis. The observed anisotropy in the elastic constants were consistent with the preferred orientation distribution of SiC_p. The overall elastic stiffness was significantly affected by the internal defects such as intermetallic compounds and porosity.

The matrix formulation for effective stiffness calculation of two-phase composite model is of practical importance. In this approach, one does not have to explicitly calculate the eigenstrain, the perturbed strain, or the elastic strain energy. Since

the model is based on the Mori-Tanaka's theory and Eshelby's equivalent inclusion principle, it is valid for finite concentrations of ellipsoidal fibers with arbitrary orientation.

Modeling was done using the particle characteristics consistent with the microstructure analysis. A random orientation in the extrusion plane was used and transversely isotropic properties were predicted. Among different particle shapes tested, ellipsoidal model showed the best agreement with the experimental results. All predicted elastic constants agreed reasonably with the experimental results.

The agreement of in-plane Young's moduli between the ultrasonic test and the mechanical tensile test was found to be within a few percent. The agreement between the elastic constants determined by ultrasonic technique and those values predicted by the theoretical model and measured by mechanical testing indicates that the ultrasonic velocity measurement is a valid method for determining the elastic constants of short fiber reinforced metal matrix composites.

PART II. CHARACTERIZATION OF DEFECTS

1. INTRODUCTION

Voids (or porosity) are one of the most common flaws encountered during the fabrication of fiber reinforced polymer composites. Voids arise from improper curing, moisture in the prepreg and other reasons. The void content and distribution depends on the fiber volume fraction and distribution, resin properties, and processing conditions such as pressure, temperature and time. Voids caused by trapped air in the lay-up process or volatile gas released during the curing cycle tend to occur at the interface between the unidirectional laminae and they are usually elongated into ellipsoidal cavities along the adjacent fiber directions [63]. On the other hand, voids in woven laminates tend to be more spherical. Experimental studies [65,68] show that the presence of voids in a composite material may significantly reduce some of its matrix dominated mechanical properties, and may lead to greater susceptibility to moisture diffusion. Quantitative nondestructive evaluation methods for the detection and characterization of voids and void content are therefore highly desirable.

Ultrasonics has been extensively used in research and in practical NDE applications for its capability to detect distributed defects in a composite such as voids. Since voids are strong scatterers for elastic waves, the presence of matrix voids in composite laminates has noticeable effects on ultrasonic attenuation [69]. The correlation between attenuation and void contents in carbon fiber reinforced composites

are well known: greater void content causes increased attenuation and the increase is greater at higher frequencies. By manufacturing standards with known void contents, the void content of a particular system of composite can be quantitatively evaluated. Recently, measurement procedures were developed to obtain the ultrasonic attenuation as a function of frequency using broadband pulses, and correlation between attenuation slope, or $d\alpha/df$, and the volume fraction of void has been established [72]. Little emphasis, however, has been given to the corresponding dispersion, which is a necessary consequence of the attenuation.

When elastic wave propagates through a porous composite, the ultrasonic velocities generally depend on the void characteristics and fiber volume fraction as well as on the frequency. Considering the presence of voids in the matrix, increasing the void content decreases the longitudinal and shear velocities. This is due to a decrease of the elastic stiffness of the composite with an increasing void content. In addition, the presence of fiber reinforcement makes velocity decrease more rapidly with increasing void content than in the fiber-free case. Martin [77] showed that for a carbon fiber reinforced plastics (CFRP) laminate with 60% fiber content, 5% voids decreases the longitudinal wave velocity by 19% from its void-free value. The Martin study, however, assumed low frequencies, or equivalently, small fiber diameter; so that the dispersion effects were ignored. If the wavelength is of the same order of magnitude as a characteristic dimension of voids, one would expect a larger frequency range over which the medium should show velocity dispersion. Dispersion effects are evidenced by frequency dependent ultrasonic wave speeds. A pulse, being a superposition of many frequencies, will change its shape as it propagates through the dispersive medium.

In fiber reinforced composites, a common concern with using velocity as a NDE tool has been its dependence on other material properties such as variations of fiber volume fraction. The ultrasonic velocity of the composite depends on the elastic stiffness of the fiber and the matrix in the wave propagation direction. Thus, increasing the fiber contents increases the longitudinal and transverse wave velocities. This can be attributed to the fact that the stiffness of the fibers is greater than that of the matrix, so that an increase in fiber content results in larger stiffnesses of the composite and hence larger velocities. However, for a longitudinal wave propagating normal to the fibers in a carbon (or graphite) composite where the elastic constants of the anisotropic fiber is closer in value to the modulus of the matrix, the dependence of velocity on fiber volume fraction is very small [77]. Since the longitudinal velocity in CFRP propagating normal to fiber length is almost independent of the volume fraction of carbon fiber, the ultrasonic velocity can be used as a potential NDE tool for estimating the void content of CFRP.

In this thesis, a three-phase composite model containing matrix, unidirectional fiber and ellipsoidal voids was considered first to study the void characteristics and fiber properties on the ultrasonic velocity. Special emphasis was given to the anisotropic fiber properties and void shape. Effect of void content on the velocity change was similar to the Martin's study [77]. Furthermore, void shape was found to have significant effect on the rate of velocity decrease. Efforts were then made to develop a measurement technique to obtain phase velocity as a function of frequency using broadband ultrasonic pulses. In the through transmission and water immersion testing mode, phase velocity was then derived from the Fourier phase spectrum analysis through fast Fourier transform (FFT) and deconvolution principles. This technique has been

applied for obtaining the phase velocity and the dispersion of ultrasonic pulses in carbon (graphite) reinforced epoxy and polyimide samples containing different level of porosity. Composites studied included Carbon/Epoxy and Carbon/Polyimide and both woven laminates and laminates fabricated from unidirectional prepreg tapes. Void contents in the samples were determined by a destructive method, i.e., acid digestion. Correlation was sought between ultrasonic phase velocity and void content.

Finally, the applicability of Kramers-Kronig (K-K) relations was tested. The K-K relation provides a relationship between frequency dependent ultrasonic attenuation and dispersion. The validity of this relationship rests only on the linear and causal properties of the system and does not depend on details of the specific mechanism responsible for the attenuation and dispersion. When experimental results of both attenuation and velocity are available, their mutual compatibility can be checked. The relation in its local form [89], was found to hold in composites with porosity.

2. EFFECT OF VOID AND FIBER ON VELOCITY

The effect of void characteristics and fiber properties on ultrasonic wave propagation in unidirectional fiber reinforced composites are investigated in this chapter. For simplicity calculations are made in the static limit.

The model system is a three-phase composite containing matrix, fiber and void phases. For our purposes, the matrix is assumed to be isotropic, while fibers can be anisotropic. Voids are assumed to be present only in the matrix and they are all of the same shape within the framework of ellipsoid. The circular fibers are infinitely long and they are unidirectionally reinforced with random array. There is no single theory that can predict the overall elastic constants of the general multi-phase composites containing fiber anisotropy. Since the voids are present only in the matrix, the matrix and voids can be regarded as an effective homogeneous medium. The elastic constants of this medium can be computed from the matrix form of the stiffness expression given in Equation (6.37). Hashin's composite cylinders assemblage (CCA) model [108] gives closed-form results for the effective elastic constants of fiber composites with isotropic phases and transversely isotropic phases. The CCA model can be adapted to determine the overall properties of three-phase composites if the matrix and voids are replaced by the effective medium.

We investigate the dependence of the longitudinal velocity propagating normal

to the fiber length upon the void and fiber contents. The effect of fiber properties and void shape are also sought. Calculated results of the ultrasonic velocities versus fiber and void content are presented for representative composite systems.

2.1 Effective Stiffness of a Solid Containing Voids

To obtain the effective stiffness of isotropic matrix containing ellipsoidal voids, we use the matrix form of stiffness equation derived in Equation (6.37). Referring to Figure 6.1, the longest axis of each void x_1' is assumed to be parallel to the global x_1 axis (i.e., ϕ=0), and all voids are assumed to lie on the x_1-x_2 plane by setting $\theta = \pi/2$. Furthermore, the rotation angle φ of x_2' and x_3' with respect to the x_1' is assumed to have random orientation distribution. The orienatation distribution is then given by $\rho(\varphi) = \rho_0$ =constant. This type of orientation will result in a transversely isotropic properties. From Equation (6.1), the direction cosine between the ith primed and jth unprimed coordinates will be given by

$$\boldsymbol{a} = \begin{bmatrix} 1 & 0 & 0 \\ 0 & \sin\varphi & \cos\varphi \\ 0 & -\cos\varphi & \sin\varphi \end{bmatrix} \tag{2.1}$$

Then the orientation average of $< \boldsymbol{t} >$ can be performed by

$$< \boldsymbol{t} > = \frac{1}{2\pi} \int_0^{\varphi=2\pi} \boldsymbol{m}\boldsymbol{t}'\boldsymbol{m}^T d\varphi \tag{2.2}$$

where $\boldsymbol{m}$ is given by Equation (6.40). By use of Equation (2.2) together with the vanishing elastic stiffnesses for void, we can compute the effective stiffness for trans-

versely isotropic properties of a solid containing voids,

$$\boldsymbol{C} = \boldsymbol{C}_m - \nu_v \boldsymbol{C}_m < \boldsymbol{t} > [\nu_m \boldsymbol{i} + \nu_v < \boldsymbol{t} >]^{-1} \tag{2.3}$$

where ν_v is the void volume fraction.

The five engineering constants are then given by [39]

$$E_{A1} = C_{11} - \frac{2C_{12}^2}{C_{22} + C_{23}} \tag{2.4}$$

$$\nu_{A1} = \frac{C_{12}}{C_{22} + C_{23}} \tag{2.5}$$

$$k_1 = \frac{1}{2}(C_{22} + C_{23}) \tag{2.6}$$

$$G_{A1} = C_{66} \tag{2.7}$$

$$G_{T1} = \frac{1}{2}(C_{22} - C_{23}) \tag{2.8}$$

where E_{A1} is the uniaxial modulus, $\nu_{A1} = -\epsilon_{22}/\epsilon_{11}$, k_1 is the plane strain bulk modulus, G_{A1} and G_{T1} are shear moduli equivalent to G_{12} and G_{23}, respectively.

2.2 Effective Properties for Anisotropic Phases

The corresponding five engineering constants for transversely isotropic fiber are denoted by $E_{A2}, \nu_{A2}, k_2, G_{A2}$, and G_{T2}. Then the five engineering constants of a composite containing transversely isotropic matrix and transversely isotropic fibers can be obtained from the CCA model [108].

We then obtain the five effective stiffness from the five independent engineering constants. For our purpose we only need the transverse stiffness C_{22} $(= C_{33})$ given by

$$C_{22} = k^* + G^*_{T(+)} \tag{2.9}$$

where

$$k^* = \frac{k_1(k_2 + G_{T1})\nu_m + k_2(k_1 + G_{T1})v_2}{(k_2 + G_{T1})\nu_m + (k_1 + G_{T1})\nu_f} \tag{2.10}$$

and

$$G^*_{T(+)} = G_{T1}\left[1 + \frac{(1+\beta_1)\nu_f}{\rho - \nu_f(1 + \frac{3\beta_1^2\nu_m^2}{\alpha\nu_f^3+1})}\right] \tag{2.11}$$

$$\alpha = \frac{\beta_1 - \gamma\beta_2}{1 + \gamma\beta_2}, \qquad \rho = \frac{\gamma + \beta_1}{\gamma - 1} \tag{2.12}$$

$$\beta_1 = \frac{k_1}{k_1 + 2G_{T1}}, \qquad \beta_2 = \frac{k_2}{k_2 + 2G_{T2}} \tag{2.13}$$

and

$$\gamma = \frac{G_{T2}}{G_{T1}} \tag{2.14}$$

where k^* is the plane strain bulk modulus and $G^*_{T(+)}$ is the upperbound of G_T for $G_{T2} > G_{T1}$ and $k_2 > k_1$.

The longitudinal wave velocity propagating in the direction perpendicular to fiber direction is then given by

$$V_L = \sqrt{C_{22}/\rho} \tag{2.15}$$

where the composite density ρ is given by the rule of mixture as

$$\rho = \nu_f\rho_f + \nu_m\rho_m. \tag{2.16}$$

We assumed the fiber to be a circular cylinder ($a_1 \to \infty, a_2 = a_3$) and the void to be ellipsoid ($a_1 > a_2 > a_3$). The Eshelby tensor for these shapes can be found in [38].

Table 2.1: Properties of composite constituents [77]

Constituents	Elastic Constants (GPa) C_{11}	C_{12}	C_{22}	C_{23}	C_{55}	Density g/cm^3
Fiberglass composite						
Fiberglass fibers	97.6	27.5	97.6	27.5	35.1	2.48
Epoxy resin	5.5	3.0	5.5	3.0	1.3	1.21
Carbon fiber composite						
Carbon fibers	274	6	16	5.4	1.56	1.69
Epoxy resin	10.7	5.4	10.7	5.4	2.6	1.27

Typical composites containing both isotropic and anisotropic fibers are considered. For the isotropic case, we consider a composite consisting of fiberglass fiber reinforced in an epoxy resin matrix. The values used in the calculations are listed in Table 2.1. For the anisotropic case, the composite consisted of carbon fiber reinforced in an epoxy resin matrix. The constituent properties used in the calculation are also listed in Table 2.1.

2.3 Results and Discussion

Effect of void content on velocity. Figures 2.1 and 2.2 show the longitudinal velocity changes from the void free values for several typical fiber contents of fiberglass fiber and carbon fiber, respectively. Ellipsoidal voids with $(a_1, a_2, a_3) = (3, 1, 0.2)$ were used. The void contents are typical of those that occur in practice in fabricating composites. The velocity change in resin matrix is also given as a function of void content.

Regardless of the fiber type used, we see that increasing void content decreases

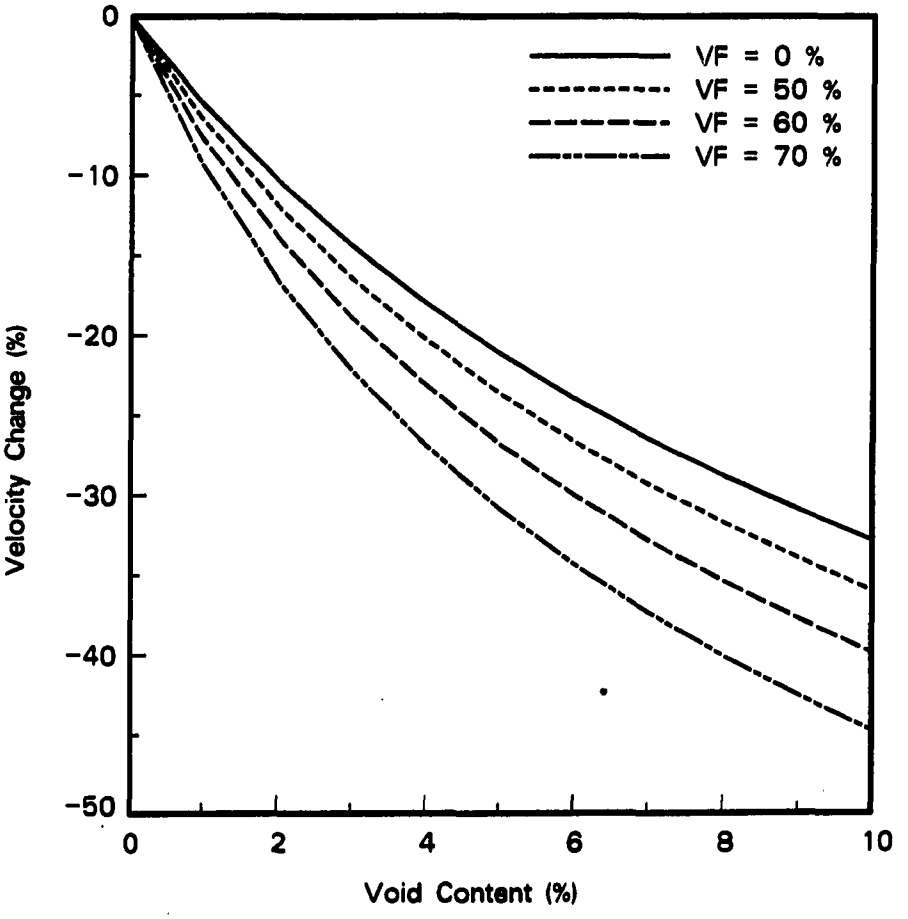

Figure 2.1: Effect of void content on ultrasonic velocity (fiberglass fiber composite)

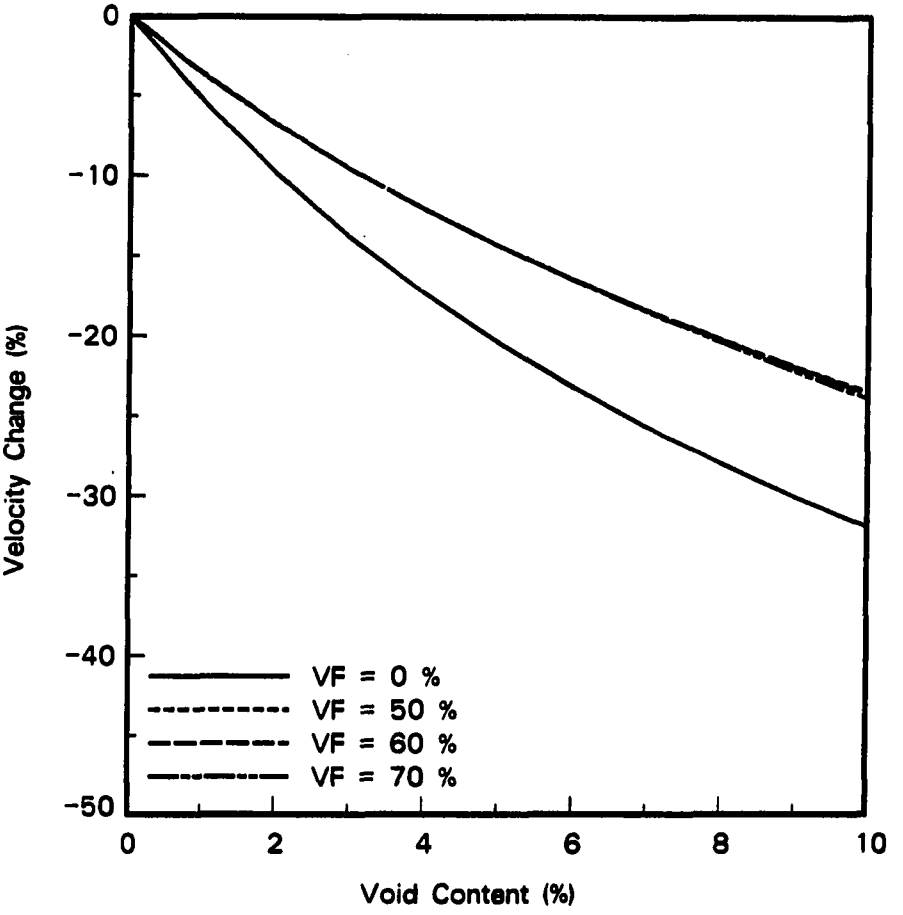

Figure 2.2: Effect of void content on ultrasonic velocity (carbon fiber composite)

the ultrasonic velocities. This is to be expected since the values of the composite elastic stiffness decreases with increasing void content. The same is true for the unreinforced epoxy matrix containing voids.

For the case of isotropic fiberglass fiber composite, the presence of fiber reinforcement causes the ultrasonic velocities to decrease more rapidly with increasing void content than for the case of no fibers. It is noticed that this behavior becomes more pronounced for higher fiber contents. For the case of transversely isotropic carbon fiber composites, however, the velocity of unreinforced resin matrix decreases more rapidly with void content than the reinforced composites. When we used the spherical void, the velocity of reinforced composites decreases slightly more rapidly than the unreinforced resin matrix. Thus,the rate of velocity decrease for composites containing voids seems to depend on the void shape too. We also notice that the carbon fiber contents have no effect on the velocity change in carbon fiber composites compared to the fiberglass fiber composites.

Effect of fiber contents on velocity. Figures 2.3 and 2.4 show the ultrasonic longitudinal velocities as a function of fiberglass fiber and carbon fiber contents, respectively for several void contents. Ellipsoidal voids with $(a_1, a_2, a_3) = (3, 1, 0.2)$ were used. Figure 2.3 shows that increasing the fiberglass fiber content increases the ultrasonic longitudinal velocities. The reason for this is that the fiber elastic constants are larger than those of the matrix (Table 2.1) so that increasing the fiber content results in larger values of composite elastic stiffness that enter into the velocity expression. This behavior is more pronounced for higher fiber contents. For carbon fiber composites (Figure 2.4), the lonitudinal velocity does not depend much on the fiber contents. The carbon fiber anisotropy causes pronounced differences in

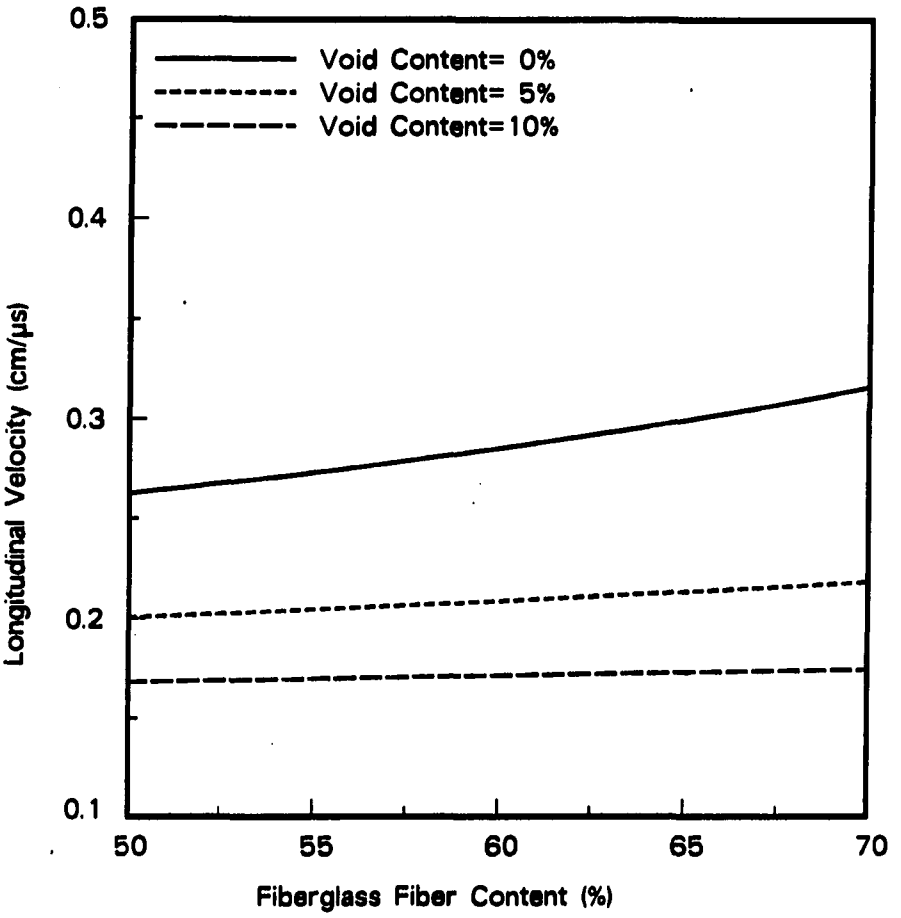

Figure 2.3: Effect of fiber content on ultrasonic velocity (fiberglass fiber composite)

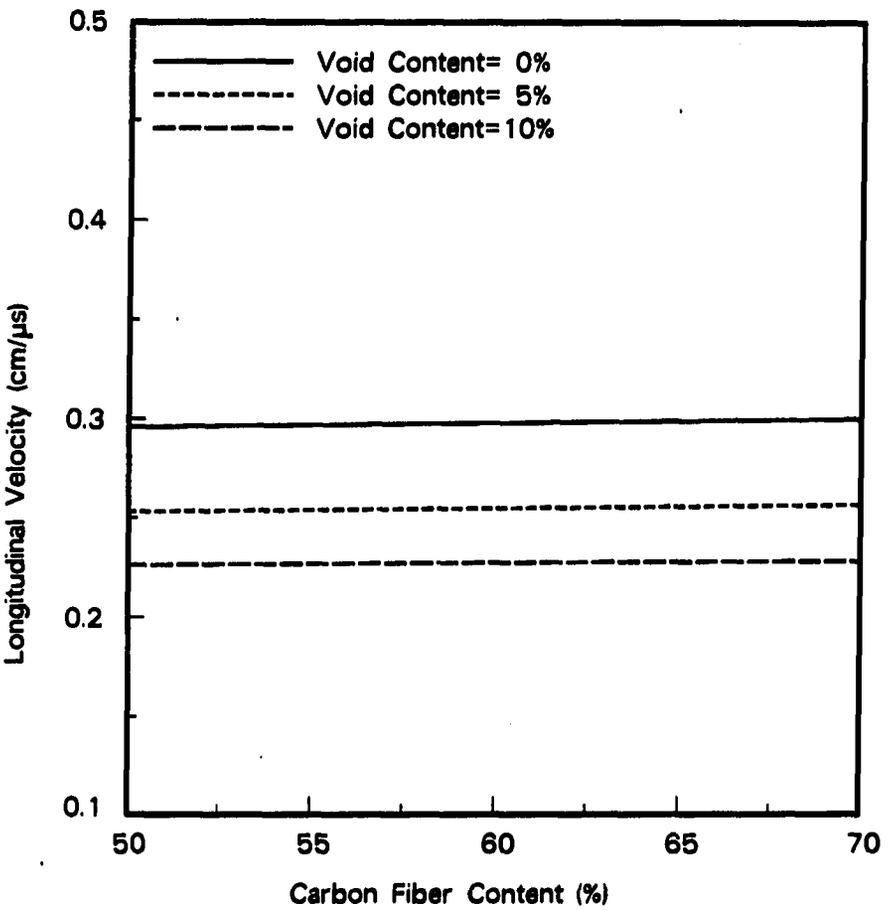

Figure 2.4: Effect of fiber content on ultrasonic velocity (carbon fiber composite)

the relative behavior of the velocities as a function of fiber content. These observations can be explained by considering the elastic constants of constituent phases. For the longitudinal velocity in the direction normal to the fiber direction, the dominant elastic constant is C'_{22} for both fiber and matrix. For the fiberglass composite, the value of C'_{22} (fiber) is approximately 18 times that of C'_{11} (matrix). This accounts for the significant influence of fiberglass fiber content on the longitudinal velocity. In the carbon fiber composites, C'_{22} (fiber) is close in value to C'_{11} (matrix) so that the effect of carbon fiber content on the transverse longitudinal velocity is very small.

Effect of void shape on velocity. Figures 2.5 and 2.6 show the longitudinal velocity change of composites for different void shapes. The fiber volume fraction of 60% was used for both fiber types. Among the various void shapes used, the ellipsoidal shape of $(a_1, a_2, a_3) = (3, 1, 0.2)$ shows the largest decrease in velocity change. As the void shape changes from sphere to thin, ribbon-like ellipsoid, velocity decreases more rapidly. The decrease rate is in general more significant in fiberglass composites. The effect of void shape can be explained by considering the surface area of voids having the same volume. The geometry of void affect the aspect ratio. Specifically a thin, flat, ribbon-shaped void has a larger perimeter than a round spherical void with an equivalent volume. Spherical voids have the minimum surface area-to-volume ratio; hence any change in cross sectional geometry will increase the aspect ratio of the void.

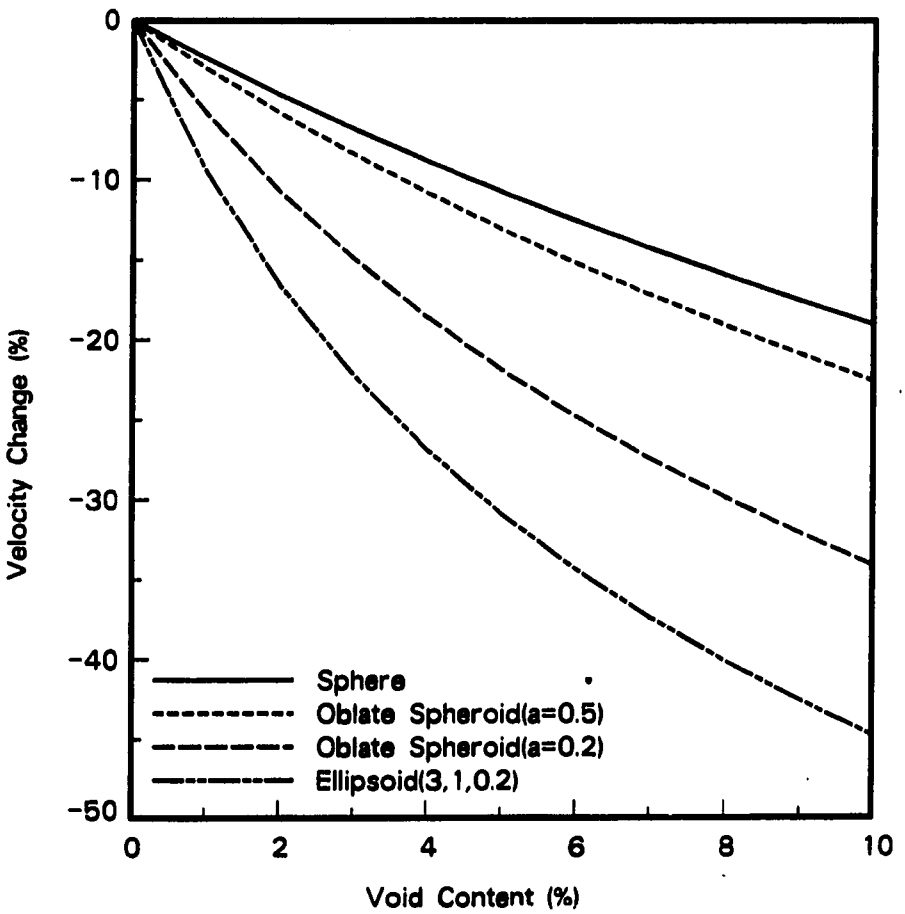

Figure 2.5: Effect of void shape on ultrasonic velocity (fiberglass fiber composite)

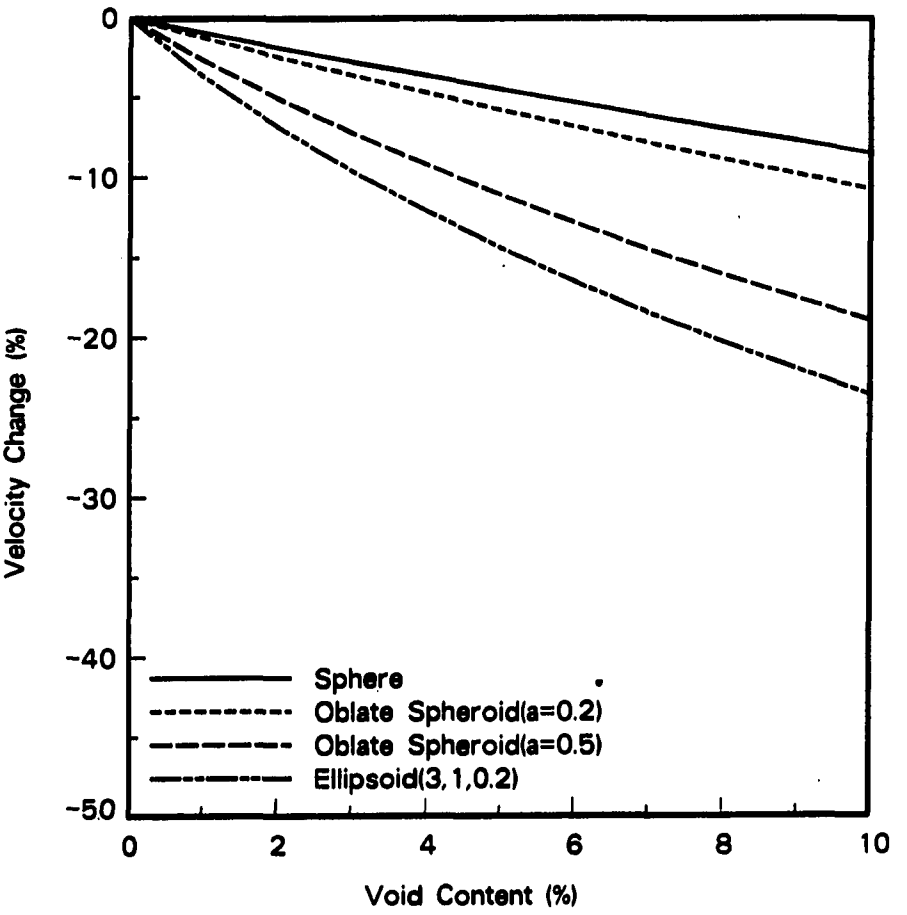

Figure 2.6: Effect of void shape on ultrasonic velocity (carbon fiber composite)

3. ULTRASONIC DISPERSION AND ATTENUATION

When an ultrasonic pulse, being a superposition of many different frequencies, propagates a real elastic solid, signal distortion is observed after a certain distance. This distortion can be attributed either to attenuation (different signal amplitude reduction with propagation distance) or dispersion (pulse expansion or contraction due to different frequency components travelling with different velocities). Attenuation is the loss of the energy associated with the decrease in the stress wave amplitude due to scattering and absorption, and is generally frequency dependent. Dispersion is characterized by the frequency dependent phase velocity of plane harmonic waves. Attenuation in the fiber reinforced epoxy composites is relatively high due to scattering by fibers and viscoelastic absorption in the epoxy matrix. Experimental works [109,110] show that attenuation is frequency dependent and increases with frequency for fiber reinforced composites. The dispersion characteristics in these materials is attributed to the viscoelastic nature of the material as well as its structural geometry. However, experimental work [109] shows that the dispersion of epoxy matrix was relatively small for all wave modes. It has also been observed that when the elastic waves propagate in a direction normal to the fibers, there are no dispersive effects as long as the wavelength is much larger than the fiber diameter [111]. More recently, Kim and Park [110] have shown that the phase velocity of longitudinal waves in

carbon/epoxy composites is independent of frequency in the long wavelength limit.

For the analysis of the fiber reinforced composites containing voids, we assume that the solids comprise a linear system, and they are capable of supporting one dimensional plane waves (i.e., the concept of an effective homogeneous medium holds) along its thickness direction. Such system admits plane wave solution of the form $exp\ i[\omega t - k(\omega)x]$, where $k(\omega)$ being the wave number of the averaged field and ω being circular frequency of the incident wave. As long as the total energy is conserved regardless of mechanisms responsible for attenuation and dispersion, we can define a complex wave number $k(\omega)$ and real circular frequency ω, where real part of $k(\omega)$ is a dispersion part of the wave number related to the frequency dependent phase velocity, $v(\omega)$, while the imaginary part of $k(\omega)$ is attenuative part related to the frequency dependent attenuation of the wave, $\alpha(\omega)$. These relations can be written as

$$k(\omega) = k_r(\omega) + i\ k_i(\omega) \tag{3.1}$$

$$= \omega/v(\omega) + i\ \alpha(\omega) \tag{3.2}$$

3.1 Calculation of Phase Velocity and Attenuation

Consider a composite plate of thickness h immersed in an elastic fluid (water). In a through transmission, water immersion testing mode, the phase velocity and attenuation in the plate thickness direction can be obtained by specifying the wave form in the propagation path without and with sample. Figure 3.1 shows that the measurement configuration using a substitution method in the through transmission, immersion testing mode. A broadband longitudinal pulse is normally incident on the plate. This results in an infinite series of reflected and transmitted pulses.

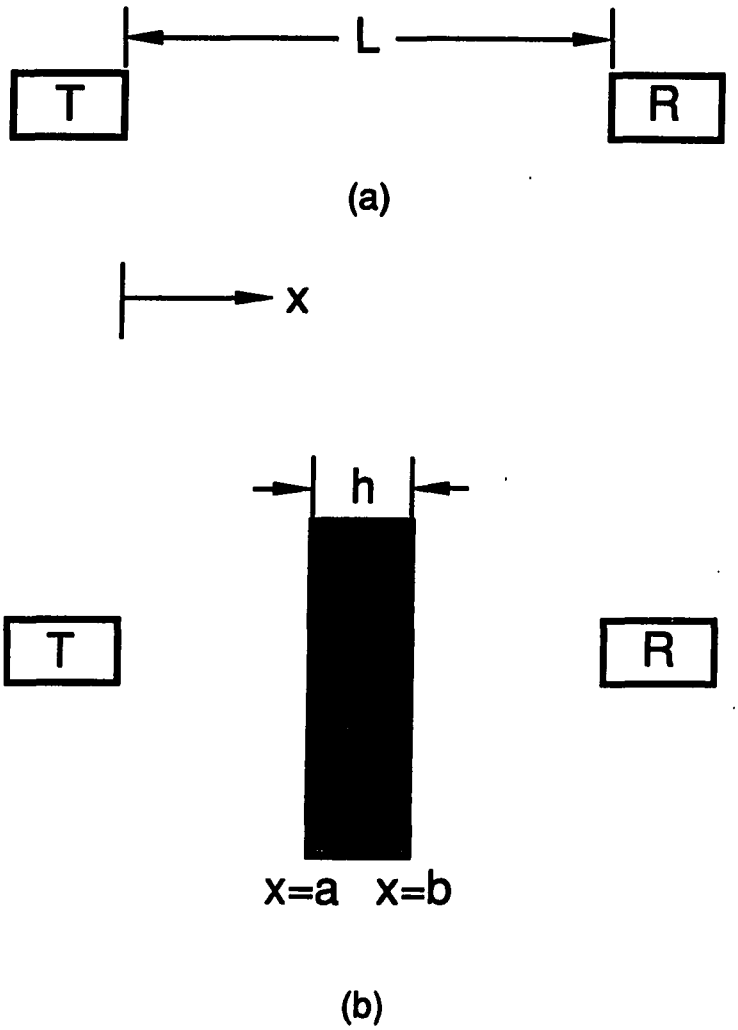

Figure 3.1: Measurement configuration for substitution method; (a) For reference waveform (b) For sample waveform

Let the displacement in the incident field be given by

$$u^{inc} = f_0(\omega t - k_0 x) \tag{3.3}$$

where $f_0(s) = 0$ for $s < 0$ and k_0 is the wave number of a monochromatic harmonic wave.

We consider a relatively thick specimen such that the reflected and transmitted pulses of the sample can be clearly separated from each other in the time domain. For our purpose, the first transmitted field is only considered. The displacement field for this pulse can be written as

$$u_4 = T_{12}T_{21}f_0(s - s_4); \quad s_4 = h(k - k_0). \tag{3.4}$$

Here $s = \omega t - k_0 x, h = b - a$ is the plate thickness, R_{ij} is the reflection coefficient in medium i from medium j, T_{ij} is the transmission coefficient for a wave incident in medium i and transmitted into medium j, k is the wave number of the plate. R_{ij} and T_{ij} are given by

$$R_{12} = \frac{\rho_0 v_0 - \rho v}{\rho_0 v_0 + \rho v} = -R_{21} \tag{3.5}$$

$$T_{12} = \frac{2\rho_0 v_0}{\rho_0 v_0 + \rho v} = 2 - T_{21} \tag{3.6}$$

where ρ_0 and ρ are, respectively, the density of water and the plate material.

The Fourier transform of a function $f(t)$ is defined as

$$F^*(\omega) = \frac{1}{\sqrt{2\pi}} \int_{-\infty}^{\infty} f(t)e^{-i\omega t}dt, \quad -\infty < \omega < \infty \tag{3.7}$$

with the associated inverse transform given by

$$f(t) = \frac{1}{\sqrt{2\pi}} \int_{-\infty}^{\infty} F^*(\omega)e^{i\omega t}d\omega. \tag{3.8}$$

Now consider the transmitted field for a thick specimen. Two measurement are made. In the first, the wave travels only through water. Let the receiving transducer be located at $x = l > b$. Then

$$u^{inc}(l,t) \equiv (t) = f_o(\omega t - k_o l). \tag{3.9}$$

The specimen is now inserted in the wavepath and the signal due to Ray 4 alone is recorded. Thus,

$$u_4(l,t) \equiv g(t) = T_{12}T_{21}f_o(\omega t - k_o l + k_o h - kh). \tag{3.10}$$

Let $F^*(\omega), G^*(\omega)$ and $F_o^*(\omega)$ be the Fourier transforms of $f(t), g(t)$ and $f_o(t)$, respectively. Then, an application of the shifting theorem for Fourier transforms yields

$$F^*(\omega) = e^{-ik_o l}F_o^*(\omega), \tag{3.11}$$

$$G^*(\omega) = e^{-i(k_o l - k_o h + kh)}F_o^*(\omega) \tag{3.12}$$

and

$$\frac{G^*(\omega)}{F^*(\omega)} = T_{12}T_{21}e^{-i(k_o h + kh)}. \tag{3.13}$$

If we set

$$\frac{G^*(\omega)}{F^*(\omega)T_{12}T_{21}} = Me^{i\phi}, \tag{3.14}$$

then use of (3.2) for $k(\omega)$ and $k_o(\omega)$ yields

$$v(\omega) = [\frac{1}{v_o} - \frac{\phi(f)}{2\pi fh}]^{-1}, \tag{3.15}$$

$$\alpha(\omega) = \frac{\ln M}{h}. \tag{3.16}$$

It is assumed that water behaves in a perfectly elastic manner, i.e., the wave number k_o is real and $v_o = \omega/k_o$.

4. EXPERIMENTAL PROCEDURE

4.1 Experimental Setup

Two nearly identical broadband transducers were set up in an immersion tank to face each other and separated by a distance of typically $15cm$. The transducers used are 0.5 inch and 0.25 inch diameter unfocused probes with nominal frequency of 2.25 and 5 MHz. To get the broadband pulse, one transducer was excited by a spike voltage pulse produced by a Panametrics model 5052PR pulser/receiver and the receiving transducer was aligned with the transmitting transducer to obtain maximum gain. The specimen was then placed between the two transducers and adjusted perpendicularly to one of the transducer faces.

The signal from the receiving transducer was acquired by digital sampling in a LeCroy 9400 digital oscilloscope, averaged over one hundred times to increase S/N ratio, and transferred to file storage in a Textronix 4052 computer, where further processing is performed.

A typical window of 512 data points with 8 bit vertical resolution is constructed containing a pulse and this represents the time data to be Fourier transformed. The data are usually sampled at a rate of about 9.76 ns per point. The fourier transform gives 257 frequency data points with 0.2 MHz frequency interval for both amplitude and phase, ranging between zero and Nyquist frequency, 51.2 MHz.

4.2 Implementation

Correction of spurious 2π errors. The frequency domain spectra are calculated using FFT algorithm provided by the system software for both the signal transmitted through water alone as a reference and the signal transmitted with the sample inserted in the path of the beam. Rectangular window was often used to obtain the first arrival sample signal only. As shown in Equation (3.15), the phase velocity is obtained by calculating the phase difference ϕ between the sample signal and the reference signal. This phase difference can be obtained by making use of deconvolution principle, where the frequency response of the sample alone is calculated by dividing the sample FFT data by the reference only spectrum.

The phase spectrum of a signal, $x(t)$, is calculated by the relation

$$\phi(\omega) = ATAN2(ImX(\omega), ReX(\omega)). \tag{4.1}$$

The ATAN2 function keeps the phase in the interval $(-\pi, \pi)$. Phase unwrapping routines are often used to obtain the continuous phase spectrum. The routine simply inserts a 2π radians (or 360°) correction whenever there is a jump in $\phi(\omega)$ of more than π radians (or 180°). Thus the phase uncertainty of $\pm 2\pi m$, m being integer, may arise at low frequencies because the spectral contents of the ultrasonic pulse do not extend all the way to zero frequency. Thus the continuous phase spectra may contain spurious 2π errors. This error was corrected using the nearly linear property of the phase slope of the medium with dispersion. First, using two pairs of data points, (ϕ_1, f_1) and (ϕ_2, f_2), within the usable bandwidth of the amplitude spectrum, the y-axis intercept was found and compared with $2\pi m$. If there was a -2π error in the phase, for instance; the calculated intercept will be close in value to -2π. The

correct $\phi(f)$ is then obtained by adding 2π. Figure 4.1 show phase spectrum before and after the 2π correction.

Time delay of digitizing window. The phase difference ϕ between the sample signal $g(t)$ and the reference signal $f(t)$ was found with respect to a common time window. Often it is necessary to shift the reference or sample signal by say, t_d, to fit the signal of interest into the digitizing window. The phase velocity equation is then modified to account for the time delay of the digitizing window, see below.

Sound velocity in water. The sound velocity in water was assumed as nondispersive. In practice, the velocity of sound in water is a function of temperature, and the sound velocity in water was computed using the equation given in [96].

Diffraction effects on phase velocity. In practice, the transmitting and receiving transducers are not idealized plane wave source and sensor. Diffraction effects may cause the measured value of the velocity and attenuation of the received signal to be higher than it actually is. Since the effect of diffraction on the phase shift of the acoustic signal is small, no phase correction was made.

Combining the $2\pi m$ correction, the window time delay t_d and the sound velocity in water as a function of temperature, we arrive at the following equation for the phase velocity in the sample:

$$v(f) = [\frac{1}{v_0(T)} - \frac{\phi(f)/2\pi f + t_d}{h}]^{-1} \tag{4.2}$$

The attenuation coefficient $\alpha(f)$ given by Equation (3.16) can be simultaneously obtained using the deconvolution procedure provided one compensates properly for sample signal loss due to transmission. Both the reference and sample signal can be corrected for diffraction effects. However, for composite samples with sickness much

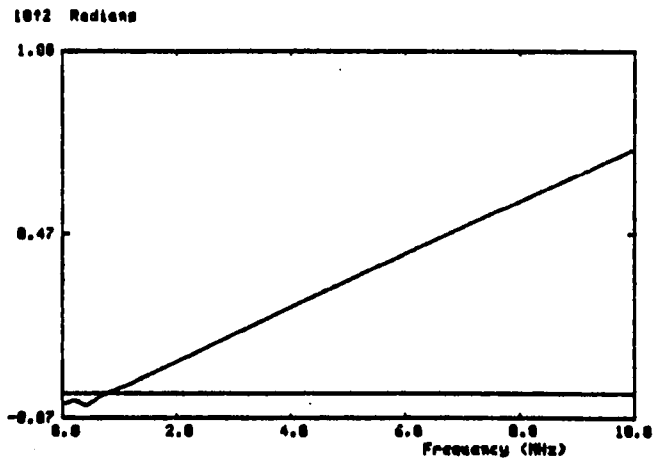

(a)

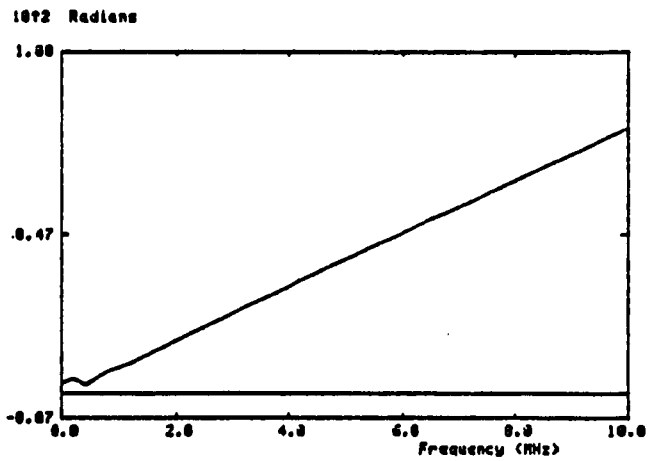

(b)

Figure 4.1: Phase spectrum (a) with -2π error (b) after 2π correction

less than the transducer separation distance, the difference between the two signals is quite small as to be cancelled out.

The above method does not work when the thickness of composite plate h is rather thin. By thin sample it is meant that a series of reflected and transmitted pulses are not clearly resolved in the time domain. It usually occurs when $h \geq 3\lambda$ where λ is the wavelength. Kinra and Dayal [87] and Pialucha et al. [88] proposed a new ultrasonic technique for measuring phase velocity and attenuation for thin samples.

4.3 Materials and Microstructures

Four groups of composite samples were used in this study. The first group (A series) consists of four coupons of 16 plies of unidirectional carbon/epoxy laminates containing a porosity content of zero to 6.5% as determined by acid digestion. The second group (B series) is quasi-isotropic $[\pm 45/0/90]_{4s}$ laminates of the same material with 0-4% void content. The third group (D series) of samples consists of four coupons of 8 ply woven carbon/epoxy laminates with coarse weave pattern and has 0-5% porosity. The typical thickness of samples in these three groups were about 0.1 inch The fourth group (6240 series) consists of 5 samples of six plies of 8-harness satin weave and covers a porosity content of 0-11%. The thickness of the samples varied from $0.2cm$ for void free coupon to about $0.24cm$ for 11% void coupon. Table 4.1 lists the sample designation in each group, their lay-up and void contents as determined by acid digestion.

In order to examine the void shape in these samples optical micrographs were taken on highest porosity samples from each group. Typical results are shown in

Table 4.1: Sample description and void content

Designation	Material	lay-up	Void content (%)
A1	carbon/epoxy	unidirectional	6.53
A2	carbon/epoxy	unidirectional	2.04
A4	carbon/epoxy	unidirectional	1.14
A5	carbon/epoxy	unidirectional	0.20
B1	carbon/epoxy	quasi-isotropic	4.05
B2	carbon/epoxy	quasi-isotropic	2.82
B4	carbon/epoxy	quasi-isotropic	1.25
B5	carbon/epoxy	quasi-isotropic	0.34
D1	carbon/epoxy	woven	5.09
D2	carbon/epoxy	woven	1.58
D3	carbon/epoxy	woven	3.41
D5	carbon/epoxy	woven	0.01
6240-4	carbon/polyimide	woven	1.20
6240-7	carbon/polyimide	woven	2.90
6240-8	carbon/polyimide	woven	5.40
6240-9	carbon/polyimide	woven	7.90
6240-13	carbon/polyimide	woven	11.20

Figures 2.2-2.5.

4.4 Results and Discussion

4.4.1 Phase velocity measurement results

Figure 4.6 shows the phase velocity of longitudinal waves propagating normal to the woven carbon/epoxy laminates (D series). To demonstrate that the measurement velocity results do not depend on the particular type of transducers used, both 5 MHz and 10 MHz transducers were used and their results are compared. As can be seen the agreement is good. The void-free sample shows no dispersion over the frequency range used. The observed nondispersion of void-free composites agree with the point-by-point toneburst measurements by Williams et al. [109].

Results in Figure 4.6 show that the velocity decreases with increasing void content. This behavior agrees qualitatively with the three-phase static composite model studied in the previous chapter.

The velocity dispersion is greater for laminates with more voids. The velocity data obtained with the phase spectral technique were compared with point-by-point toneburst measurements made at different frequencies. The agreement were very good. Experimental or theoretical data on the velocity change or dispersion of porous composite laminates are rare in the literature so that any quantitative evaluation of present results are impossible.

Measurements were also made in unidirectional and quasi-isotropic laminates, and the results were similar to that in Figure 4.6. The correlation of decreasing velocity with increasing porosity was also observed in a set of five woven carbon/polyimide laminates.

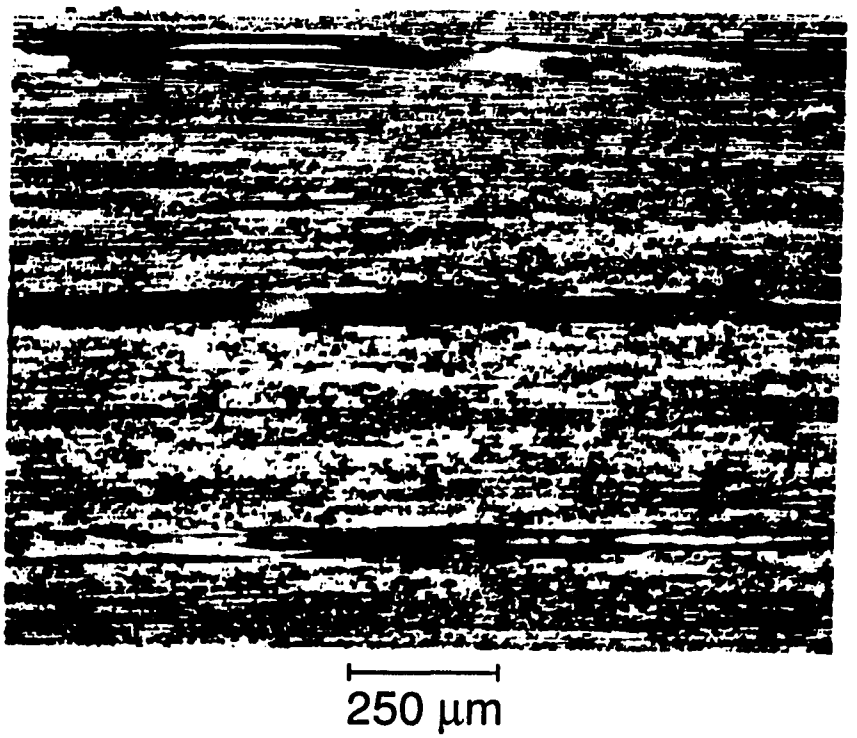

Figure 4.2: Optical micrograph of sample A1 (6.53% voids)

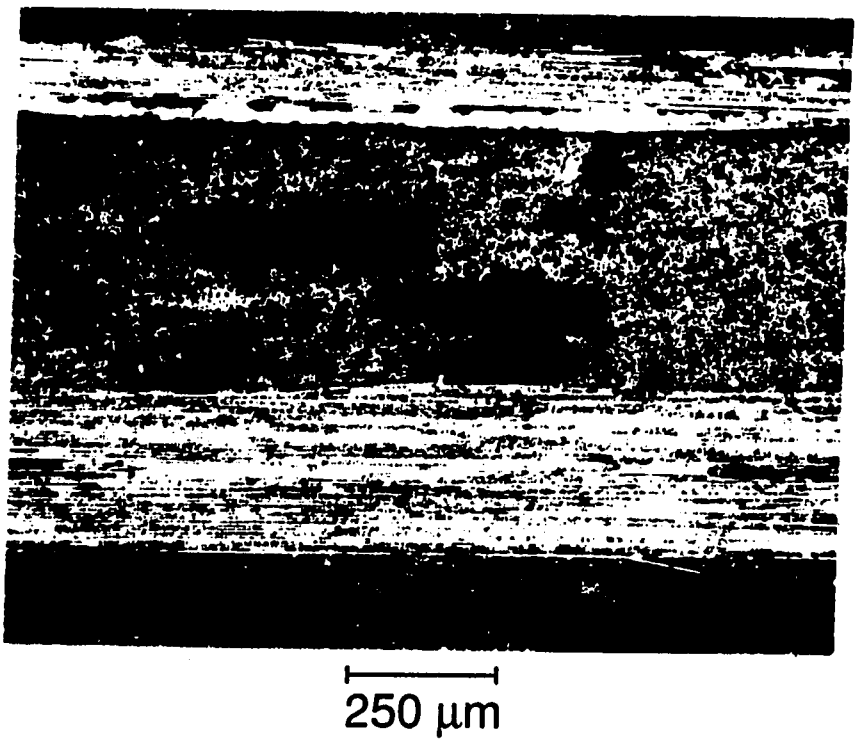

Figure 4.3: Optical micrograph of sample B1 (4.05% voids)

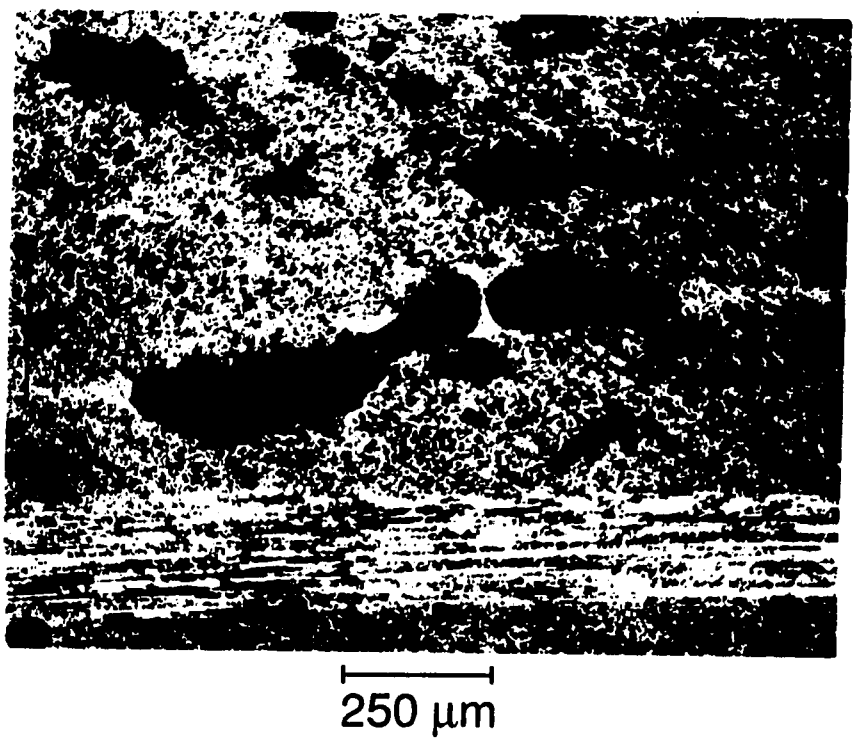

Figure 4.4: Optical micrograph of sample D1 (5.09% voids)

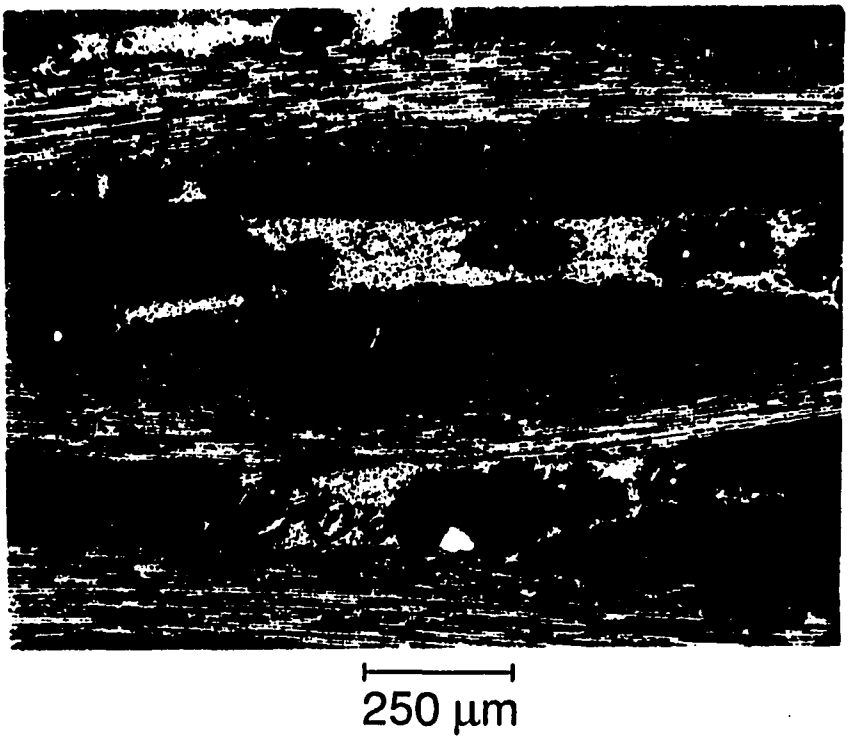

Figure 4.5: Optical micrograph of sample 6240-13 (11.2% voids)

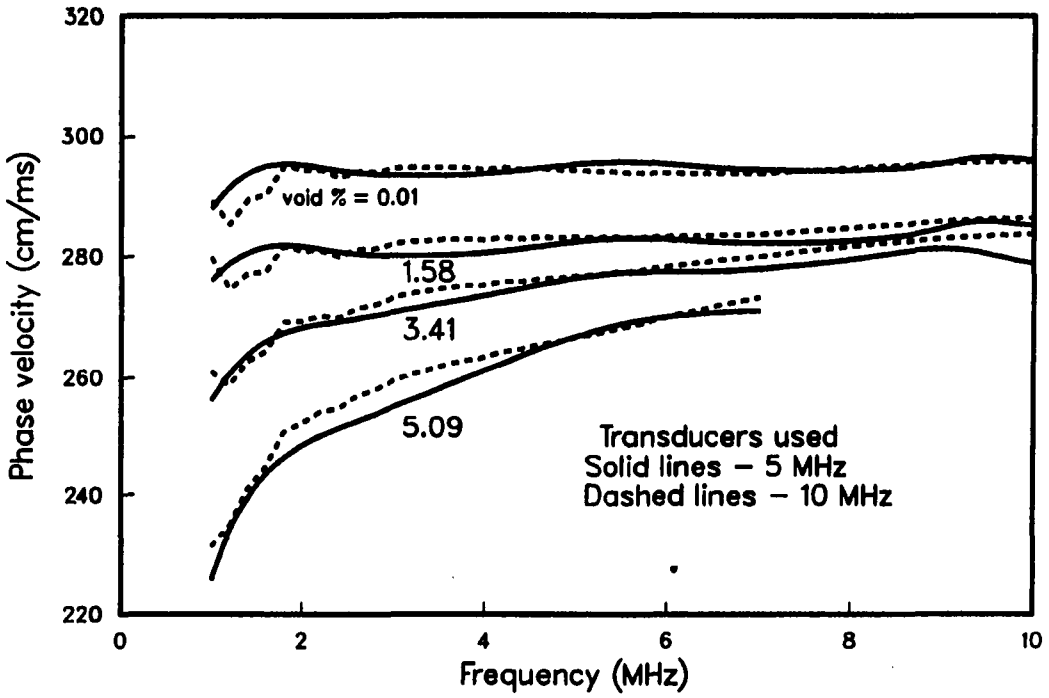

Figure 4.6: Phase velocity of longitudinal waves in woven carbon/epoxy laminates

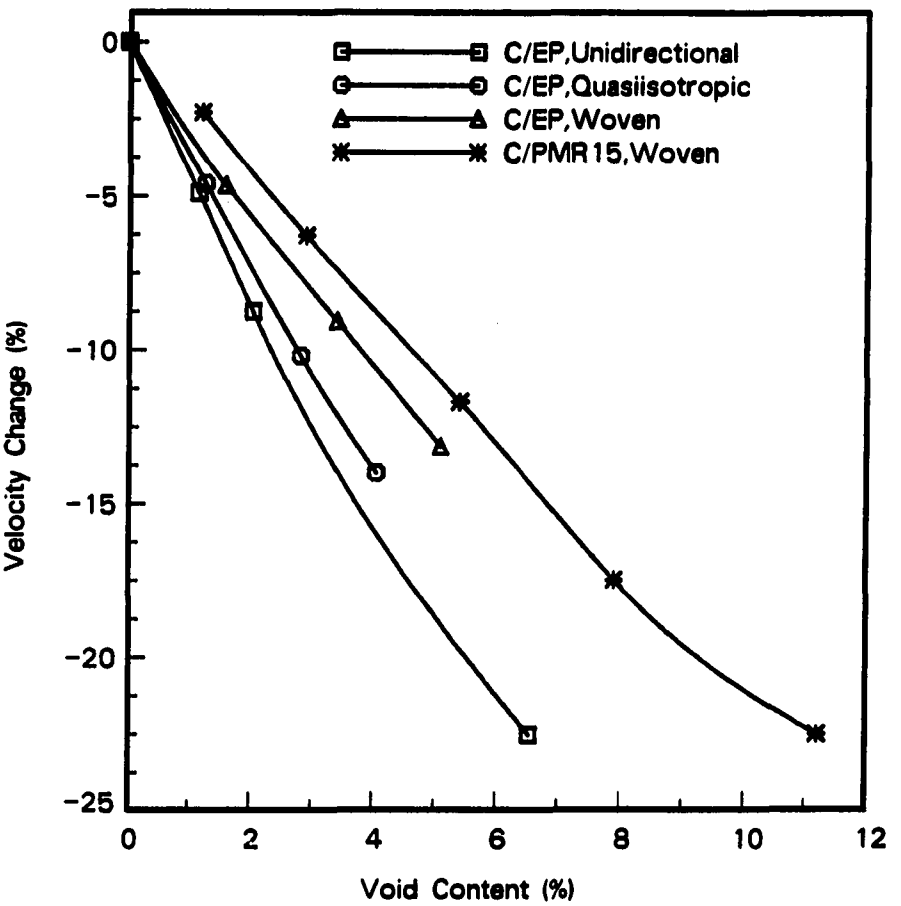

Figure 4.7: Velocity change versus void content at 2 MHz

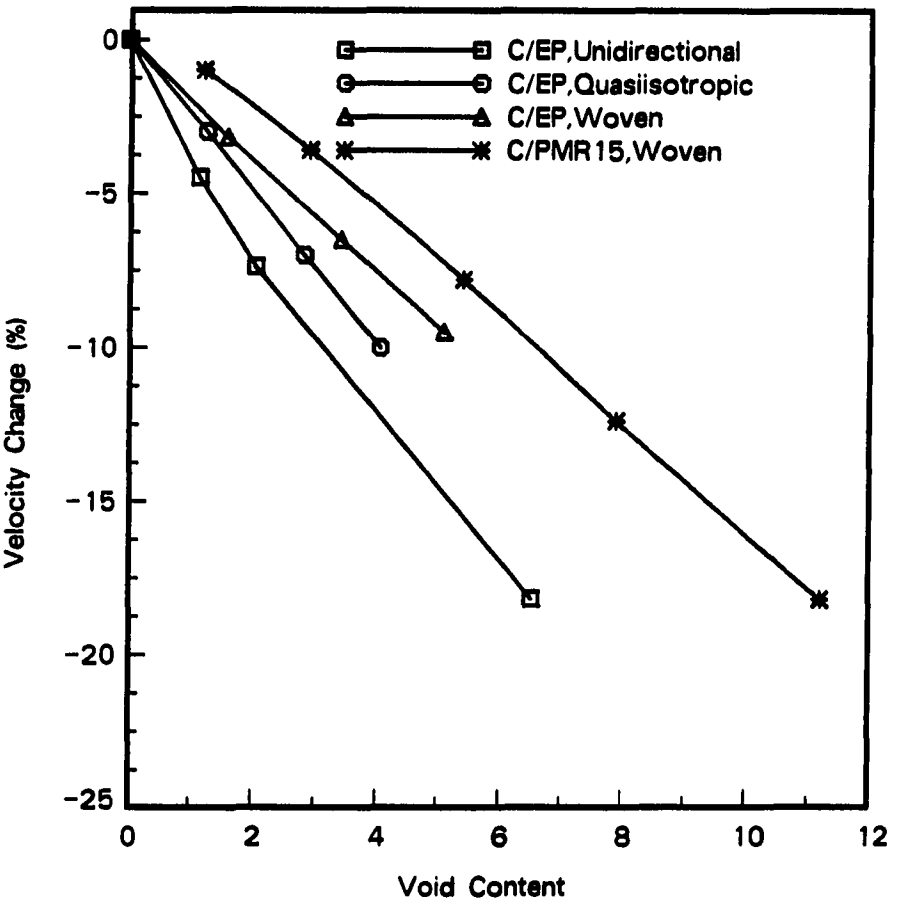

Figure 4.8: Velocity change versus void content at 5 MHz

To make a quantitative correlation between the velocity change and the void content, the fractional velocity decrease $\Delta v/v$ (expressed in percent) with respect to the velocity in a void-free sample was plotted against the void content. Figure 4.7 shows the results for four groups of composites at a frequency of 2 MHz. As a comparison, the same plot was also made at a frequency of 5 MHz, as shown in Figure 4.8. A review of the results at different frequencies revealed that at lower frequencies the velocity decrease rate is stiffer than the rate at higher frequencies. It can be expected that with increasing frequency the slope will become closer to each other because the dispersion effect is less significant at higher frequency. The order of magnitude in velocity decrease at a given frequency is the highest in the unidirectional samples and the lowest in the carbon/polyimide woven laminates. The quasi-isotropic laminates and the carbon/epoxy woven laminates are in between. The cause of this difference can be attributed to the shape of voids in these samples.

4.4.2 Microstructural Analysis

Figures 4.2-4.5 show that voids are present in the resin-rich region. The shape of voids are very much different in each series of sample. Voids in the unidirectional carbon/epoxy laminates tend to be very long, flat and elongated while the voids in quasi-isotropic laminates shows disk-like shape. On the other hand, voids in the woven carbon/polyimide are very spherical. Voids in the woven carbon/epoxy laminates are less spherical and the size has a large variation. It is clear that the lay-up has some effect on the formation of void shape. The void shape observed through microstructural analysis now explains the different velocity decrease in each group of sample at a given frequency. The woven carbon/polyimide sample containing spher-

ical voids show the smallest decrease. The unidirectional laminate containing long, flat, ribbon-shaped voids show the largest decrease. These experimental results are also in agreement with the three-phase model at static limit.

5. TEST OF THE KRAMERS-KRONIG RELATION

It is well known that ultrasonic attenuation and velocity are related by the Kramers-Kronig relation. In the general Kramers-Kronig relation the velocity change is proportional to an integration over frequency from zero to infinity of $\alpha(\omega)/\omega^2$. A simpler form of the Kramers-Kronig relation, known as the local approximation, relates the velocity change and the attenuation over a finite frequency range [89].

$$\frac{1}{v(\omega_0)} - \frac{1}{v(\omega)} = \frac{2}{\pi}\int_{\omega_0}^{\omega} \frac{\alpha(\omega')}{\omega'^2} d\omega' \tag{5.1}$$

where $v(\omega_0)$ and $v(\omega)$ are respectively the velocities at frequencies ω_0 and ω. In this work the local approximation is applied to the attenuation and velocity of composites containing porosity. Figure 5.1 shows the phase velocity in woven carbon/polyimide composites with 0-11% voids as measured by 5 MHz transducers. Also shown in Figure 5.1 are the calculated velocity using the Kramers-Kronig relation and a reference frequency ω_0 at 5 MHz. This calculation used frequency dependent attenuation data obtained previously and the comparison is normalized at $\omega_0 = 5$ MHz. These results show that the local approximation of the Kramers-Kronig relation holds in porous composites where the velocity dispersion and attenuation is quite large.

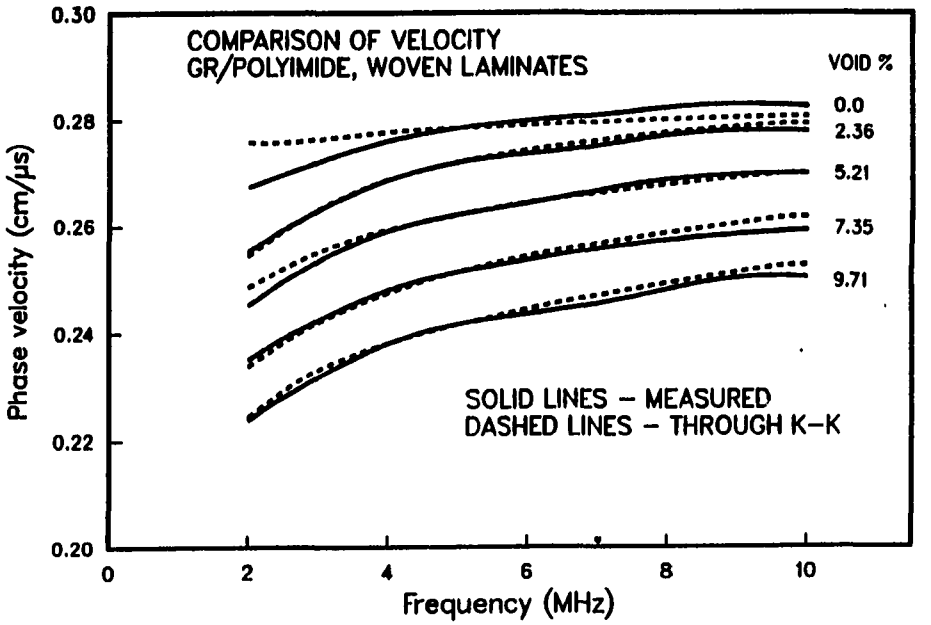

Figure 5.1: Comparison of measured velocity in carbon/polyimide composites with calculated velocity using Kramers-Kronig relation

6. CONCLUSION

A three-phase composite model containing isotropic matrix, unidirectional fibers and ellipsoidal voids was considered in the investigation of the effects of void characteristics and fiber properties on the longitudinal wave velocity propagating normal to the fiber direction. The results showed that increasing void content decreased the velocity from the void-free value. The volume fraction of isotropic fibers were found to have a significant effect on the velocity decrease of porous composites, whereas the volume fraction of transversely isotropic fibers had a negligible effect. The void shape also had a substantial effect on the rate of velocity decrease due to voids. As the void shape changes from spheres to flat ellipsoidal voids, the rate of decrease became stiffer for both types of fibers.

Phase velocity measurement technique was developed to find a correlation between the void content and phase velocity change due to voids from the void-free value. Using fast Fourier transform (FFT) and phase spectroscopy, the velocity measurement method was implemented for through-transmission, immersion testing mode. Phase velocity was measured on a series of graphite fiber reinforced epoxy and polyimide samples containing different level of void content. The measurements yielded frequency dependent velocity over the effective band of the transducers used. The void content in carbon fiber reinforced composites were found to correlate with

changes in the ultrasonic phase velocity. With increasing void content, the velocity decreased substantially. In addition, the velocity in the composites containing voids was found to be more dispersive than that in void-free composites. The velocity change was also affected by the void shape. The composite samples containing flat, ellipsoidal voids showed the steeper decrease rate compared to the composites containing spherical voids. Experimental observations on the velocity change at a given frequency agreed qualitatively with the static model behavior and the actual void shape. Finally, the relationship between the ultrasonic attenuation and the velocity change was compared to that described by the local approximation of the Kramers-Kronig relation. The local form of Kramers-Kronig relation was found to hold in porous CFRP with relatively large dispersion.

GENERAL SUMMARY

1. Ultrasonic velocity measurements using the normal and oblique incidence in the immersion mode have determined the complete orthotropic elastic stiffnesses of extruded Al/SiC_p metal matrix composites.

2. The anisotropy observed in the elastic constants measured by ultrasonics were consistent with the preferred orientation distribution of SiC_p. In addition, overall stiffnesses of Al/SiC_p were largely affected by internal defects such as voids and intermetallic compounds.

3. A 6×6 matrix form for calculating effective stiffness of two-phase composite materials was developed based on Eshelby's equivalent inclusion idea and Mori-Tanaka'a average stress concept. The elastic constants of Al/SiC_p MMCs were predicted using the particle characteristics consistent with microstructures. All predicted elastic constants agreed reasonably well with the ultrasonic measurement results.

4. A fiber reinforced composite containing voids was used in the study of the effect of void characteristics and fiber properties on the ultrasonic velocity propagating normal to the fiber length. The velocity decreases with increasing void content and it is almost independent of the volume fraction of transversely

isotropic fibers. In addition, the shape of void has a considerable effect on the rate of velocity decrease.

5. Phase velocity measurement technique was developed. Using fast Fourier transform and phase spectroscopy, the method was implemented for through transmission and immersion testing mode.

6. The void contents in CFRP were found to correlate with the ultrasonic phase velocity. With increasing void content, the velocity decreased substantially. In addition, the velocity in the composites containing voids was found to be more dispersive than that in void-free composites.

7. The relationship between ultrasonic attenuation and velocity change was tested using the local approximation of Kramers-Kronig relations. The local form of Kramers-Kronig relations was found to hold in porous CFRP with relatively large dispersion.

REFERENCES

[1] M. Taya and R. J. Arsenault, *Metal Matrix Composites*, Pergamon Press, New York (1989).

[2] C-H. Anderson and R. Warren, *Composites* **15**, 16 (1984).

[3] S. V. Nair, J. K. Tien and R. C. Bates, *International Metals Reviews* **30**, 275 (1985).

[4] W. H. Sheldon, *Materials Evaluation* **36**, 41 (1978).

[5] D. J. Hagemaier and R. H. Fassbender, *Materials Evaluation* **37**, 43 (1979).

[6] R. Prakash, *Composites* **11**, 217 (1980).

[7] I. G. Scott and C. M. Scala, *NDT International* **15**, 75 (1982).

[8] P. R. Teagle, *Composites* **14**, 115 (1983).

[9] D. J. Hagemaier and R. H. Fassbender, *Materials Evaluation* **43**, 556 (1985).

[10] W. N. Reynolds, *SAMPE Quarterly* **16**, 1 (1985).

[11] D. Proulx, C. Roy and D. G. Zimcik, *Canadian Aeronautics and Space J.* **31**, 325 (1985).

[12] Y. Bar-Cohen, *Materials Evaluation* **44**, 446 (1986).

[13] R. D. Adams and P. Cawley, *NDT International* **21**, 208 (1988).

[14] R. E. Shannon, P. K. Liaw and W. G. Clark, Jr., To appear in *Metallurgical Transactions A*.

[15] P. L. Blue, *Rev. Prog. Quant. NDE* **8B**, 1157 (1989).

[16] G. Mott and P. K. Liaw, *Metallurgical Transactions A* **19A**, 2233 (1988).

[17] W. G. Clark, Jr., and J. N. Iyer, *Materials Evaluation* **47**, 460 (1989).

[18] P. K. Liaw, R. E. Shannon, W. G. Clark, Jr. and W. C. Harrigan, In M. E. Fine Symposium, TMS-AIME, Warrendale, PA (1990). In press.

[19] L. S. Fu, *Applied Mechanics Reviews* **35**, 1047 (1982).

[20] M. C. Bhardwaj, *Advanced Materials & Processes* **136**, May (1989) p.53.

[21] A. Wolfenden, M. R. Harmouche, G. V. Blessing, Y. T. Chen, P. Terranova, V. Dayal, V. K. Kinra, J. W. Lemmens, R. R. Phillips, J. S. Smith, P. Mahmoodi and R. J. Wann, *J. Testing and Evaluation* **17**, 2 (1989).

[22] J. A. Gallego-Juarez, In *Ultrasonic Methods in Evaluation of Inhomogeneous Materials*, ed. by A. Alippi and W. G. Mayer, Kluwer Academic Pub., Hingham, MA (1987), p. 281.

[23] J. E. Zimmer, *J. Acoust. Soc. Am.* **47**, 795 (1970).

[24] H. M. Ledbetter and D. T. Read, *J. Appl. Phys.* **48**, 1874 (1977).

[25] R. D. Kriz and W. W. Stinchcomb, *Exp. Mech.* **19**, 41 (1979).

[26] G. V. Blessing and W. L. Elban, *J. Appl. Mech.* **48**, 965 (1981).

[27] W. C. Van Buskirk, S. C. Cowin and R. Carter, Jr., *J. Mater. Sci* **21**, 2759 (1986).

[28] H. M. Ledbetter and S. K. Datta, *J. Acoust. Soc. Am.* **79**, 239 (1986).

[29] M. F. Markham, *Composites* **1**, 145 (1970).

[30] G. D. Dean *ASTM STP 521* (1973), p. 326.

[31] R. E. Smith, *J. Appl. Phys.* **43**, 2555 (1972).

[32] G. D. Dean and T. Turner, *Composites* **4**, 174 (1973).

[33] J. H. Gieske and R. E. Allred, *Exp. Mech.* **14**, 158 (1974).

[34] S. I. Rokhlin and W. Wang, *J. Acoust. Soc. Am* **86**, 1876 (1989).

[35] A. Woolf, *Polymer Testing* **5**, 375 (1985).

[36] R. A. Kline, *Mater. Eval.* **46**, 986 (1987).

[37] R. C. Stiffler, Ph.D. Thesis, Virginia Polytechnic Institute and State U., Blacksburg, VA (1986).

[38] T. Mura, *Micromechanics of Defects in Solids*, Kluwer Academic Pub., Hingham, MA (1987).

[39] R. M. Christensen, *Mechanics of Composite Materials*, John Wiley & Sons, New York (1979).

[40] H. L. Cox, *Br. J. Appl. Phys.* **3**, 72 (1952).

[41] A. Kelly and N. H. MaCmillan, *Strong Solids*, Oxford U. Press, New York (1986).

[42] V. L. Nardone and K. M. Prewo, *Script Metall.* **20**, 43 (1986).

[43] M. Taya and R. J. Arsenault, *Script Metall.* **21**, 349 (1987).

[44] R. M. Jones, *Mechanics of Composite Materials*, McGraw-Hill Book Co., New York (1975).

[45] Z. Hashin and S. J. Shtrikman, *J. Mech. Phys. Solids* **10**, 335 (1962).

[46] Z. Hashin and S. J. Shtrikman, *J. Mech. Phys. Solids* **11**, 127 (1963).

[47] J. D. Eshelby, *Proc. Roy. Soc.* **A241**, 376 (1957).

[48] T. Mori and K. Tanaka, *Acta Metall.* **21**, 571 (1973).

[49] M. Taya and T. Mura, *J. Appl. Mech.* **48**, 361 (1981).

[50] Y. Takao, T. W. Chou and M. Taya, *J. Appl. Mech.* **49**, 536 (1982).

[51] Y. Takao and M. Taya, *J. Comp. Mater.* **21**, 140 (1987).

[52] G. J. Weng, *Int. J. Eng. Sci.* **22**, 845 (1984).

[53] G. P. Tandon and G. J. Weng, *Polym. Comp.* **5**, 327 (1984).

[54] G. P. Tandon and G. J. Weng, *Comp. Sci. Tech.* **27**, 111 (1986).

[55] Y. H. Zhao, G. P. Tandon and G. J. Weng, *Acta Mech.* **76**, 105 (1989).

[56] Y. H. Zaho and G. J. Weng, *J. Appl. Mech.* **57**, 158 (1990).

[57] M. Taya, *J. Comp. Mater.* **15**, 198 (1981).

[58] M. Taya and T. W. Chou, *Int. J. Solids Structures* **17**, 553 (1981).

[59] Y. Benveniste, *Mechanics of Materials* **6**, 147 (1987).

[60] Y. Benveniste, *J. Appl. Mech.* **57**, 474 (1990).

[61] A. N. Norris, *J. Appl. Mech.* **56**, 83 (1989).

[62] D. Hull, *An Introduction to Composite Materials*, Cambridge U. P., New York (1981).

[63] D. K. Hsu and K. M. Uhl, *Rev. of Prog. Quant. NDE* **6B**, 1175 (1987).

[64] D. K. Hsu, *Rev. Prog. Quant. NDE* **7B**, 1063 (1988).

[65] K. M. Uhl, B. Lucht, H. Jeong and D. K. Hsu, *Rev. Prog. Quant. NDE* **7B**, 1075 (1988).

[66] N. C. W. Judd and W. W. Wright, *SAMPE J.* **14**, 10 (1978).

[67] M. J. Yokota, *SAMPE J.* **14**, 11 (1978).

[68] B. D. Harper, G. H. Staab and R. S. Chen, *J. Comp. Mater.* **21**, 280 (1987).

[69] D. E. W. Stone and B. Clark, *Nondest. Testing* **8**, 137 (1975).

[70] B. G. Martin, *NDT International* **9**, 242 (1976).

[71] J. M. Hale and J. N. Ashton, *NDT International* **21**, 321 (1988).

[72] S. M. Nair, D. K. Hsu and J. H. Rose, *J. Nondest. Eval.* **8**, 13 (1989).

[73] Y. Bar-Cohen and R. L. Crane, *Mater. Eval.* **40**, 970 (1982).

[74] E. D. Blodgett, L. J. Thomas and J. G. Miller, *Rev. Prog. Quant. NDE* **5B**, 1267 (1986).

[75] D. E. Yuhas, C. L. Vorres and R. A. Roberts, *Rev. Prog. Quant. NDE* **5B**, 1275 (1986).

[76] J. D. Achenbach and J. Qu, *Rev. Prog. Quant. NDE* **5B**, 1179 (1986).

[77] B. G. Martin, *J. Appl. Phys.* **48**, 3368 (1977).

[78] W. N. Reynolds and S. J. Wilkinson, *Ultrasonics* **16**, 159 (1978).

[79] D. K. Hsu and H. Jeong, *Rev. Prog. Quant. NDE* **8B**, 1567 (1989).

[80] W. Sachse and Y. Pao, *J. Appl. Phys.* **49**, 4320 (1978).

[81] K. W. Winkler, *1982 Ultrasonics Symposium*, (1982) p.1054.

[82] R. A. Kline, *J. Acoust. Soc. Am.* **76**, 498 (1984).

[83] R. A. Kline and D. M. Egle, *NDT International* **18**, 341 (1986).

[84] M. S. Hughes, S. M. Handley and J. G. Miller, *1987 Ultrasonics Symposium* (1987) p.1041.

[85] D. R. Allen and W. H. B. Cooper, *NDT International* **16**, 205 (1983).

[86] D. R. Hull, H. E. Kautz and A. Vary, *Mater. Eval.* **43**, 1455 (1985).

[87] V. K. Kinra and V. Dayal, *Exp. Mech.* **28**, 288 (1988).

[88] T. Pialucha, C. C. H. Guyott and P. Cawley, *Ultrasonics* **27**, 270 (1989).

[89] M. O'Donnell, E. T. Janes and J. G. Miller, *J. Acoust. Soc. Am.* **69**, 696 (1981).

[90] J. H. Rose, D. K. Hsu and L. Adler, *J. De Physique* **C10**, 787 (1985).

[91] J. H. Rose, *Rev. Prog. Quant. NDE* **5B**, 1617 (1986).

[92] A. I. Beltzer and N. Brauner, *J. Mech. Phys. Solids* **33**, 471 (1985).

[93] A. I. Beltzer and N. Brauner, *Mechanics of Materials* **5**, 161 (1986).

[94] B. A. Auld, *Acoustic Fields and Waves in Solids*, Robert E. Krieger Pub. Co., Malabar, Florida (1990).

[95] B. Hosten and B. Castagnede, *C. R. Acad. Sci. Paris.* **t.296**, 297 (1983).

[96] W. Kroebel and K. H. Mahrt, *Acoustica* **35**, 154 (1976).

[97] R. B. Mignogna, *Rev. Prog. Quant. NDE* **9**, (1990).

[98] *ASM Handbook*, Vol. **1**, ASM International, Materials Park, OH (1987).

[99] D. L. McDanels, *Metall. Trans. A* **16A**, 1105 (1985).

[100] J. M. Papazian and P. N. Adler, *Metall. Trans. A* **21A**, 401 (1990).

[101] T. J. Warrner and W. M. Stobbs, *Acta Metall.* **37**, 2873 (1989).

[102] M. Ferrari and G. C. Johnson, *Mech. Mater.* **8**, 67 (1989).

[103] R. Hill, *J. Mech. Phys. Solids* **13**, 213 (1965).

[104] T. T. Wu, *Int. J. Solids Struct.* **2**, 1 (1966).

[105] P. J. Withers, W. M. Stobbs and O. B. Pederson, *Acta Metall.* **37**, 3061 (1989).

[106] S. G. Advani and C. L. Trucker III, *J. Rheol.* **31**, 751 (1987).

[107] E. Schreiber and N. Soga, *J. Am. Ceram. Soc.* **49**, 342 (1966).

[108] Z. Hashin, *J. Appl. Mech.* **46**, 543 (1979).

[109] J. H. Williams, Jr., H. Nayeb-Hashemi and S. S. Lee, *J. Nondest. Eval.* **1**, 137 (1980).

[110] H. C. Kim and J. M. Park, *J. Mater. Sci.* **21**, 4335 (1986).

[111] J. D. Achenbach and G. Herrmann, *AIAA J.* **6**, 1832 (1968).

ACKNOWLEDGEMENTS

I would like to express my sincere gratitude to my major professor Dr. David K. Hsu for his guidance and inspiration during the course of this work. With his great understanding and insight in various fields of NDE related problems, he guided me patiently throughout this research.

I would also like to express my appreciation to Professors Otto Buck, David K. Holger, T. J. McDaniel, and R. Bruce Thompson for offering advice and serving on my committee. The financial support from the Engineering College and the Center for NDE throughout the course of the Ph.D. program is acknowledged with gratitude. I am especially grateful to Westinghouse Electric Company for providing us with the metal matrix composite samples and for their partial financial support.

To my wife Jinok, I am specially thankful for her love and patience that helped me a lot to work hard with great enthusiasm. I am also deeply indebted to my family in Korea for their support and encouragement during my study in the United States.